



Semi-analytical Modelling of Time-variable Blazar Jet Spectra

Ana Milovanović

October 31, 2008

*Submitted in accordance with the requirements for
the degree of Doctor of Philosophy.*

The University of Leeds

School of Physics & Astronomy

The candidate confirms that the work submitted is her own and that appropriate credit
has been given where reference has been made to the work of others.

This copy has been supplied on the understanding that it is copyright material
and that no quotation from the thesis may be published without proper acknowledgement.

Acknowledgements

I am most grateful to my supervisor Dr. Joachim Rose for all his time and support (and patience), as well as for giving me the opportunity to pursue my interest in theoretical aspects of blazar astrophysics.

I am indebted to Prof. Martin Pohl and Dr. Phill Skelton their invaluable input and discussions and to Prof. Markus Böttcher for taking time to answer my question-laden emails. Many thanks to Dr. Alex Wagner, Dr. Jim Hinton, Dr. Michael Daniel, Dr. Julian Pittard, and Dr. Jamie Holder for fruitful discussions. Thanks are also in order to the rest of the Astrophysics Group at the University of Leeds for their friendship and support, especially to Dr. Stella Bradbury¹ and Dr. Alex Syson²; to Zoran Rilak for his moral support and for lending his computer-wizardly hand with programming problems; and to my colleagues at the Devonshire hall of residence.

Last but not least, my gratitude to a “low-energy” theoretician Dr. Edward Pope for his willingness to listen patiently to some painfully detailed explanations of various ‘high-energy’ modelling issues (even though they concerned particles!), for reading my thesis and giving useful comments and for making me laugh, even during the final writing-up times.

¹for feeding me cookies and other various lovely food in those famished writing-up times

²for cheering me up during some long hours in our astro-office/saving me from bankruptcy by returning my books to the library during my journeys to the Whipple telescope site

Abstract

The temporal evolution of multi-wavelength spectra from TeV blazars is modelled. The characteristic double-peaked spectral shape seen in blazar activity is reproduced. The radiation is assumed to originate in an evolving pair plasma that populates a compact, ultra-relativistic emission region moving outwards along the AGN jet axis in a randomly oriented, uniform magnetic field. The TeV component is explained through the Inverse Compton upscattering of the self-produced synchrotron photons and of the photons originating externally to the jet. The accretion disc and the Broad Line Region are considered as the sources of soft external target photons. The effects of the emission region's passage through the Broad Line Region on the evolution of the observed spectra have been investigated in this study. The emission region is modelled as a homogeneous spherical blob that is populated by isotropic particles which subsequently cool radiatively. For the calculation of the observed spectra, time-travel effects within the blob volume are taken into account, producing the observed spectra that are correctly treated as a superposition of spectra from different epochs, for each instance in time. In the treatment of the Inverse Compton Scattering, the full Klein-Nishina cross-section has been taken into account, allowing to model the radiation from the highest-energy particles without the usual approximations. Other effects, such as the synchrotron self-absorption, the pair production of the generated TeV photons on ambient fields and the extinction of the TeV light by the extragalactic background light have been taken into account. Particle energy losses at a single energy are not approximated with an average energy loss at every energy, but (for the first time, to the author's awareness) with a distribution function over a range of energies. To reproduce the photon spectra self-consistently from the evolving particle distribution, a detailed, fast numerical code has been developed, that relies on the kinetic-equation solving approach, in the hope of using it to fit the future time-resolved spectral observations. Predictions of the lightcurves and the averaged photon spectra have been made on timescales of 10 - 30 min in expectation of the results from the current generation of Cherenkov telescopes (HESS, MAGIC, VERITAS), along with the detailed coverage from the X-ray missions (XMM) and the previously uncharted intermediate range (GLAST).

Contents

List of Figures	iv
List of Tables	v
List of Abbreviations	vi
1 Introduction	1
1.1 Unified Model & AGN Paradigm	2
1.2 Jets in AGN	6
1.3 Blazars	10
1.3.1 The Blazar Sequence	13
1.3.2 Variability	15
1.3.3 Relativistic Effects	17
1.4 Models of Jet Radiation	21
1.4.1 Difficulties of the Current Models	23
1.4.2 External Compton Models	27
1.5 This work	30
2 Radiative Processes	33
2.1 Inverse Compton Scattering	34
2.2 Synchrotron Spectrum	40
2.2.1 Synchrotron Self-Absorption	42
2.2.2 Razin-Tsytoich Effect	45
2.3 Pair Production	45
3 Target Fields	50
3.1 Synchrotron Photons	50
3.2 Accretion Disc Photons	52
3.3 Broad Line Region Photons	55
3.3.1 Position of the blob relative to the BLR	59

CONTENTS

3.3.2	Monoenergetic Approximation for BLR Radiation	61
3.3.3	Estimating the BLR radius	63
4	Temporal Evolution of Particle and Photon Spectra	66
4.1	Continuity equations for electron spectra	67
4.2	Coefficients	68
4.3	Observed Spectrum	71
4.4	Numerical Treatment of Temporal Evolution	73
4.5	Examples of spectra	74
5	Simulations of Observed Photon Spectra	85
5.1	Timescales for relevant processes	87
5.2	Simulations	87
5.3	Discussion of Scenarios and Limitations	106
6	Summary and Conclusions	109
A	Coefficients	114
B	Approximation for small $\frac{\mu_+ - \mu_-}{\mu_+}$	116
	Bibliography	119

List of Figures

1.1	The current paradigm for radio loud AGN	3
1.2	Unification scheme for AGN	4
1.3	The jet propagation through ambient medium	7
1.4	Blazar sequence	13
1.5	Spectral variability of Mrk 421	16
1.6	Relativistic beaming	19
1.7	Models of the gamma-ray production in relativistic jets	22
1.8	Photon spectra of Mrk 421, Mrk 501, PKS 2155 and 1ES 1101 by Katarzynski et al. (2006)	24
1.9	X-ray – TeV correlation and orphan flares	26
1.10	Whipple vs. VERITAS	28
2.1	Relative rate for a parallel beam of target photons scattering with the monoenergetic electrons	38
2.2	Synchrotron spectrum	43
2.3	Attenuated synchrotron intensity spectrum	44
2.4	Optical depth due to the accretion disc photons and BLR photons (Halpha and Hbeta)	48
3.1	Upsscattered synchrotron radiation by a power-law distributed elec- trons	51
3.2	Upsscattered disc radiation by a power-law distributed electrons .	54
3.3	Unboosted and boosted incoming number densities plotted against the incoming angle	56
3.4	The schematic representation of the model of the Broad Line Region	59
3.5	Upsscattered BLR radiation by a power-law distributed electrons .	62
3.6	Spectra due to BLR photons radiated at Halpha and at Hbeta line	64

LIST OF FIGURES

4.1	Comparison of individual instantaneous photon spectral components with other authors	74
4.2	Evolving electron spectrum	75
4.3	Evolving instantaneous photon spectrum due to synchrotron, accretion disc EC and SSC losses	76
4.4	Evolving instantaneous photon spectrum due to synchrotron, accretion disc EC and SSC losses, after accounting for the finite size of the emitting region	77
4.5	Overall spectra due to synchrotron, accretion disc EC and SSC losses	78
4.6	Comparison of the SSC model with other authors	81
4.7	Averaged observed photon spectra for Mrk 421 and Mrk501	82
4.8	Averaged observed photon spectra for PKS 2155 and 1ES 1101 . .	83
4.9	Optical depth due to EBL from Kneiske et al. (2004) model . . .	84
5.1	Evolving photon and electron spectra, 0.5 mpc	89
5.2	Evolving photon and electron spectra, 2 mpc	90
5.3	Evolving photon and electron spectra, lower magnetic field	92
5.4	Evolving photon and electron spectra, bigger blob radius	93
5.5	Evolving photon and electron spectra, lower electron number density	95
5.6	Evolving photon and electron spectra, higher maximum cut-off of the electron spectrum	96
5.7	Evolving photon and electron spectra, higher minimum cut-off of the electron spectrum	97
5.8	Evolving photon spectrum, starting distance of 2 mpc and 5 mpc	99
5.9	Evolving electron spectrum, flux fall-off times	100
5.10	X-ray and TeV lightcurves	103
5.11	Evolving photon and electron spectra, acceleration term included, starting distance of 2 mpc	104
5.12	Evolving photon spectrum, starting distance of 2 mpc	105

List of Tables

1.1	Identified extragalactic TeV sources as of end 2008 (from Weekes 2008).	11
1.2	Typical observed peak positions in different types of blazars. . . .	14
5.1	Input parameters for the simulations	88
5.2	BLR input parameters	101

List of Abbreviations

ADAF	Advection-Dominated Accretion Flow
ADIOS	Advection-Dominated Inflow-Outflow Solution
AGN	Active Galactic Nucleus
BAL QSO	Broad Absorption Line Quasi-Stellar Object
BLR	Broad Line Region
BRLG	Broad Line Region Galaxies
CGRO	Compton Gamma-Ray Observatory
EBL	Extragalactic Background Light
EC	External Compton
EGRET	Energetic Gamma Ray Experiment Telescope
ERF	Electron Rest Frame
EUV	Extreme Ultraviolet
FR I	Fanaroff-Riley I
FR II	Fanaroff-Riley II
FSRQ	Flat Spectrum Radio Quasars
GLAST	Gamma-ray Large Area Space Telescope
HBL	High-peaked BL Lac
HEGRA	High Energy Gamma Ray Astronomy

HESS	High Energy Stereoscopic System
HPQ	Highly-Polarised Quasar
IBL	Intermediate-peaked BL Lac
IC	Inverse Compton
ICS	Inverse Compton Scattering
IG	Inter-Galactic
IR	Infrared
IS	Inter-Stellar
LBL	Low-peaked BL Lac
LPQ	Lowly-Polarised Quasar
MAGIC	Major Atmospheric Gamma-ray Imaging Cherenkov Telescope
Mrk 421	Markarian 421
Mrk 501	Markarian 501
NELG	Narrow Emission Line Galaxy
NLR	Narrow Line Region
NLRG	Narrow Line Region Galaxy
QSO	Quasi-Stellar Object
RXTE	Rossi X-ray Timing Explorer
SED	Spectral Energy Distribution
SMBH	Supermassive black hole
SSC	Synchrotron Self-Compton
SSRQ	Steep Spectrum Radio Quasars
UV	Ultraviolet

LIST OF TABLES

VERITAS Very Energetic Radiation Imaging Telescope Array

VHE Very High Energy

VLBI Very Long Baseline Interferometry

XMM X-ray Multi-mirror Mission

Chapter 1

Introduction

Although studied extensively for over 40 years, Active Galaxies remain one of the most impenetrable puzzles of astronomy. These mesmerising objects are ascribed a large number of superlatives – the most energetic, the most luminous, the most distant objects known, the youngest galaxies observable, the most powerful accelerators. Relatively rare, constituting only a few percent of all known galaxies, they are invaluable sites for examining the most extreme physical conditions and processes, and also our primary probes of the edges of the observable Universe and, correspondingly, its early epochs. Although having been observed at all redshifts, they seem to be far more numerous at the higher ones, the fact that may suggest their connection to the galactic evolution. Regardless of this, their abundance at high redshifts seems to imply that this evolutionary phase can persist for about 100 million years. In the most extreme cases, this gives us the opportunity to get an insight into the formation and early evolution of the Universe’s firstborn galaxies, only a billion years after Big Bang. Furthermore, AGN also seem to play an important role in heating the X-ray emitting atmospheres of elliptical galaxies and clusters of galaxies, thereby controlling the growth of large galaxies even at comparatively small redshifts.

The intrigue of these objects comes from their innermost region, the Active Galactic Nucleus (AGN). These are known to be as small as the Solar System, yet show traits of enormous and often variable activity, sometimes outshining the rest of their hosts and appear to radiate alone as much energy as thousands of normal galaxies. It was realised early on that the amount these objects radiate in the blue – UV regime could not be due to starlight, not even due to the radiation from the most extreme stars (temperature- and mass-wise). And even though there is

1.1. UNIFIED MODEL & AGN PARADIGM

still a small minority of models which attempt to explain this peculiar behaviour with supernovae or starburst activity, it is nowadays widely accepted that these enormous observed bolometric luminosities, ranging from $10^{40} - 10^{49}$ erg/s, can only be generated through a highly efficient process. The natural explanation is the gravitational energy release from the galactic gas and dust accreting onto the central supermassive black hole (SMBH), and its conversion into radiative energy. This process has a potential of reaching efficiencies as high as 40% (Eddington limit for a spinning, Kerr black hole), as opposed to less than a percent for the thermonuclear reactions that occur in stars. The masses of such gargantuan black holes, as inferred from observed luminosities, range from millions to several billion solar masses.

This chapter provides a background to the field of AGN physics, and more specifically the subgroup of blazars, that this thesis is concerned with. The second chapter gives an overview of relevant radiative processes. In the third chapter the radiation fields in AGN are discussed with the details of the geometry of relevant regions and their parameters, while their interactions with the jet radiation and the subsequent evolution of the particle population are outlined in the fourth chapter. The fifth chapter presents and discusses various simulations with different scenarios that reproduce the observed rapid variability (flares) from blazars. The last chapter provides a summary and an outlook.

1.1 Unified Model & AGN Paradigm

AGN come with a wide variety of observational signatures. Historically, they have been sorted into many different schemes, based on either one or a combination of various classification criteria, such as the morphological and spectral properties, total power radiated and variability. This has led to a very user-unfriendly nomenclature, confusing to any newcomer to the field. Today, the zoo of observed AGN is interpreted within the *Unified Model of AGN* to be due to a combination of orientation and obscuration effects, as well as some intrinsic variations in the individual object's characteristics, such as power, central black hole mass and ambient conditions (see figure 1.1). In addition, these parameters may be intercorrelated, and may bear a connection to the evolutionary stage. Spectra of AGN are particularly complex and can have a number of characteristic features. The 'blue bump', often visible in UV and soft X-ray (usually peaking in hard-

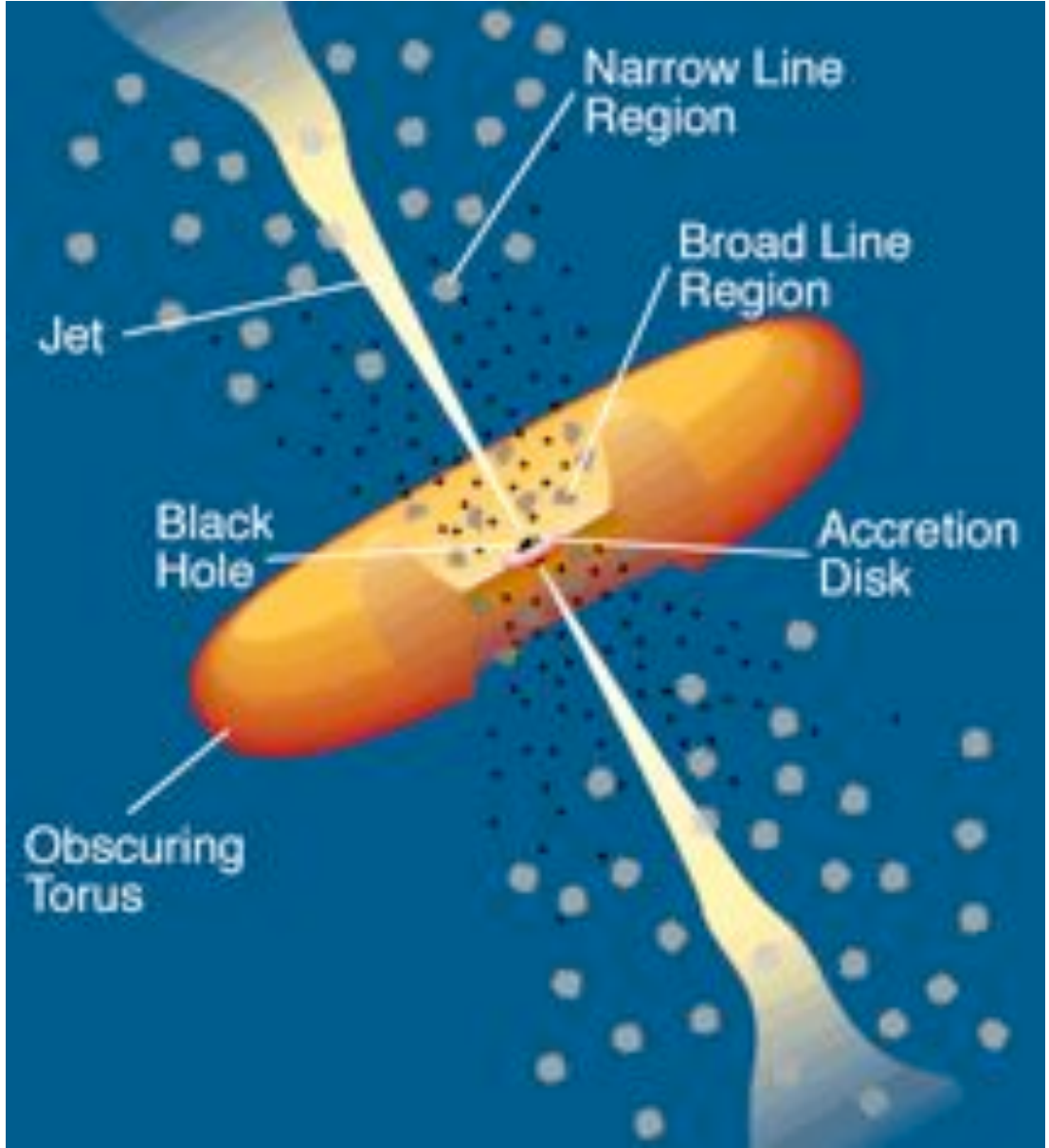


Figure 1.1: The current paradigm for radio loud AGN (adapted from Padovani 1998). The accretion disc surrounds the central SMBH, and it stretches out to about 100 gravitational radii, where it extends to a compact molecular torus, and beyond that to a much more extended dusty torus. Above the disc there are fast moving, hot clouds of gas, that are believed to be the sources of broad emission lines. These “clouds” are so close to the central engine, that they can barely hold themselves together, due to the large gravitational effects. The signature of this region is not present in all AGN spectra, the observation explained by the obscuring torus of material that, viewed from certain directions, can be in the way. Much further away there are cooler and slower gas clouds, where the narrow lines originate from. The fact that Narrow Line Region has been observed in all the AGN provides an important evidence of the activity far enough from the centre to not be extinguished by a dusty torus.

1.1. UNIFIED MODEL & AGN PARADIGM

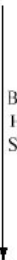

<i>Radio Loudness</i>	<i>Luminosity</i>	<i>Optical emission line properties</i>		
		<i>Type 2</i> (<i>narrow line</i>)	<i>Type 1</i> (<i>broad line</i>)	<i>Type 0</i> (<i>unusual</i>)
<i>Radio-quiet</i>	<i>Low</i> <i>High</i>	Seyfert 2 NELG IR Quasar?	Seyfert 1 QSO	BAL QSO?
<i>Radio-loud</i>	<i>Low</i> <i>High</i>	NLRG: FR I, FR II	BLRG SSRQ, FSRQ	Blazars: BL Lacs, (FSRQ)
<div style="text-align: right; margin-right: 50px;">  Black Hole Spin? </div> <div style="text-align: center; margin-top: 10px;">  Decreasing angle of the jet axis to the line of sight </div>				

Figure 1.2: Unification scheme for AGN, adapted from Urry & Padovani (1995). The classification is made on the basis of the observed emission lines, that imply the orientation effect, but also the bolometric luminosity and the radio emission, which seem to be the intrinsic features of the sources. It is not yet well understood what causes these fundamental differences in AGN, but it is often speculated that in some way the black hole spin and/or the disc accretion rate might be responsible. Observationally, almost all combinations of the three properties appear allowed (except maybe for Type 0 low-luminosity radio-quiet AGN). Edge-on viewed radio-loud AGNs (NLRG) are divided into FR I and FR II, the distinction again made on the basis of the luminosity, the former being the less luminous ones. The subdivision of high luminosity, radio loud objects of Type 1 to SSRQs and FSRQs is related to the viewing angle ($40^\circ - 15^\circ$ and $<15^\circ$, respectively). If the radio-loud objects are viewed nearly face-on, then we are looking down the jet. This class of objects is called blazars, and consists of the less powerful BL Lacs and the more powerful FSRQs.

UV, around 10 eV), is interpreted as the thermal emission from the accretion disc (existing at scales lower than a milliparsec), whereas hard X-ray is more likely to be from the disc's hot corona, and also the synchrotron radiation from the jet. There is usually a small IR bump present, which indicates (warm) dust radiation from a region further out from the centre (beyond few hundred milliparsecs). This region is often modelled with a torus, and could be a continuation of the disc. Another peculiar feature of Active Galaxies' SED is the existence of the emission lines (mostly strong Balmer and Lyman series). Two types of emission lines have been observed in these objects – broad (permitted) and narrow ones (permitted and forbidden), both Doppler-broadened. The widths of these lines indicate velocities of 1000s of km/s for broad and 100s of km/s for narrow lines. This points to the emission from dense, fast moving local condensations of gas (with densities higher than 10^9 particles per cm^3) and slower, less dense ones ($10^3 - 10^6 \text{ cm}^{-3}$), respectively, with a low covering factor (less than 10%). It is believed that these gas clouds (as they are usually referred to) are moving above the accretion disc, the faster ones being closer at scales of a few milliparsecs to a few tens of milliparsecs, and the slower ones further out, above a few hundred milliparsecs. The two regions are appropriately named Broad Line Region (BLR) and Narrow Line Region (NLR). These gas clouds are ionised/collisionally excited by the continuum from the central engine, with ionising parameters of $0.03 - 1$ and $10^{-2} - 10^{-3}$, respectively (for an overview of AGN characteristics see Robson 1996). They reprocess the incoming continuum, which is why the resulting BLR spectrum can somewhat resemble that of a thin accretion disc (whose generic feature is a quasi-thermal peak in UV – EUV), showing a “blue bump” in optical and UV and a strong edge at the Lyman limit.

Galaxies with only narrow lines have been observed (labelled Type 2, where Type 1 contains both kinds of lines), but none with only broad lines have been detected. This points to orientation/obscuration effect – Type 2, seen almost edge on, have the BLR hidden inside the dusty torus (inner radius of the order of maybe 100 mpc), while Type 1, at intermediate angles to the line of sight, reveal both regions. This picture is further reinforced by the fact that Type 2 exhibits a weak continuum, as opposed to the bright one in Type 1 AGN, in which the light from the central engine is not extinguished by the torus. Another distinctive type of AGN in this spectroscopic classification, Type 0, comprises those objects that show signs of weak or unusual emission (and sometimes absorption) lines.

1.2. JETS IN AGN

In some of the AGN broad lines are detected in polarised light, which is usually interpreted to be due to the extinction by a compact molecular torus existing just outside the BLR (see figure 1.2 for the unification scheme).

Radio Loudness. A percentage of AGN (10 – 15%) display strong radio emission. Based on their power output in radio, the distinction is made between radio-quiet and radio-loud sources, noting that the radio-quiet category does not necessarily mean absence of radio emission but only a very low radio luminosity, as compared to the optical one. Radio-loud AGN have a ratio of radio to optical luminosity greater than 10. The spectra of the radio-loud sources display a power law emission that spans over many orders in energy, extending from radio to X-ray, and sometimes even TeV gamma-ray band. This emission is associated with the collimated, twin outflows of plasma – jets – that emerge from the vicinity of the SMBH at relativistic speeds, and extend deep into the galactic halo.

1.2 Jets in AGN

Jets are ubiquitous phenomena in the Universe, found in active galaxies, Gamma-Ray Bursts, Young Stellar Objects, protoplanetary nebulae, microquasars and X-ray binaries. Even our own Milky Way shows signatures of a weak jet. Jets are associated with accretion flows.

The material in the disc needs to lose angular momentum for the material to be able to spiral down to the very central regions of the disc and eventually fall into the black hole. In the accretion process, the luminosity output of the central region is generated by the conversion of the gravitational potential energy of the accretion disc into radiation, via viscous dissipation in the disc. As the gas moves inwards, it is heated because of the friction, e.g. due to ion or magnetic viscosity, and radiates energy. Gravitational potential energy goes into the kinetic and thermal energy of the accreting gas. The angular momentum is transported outward, allowing the gas to spiral inward towards the black hole.

The plasma viscosity of the disc is far too low to provide sufficient angular-momentum transfer that would allow the material to flow inwards. However, a solution has been found in the form of turbulence caused by the magnetorotational instability, with growing observational evidence backing the computer simulations that show that accretion is not supported hydrodynamically but magnetically (for a recent overview of accretion models and observations see e.g. Balbus 2006,

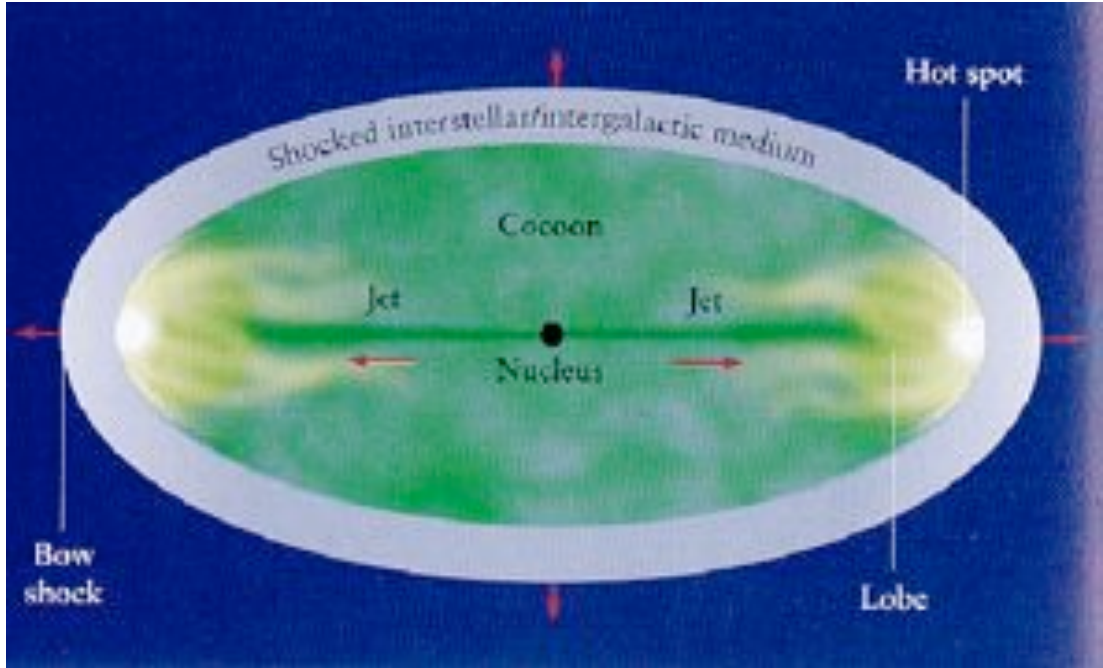


Figure 1.3: The jet propagation through ambient medium (from Begelman & Rees 1996).

Hubbard & Blackman 2008). Magnetorotational instability arises in a magnetised fluid when the angular velocity decreases with the increasing distance from the centre of rotation. This differential rotation occurs in Keplerian discs (which obey Kepler's laws of motion under the gravitational effect of a massive central body). Two adjoining fluid parcels at consecutive radii move at different speeds and as they move apart, magnetic field acts as the tension, slowing down the inner element, which consequently moves to a lower orbit, and speeding up the outer, moving it to a higher orbit. This way the angular momentum is transported outwards.

If the accreting gas can cool efficiently, it will form a thin accretion disc. This would lead to luminous sources. Yet there are sources for which the observed disc radiation spectrum indicates that this is not what happens, which argues for the radiatively inefficient, thick accretion discs. In this case the gas stores most of the thermal energy and carries it in the form of entropy over the event horizon of the black hole as it accretes, and so we observe the radiation from the advection-dominated accretion flow – ADAF (Narayan & Inoué 1994). This predicts low-luminosity sources. However, these models fail to explain the flat broadband spectra of blazars. To solve this, ADAF solution was modified to

1.2. JETS IN AGN

allow for the powerful outflow, such as wind or a jet (ADIOS, see Blandford & Begelman 1999), that would extract the excess angular momentum in the vicinity of the black hole, so that the gas could accrete onto it.

Jets in the scope of the Unified Model. A notable signature of jets is their radio power. Radio sources in AGN display emission that is either extended, typically having a steep spectrum, or compact, usually with a flat spectrum. *Extended* sources comprise two distinctive morphological subtypes, which were found by Fanaroff and Riley to be linked with the radio luminosity, and so were named after them: FR I and FR II. In the first class are the less luminous radio sources, with the jets that are brightest closest to the central engine, growing fainter towards the lobes. They can start off as being one-sided close to the centre, but on a kpc scale they become two-sided. FR II, on the other hand, are strong radio sources with “hot spots” in their lobes, which are very distinctive features that are much brighter than their cores and jets, which themselves are much brighter than their FR I counterparts. FR II jets are one-sided not only at small (VLBI) scales, but also on kpc scales, displaying a typically smooth structure as opposed to the often irregular FR I jets. The large-scale differences in these features are normally interpreted as a distinction between the supersonic (FR II) or subsonic flows (FR I), which could in turn lead to a lesser or greater susceptibility to distortion by the ambient medium. It is not clear whether all flows start off as being supersonic. However, flows have been observed to decelerate on their way outwards, from the galactic centre. Another possibility is that there is a physical distinction not in the density of the ambient medium that slows the jets down, but in the way the AGN engine produces the jets. For an overview on FR classification see Kembhavi & Narlikar (1999).

Compact sources come in many flavours, but the interesting ones are the core-jet sources, with a flat-spectrum core and a steep-spectrum jet. It is interesting to note that the flat-spectrum sources normally have blazars and quasars as their hosts, and the steep-spectrum objects tend to be of FR I or FR II type. These observations lead to the unification theory, according to which different observational phenomena stem from a combination of some intrinsic characteristic, such as the host luminosity, and our orientation with respect to the jet axis. The orientational argument is further supported by the fact that all of the extended sources have a compact central component, and all of the compact have faint “halos”, interpreted as the extended sources seen pole-on. A compact radio jet is

found on the pc scale, and has a “core” at its base, from which series of knots of emission is moving outwards (seldom the stationary ones are observed), towards the extended, kpc-scale jet and lobes.

Jet Propagation. As the collimated relativistic plasma (jet) develops, it expands first into the interstellar, and then into the intergalactic medium of the galaxy (see figure 1.3). The pressure that the external medium exerts onto the tip of the jet will result in this ending point moving slower than the flow internal to the jet, resulting in a shock. This shocked jet material is responsible for the observed hot spots. When the material from the jet hits the hot spot, it can only go back towards the nucleus, and in doing so it creates a “cocoon” around the source, that is much wider than the jet itself. In the process it forms the lobe of radio emission at the end of the jet, the brightest region of which is the hot spot. The cocoon itself is enveloped with the region of the shocked ambient material, and there is a contact discontinuity between them. There is also a bow shock, produced by the expansion of the cocoon into the external medium. The region of shocked IS/IG medium material lies behind this bow shock (see Begelman & Rees 1996).

Acceleration Mechanism. There are various theories of jet acceleration (for an overview of acceleration and collimation models see Sauty et al. 2002). *Hydrodynamic acceleration* treats a jet as an adiabatic fluid propagating in an external medium with decreasing pressure. *Radiative acceleration* would result from the intense radiation field of the disc. *Hydromagnetic acceleration* seems to be a favourite of many: power is extracted from the radiation of the disc and/or spinning black hole, and the flow is threaded by a large-scale magnetic field. There are several variations to this scenario. In the *toroidal acceleration* scenario, the magnetic field is spiral and it originates in the disc. As it stretches out, the toroidal magnetic pressure builds up due to the rotation of the field lines. The net force is pushing plasma outward. *Magneto-centrifugal acceleration from the disc* would be due to the combination of centrifugal force and strong poloidal magnetic field (Blandford-Payne mechanism, Blandford & Payne 1982). Magnetic field lines thread the disc, going into its corona, and the disc’s differential rotation leads to a horizontal component of the magnetic field. As the field lines drag the corona around, the angular momentum is transferred from the disc into the corona. In the *magneto-centrifugal acceleration from the magnetosphere of the black hole* (Blandford-Znajek process, Blandford & Znajek 1977) the rotational

1.3. BLAZARS

energy of a Kerr black hole is extracted by a large scale magnetic field that is accreted onto the black hole. The potential difference that forms between the equator and the poles causes the electric current flows along the field lines from the event horizon towards the poles of the black hole, making it a battery of sorts. This current releases energy into the plasma, accelerating the particles and carrying them away from the poles in the form of bipolar outflows or jets (a PhD thesis by Costamante 2001 gives a useful overview section on jet acceleration models).

Collimation Mechanism. On larger scales, the magnetic field is known to be parallel to the jet axis in FR I, and perpendicular in FR II. This gives us some clues about the possible collimation mechanisms. *Pressure confinement* of the surrounding medium, if its pressure is higher than that of the flow. This works only for rich environments such as clusters of galaxies (e.g. in FR I, but not in FR II). In the *toroidal magnetic confinement* model (Blandford 1976), the toroidal magnetic field, that is created by the rotation of the disc material, collimates the outflow around the rotational axis. The advantage of this model is that it works for both over- and under-pressurised jets. Thermal & magnetic processes may be combined to accelerate and confine the outflow.

1.3 Blazars

One feature that is seen in a small number of radio-loud AGN is the double peaked SED (in νF_ν representation), with one broad maximum in the optical – X-ray part of the spectrum, commonly believed to be due to the synchrotron radiation of particles, and the other at higher, gamma-ray energies, usually ascribed to the Inverse Compton upscattering of photons by highly relativistic electrons in the jet. These objects are called blazars, and their peculiar spectrum is understood to be a consequence of the radiation from their jets that happen to be aligned with our line of sight. The relative orientation causes the radiation to appear relativistically beamed to us and hence boosted in flux, so we can observe even those objects that would otherwise be undetectable. Therefore the phenomenon of blazars (within the AGN group) is actually an orientation effect. The most extreme among them are called BL Lacs, with very weak line emission and the higher peak which can extend up TeV energies and strong and often rapid variability in continuum emission.

Table 1.1: Identified extragalactic TeV sources as of end 2008 (from Weekes 2008).

Catalog Name	Common Name	Redshift	Flux at 1 TeV $10^{-12} \text{ cm}^{-2} \text{ s}^{-1} \text{ TeV}^{-1}$	Index	Classification	Discovery Group/Date
TeV1231+124	M87	0.00436	1	2.9	FRI	HEGRA/2003
TeV1104+382	Markarian 421	0.031	12-97	2.4-3.1	LBL	Whipple/1992
TeV1654+398	Markarian 501	0.034	0.5-100	1.9-2.3	LBL	Whipple/1996
TeV2347+517	IES2344+514	0.044	1-5	2.3-2.5	LBL	Whipple/1998
TeV1136+702	Markarian 180	0.045	0.9	3.3	LBL	MAGIC/2006
TeV2000+651	IES1959+650	0.048	4-120	2.7-2.8	LBL	Tel.Arr./2000
TeV0551-323	PKS0548-323	0.067	0.3	2.8	LBL	H.E.S.S./2007
TeV2203+423	BL Lacertae	0.069	0.3	3.6	LBL	Crimea/2001
TeV2009-488	PKS2005-489	0.071	0.2	4	LBL	H.E.S.S./2005
TeV0152+017	RGB J0152+017	0.080		2.95	LBL	H.E.S.S./2008
TeV1221+283	W Comae	0.102		3.81	IBL	VERITAS/2008
TeV2159-302	PKS2155-304	0.117	2-3	2.3-2.5	LBL	Durham/1999
TeV1429+427	H1426+428	0.129	1-2	2.6-3.7	LBL	Whipple/2002
TeV0809+524	IES0806+524	0.138			LBL	VERITAS/2008
TeV0233+203	IES0229+200	0.140	0.62	2.5	LBL	H.E.S.S./2006
TeV2359-306	H2356-309	0.165	0.3	3.1	LBL	H.E.S.S./2006
TeV1221+302	IES1218+304	0.182	1.3	3.0	LBL	MAGIC/2006
TeV1103-232	IES1101-232	0.186	0.4	2.9	LBL	H.E.S.S./2007
TeV0349-115	IES0347-121	0.188	0.45	3.1	LBL	H.E.S.S./2007
TeV1015+495	IES1011+496	0.212	0.3	4.0	LBL	MAGIC/2007
TeV1556+112	PG1553+113	0.3-04	0.1-0.2	4.0	LBL	H.E.S.S./2006
TeV0219+425	3C66a	0.444			IBL	Crimea/1998
TeV1256-058	3C279	0.536	-	4.1	FSRQ	MAGIC/2008
TeV0716+714	S50716+714	?			LBL	MAGIC/2008

1.3. BLAZARS

EGRET, the gamma-ray experiment on the satellite CGRO (Hartman et al. 1999) operating between 20 MeV and 30 GeV, has discovered more than 70 gamma-ray blazars (FSRQs). The ground-based Cherenkov detectors, such as Whipple (see Weekes et al. 1989 and the more recent Kildea et al. 2007) and HEGRA (Daum et al. 1997), have complemented it with the observations in the TeV range. This generation of gamma-ray telescopes has detected six BL Lac objects, and the present generation of detectors, such as VERITAS (Weekes et al. 2002), HESS (Hinton 2004) and MAGIC (Lorenz & Martinez 2005), have discovered many more TeV sources as of end 2008 (see Weekes 2008). Most of the known extragalactic TeV emitters are HBL, but there are also a few representatives of IBL (W Comae and 3C66a), an LBL (BL Lacertae), an FR I (M87) and an FSRQ (3C279). All of these objects are listed here in table 1.1.

Blazars are characterised by a spectral distribution that shows two prominent peaks. EGRET selected blazars with the second peak in GeV have the first peak in radio, and the TeV blazars reveal a lower peak in the X-ray band. For two of the sources (Mrk 421 and Mrk 501) the emission extends even beyond 10 TeV.

For an object to be classified as a blazar, it has to contain signatures of a jet (Costamante 2001; Skelton 1999):

- in radio: compact core emission, with a flat spectrum
- broad band spectrum that is bright in all frequency bands: radio – GeV, and sometimes extends to multi-TeV
- strong, rapid variability in all bands
- superluminal motion of radio-compact regions, or “blobs”, as measured with VLBI – pc-scale jet (relativistic effect)
- one-sided jets (due to the relativistic effects: just as the jet approaching us would appear brighter than it actually is, for the same reasons the receding jet will appear greatly diminished)

Emission lines in optical are weak or absent in most of such sources. These objects are also known to often show strong, variable linear polarisation of radio and optical emission.

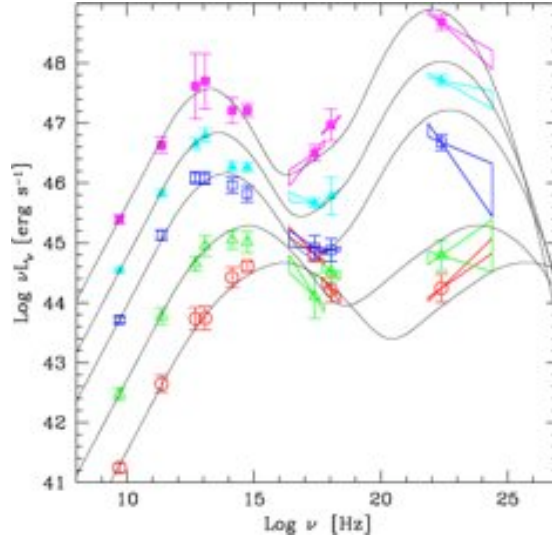


Figure 1.4: Blazar sequence proposed by Fossati et al. (1998). The main premise is that one parameter – blazar power – governs the SED shape and peak positions. Blazar sample has been divided into five radio luminosity bins and the overlaid curves represent the phenomenological fits to the data. The plotted luminosity is inferred from the observed flux as if the object was emitting isotropically in the observer’s frame, hence boosted by an unknown Doppler factor to the power of four (δ^4).

1.3.1 The Blazar Sequence

Blazars are commonly further subdivided into BL Lacs and FSRQs. BL Lacs were named after a prototype of such objects, BL Lacertae, and the reason for classifying them as a separate type lies in the absence of strong emission lines. It is not yet understood why the emission lines are so weak in these objects, but it is often taken to be linked to the low luminosity of the disc, which illuminates the BLR. On average, luminosities of BL Lac objects seem to be lower than those of FSRQs, and a trend has been observed where both the synchrotron and IC peaks shift as an inverse function of luminosity and the gamma-ray dominates increasingly over X-rays with higher luminosities. Fossati et al. (1998) and Ghisellini et al. (1998) have proposed the so-called *Blazar sequence* based on the inter-correlation of these three parameters.

The phenomenological sequence by Fossati et al. (1998) was derived from the observed anti-correlation of the radio luminosity, which traces well the bolometric luminosity, and both the peak frequency of blazars and the X-ray to gamma-ray flux ratio. The theoretical background was provided by Ghisellini et al.

1.3. BLAZARS

Table 1.2: Typical observed peak positions in different types of blazars.

	1st peak	2nd peak
new?	MeV	TeV
HBL	soft EUV – soft X-ray	GeV – TeV
LBL	IR – optical/UV	MeV – GeV
HPQ/LPQ	mm – FIR	MeV

(1998), and their physical sequence is a result of the different contributions to ICS from the target photon fields external to the jet in objects with different radio (and bolometric) luminosities. Since high-luminosity objects have more luminous BLRs, the EC component should be more important than the SSC, thus providing stronger cooling and producing the higher gamma-ray fluxes w.r.t. the synchrotron peak. The fact that the peak frequency is lower in these objects is again due to the stronger cooling of particles in these objects, if the peak is taken to represent the balance of the acceleration and cooling processes. TeV blazars, on the other hand, are supposed to have negligible contributions from their small BLR and thus the lower IC peak (typically observed to be comparable to the synchrotron peak), which in this scenario almost purely consists of the SSC photons. Weaker cooling also keeps the peak frequency relatively high. However, it should be noted that the data used to constrain their model have been compiled over a long period of time, and mostly not even contemporaneous at different wavelengths. It is thus a superposition of the observations from many individual flares, which are known to behave differently even for a same object.

A classification has been proposed (Ghisellini 1999) that encompasses high-frequency and low-frequency peaked BL Lacs, HBLs and LBLs, and highly- and lowly-polarised quasars, HPQs and LPQs (see table 1.2). LBLs are observed to have their lower peak in the IR – UV region, while HBLs' first peak lies in MeV – GeV region. Their IC peaks are, respectively, in EUV – soft X-ray region, and GeV – TeV region. The proposed blazar sequence is shown on figure 1.4.

This sequence has since been much debated, and it appears to be increasingly obvious that it suffers from strong selection effects (Padovani 2007 discusses these problems). Radio luminosity – peak frequency anti-correlation is only achieved when combining observations from three different samples (HBL were mostly X-ray selected, LBL were mostly radio selected and FSRQ were only radio selected),

and is not seen in homogeneous samples. All the subsequent studies, from the surveys that were not subject to selection effect, have shown no correlation, very large scatter (several orders of magnitude, at each peak frequency) and the outliers (sources in the regions of the plot that were empty in the original study by Fossati et al. (1998)), implying that even if any correlation exists, it is quite weak. Moreover, results from Nieppola et al. (2008) indicate that the blazar sequence seems to be an observational phenomenon, by accounting for the different Doppler factors across the sequence. They study the correlation between the de-boosted synchrotron peak position and luminosity by deriving the Doppler factors from the variability timescales. The Doppler factor and the synchrotron peak position are found to be strongly correlated, having the lower energy sources being boosted more. After accounting for the Doppler boosting, the observed anti-correlation between the synchrotron peak position and the synchrotron luminosity becomes a direct correlation, and it is markedly strong in BL Lacs.

1.3.2 Variability

Blazars are also known to display strong variability over the whole of their SED, from radio to TeV gamma-rays. The variability timescales and the amplitude changes vary greatly. The timescales range from years down to minutes, with the longer ones being typical for the radio to optical part of the spectrum, where they are observed to be of the order of days up to several years (see Ulrich et al. 1997). On the other hand, X-rays and gamma-rays can vary in flux in a matter of hours, with the TeV flares being the most dramatic ones, with flux doubling times as short as half an hour. A certain portion of sources also seem to produce the Intra-Day Variability (IDV) in all wavebands, even at the lowest energies (see Wagner & Witzel 1995). The observed timescales put constraints on the size of the emitting region, which, once corrected for the Doppler boost, turns out to be surprisingly small, and can be (in our frame) of the order of light hours (about tenth of a milliparsec), and in some cases (Mrk 421, Gaidos et al. 1996) less than an hour (in the co-moving frame of the emission region this translates into about 10 – 50 times larger region, depending on its the velocity and the viewing angle). The most extreme cases recorded yet were in the Mrk 501 flare from 2005 and the PKS 2155 one from 2006 (Albert et al. 2007; Aharonian et al. 2007), where the variability timescales were of the order of only a few minutes, which put extreme

1.3. BLAZARS

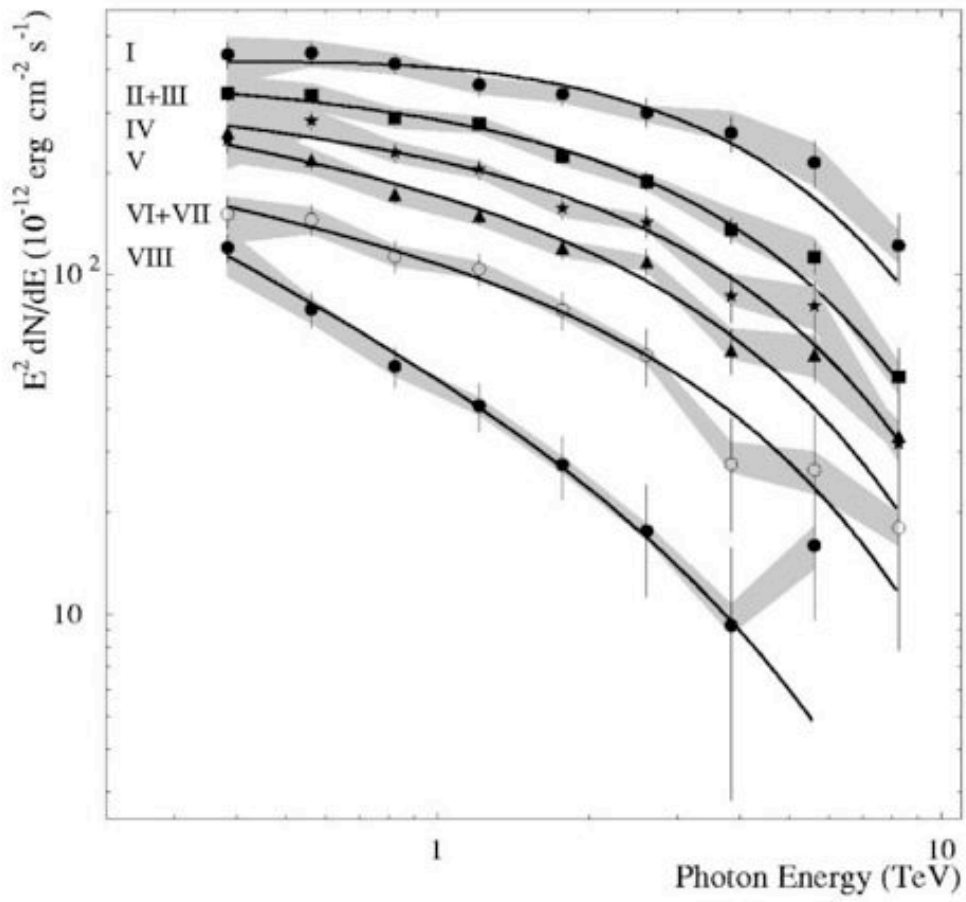


Figure 1.5: Spectral variability of Mrk 421 (from Krennrich et al. 2002). The spectral shape hardens with the increased flux.

requirements of the Doppler boosting factor (from over 50 to over a 100 in PKS 2155).

During the flares, blazars are observed to have greater amplitudes in the high-energy spectral component than in the low-energy one (Wehrle 1997). In addition, the flux changes are energy dependent within each of the two spectral components, having the greater amplitude increase with the higher photon energy (Sikora et al. 1997). Rapid variations in blazar SEDs imply a very compact emission region that is moving toward the observer with highly relativistic speeds (Blandford & Königl 1979). They are believed to be due to the shock propagation in jets. Shocks are commonly thought to be responsible for the acceleration of the jet emission region particles, since the first order Fermi acceleration (commonly invoked to model shocks) produces the slope of the accelerated particle distribution $p = 2$ for strong non-relativistic shocks¹. However, this is not an appropriate value to use for ultra-relativistic shocks, which were found to be somewhat steeper, up to $p = 2.4$ (see Kirk & Schneider 1987). The rough relationship between the slope p of the particle number density spectrum and that of the slope s of the observed photon (energy) spectrum is given by $p = 2s + 1$.

1.3.3 Relativistic Effects

Relativistic motion leaves its imprints on the observed SED in the form of several observational effects associated with blazars. One-sided jets, prohibitively high fluxes and superluminal motion are some of the effects that cannot be accounted for unless one introduces an emission region that is moving relativistically along the jet closely aligned to our line of sight².

The aberration effects that we observe stem from the fact that the jet emission region moves at speeds comparable to light speed at a small angle to the line of sight during our measurements. This essentially leads to the jet nearly catching up with its previously emitted photons (see figure 1.6). This will affect the time measurements, shortening the time intervals in the observer's frame with respect to the time intervals in the rest frame of the emission region, which will cause the observer to see larger fluxes. Such high fluxes would be impossible to get out of the emission regions this small (as inferred from the light-crossing constraints)

¹ p is actually the absolute value of the particle slope, which is always negative; the same is true for the photon energy spectrum slope s .

²The idea was first introduced by Martin Rees back in 1967.

1.3. BLAZARS

because of the transparency arguments – opacity would be so large that gamma-rays and X-rays would pair produce, hence gamma-rays would not escape and be observed, and there would be an excess of X-rays (see Ghisellini & Madau 1996). Apparent superluminal motion, which was measured in many sources by VLBI to be up to 40 times that of the light speed, is also caused by the shortening of the observed time interval.

Beamed Emission

Consider a source that is at the point A when it emits a signal that reaches a stationary observer after the interval Δt_A (figure 1.6), crossing the distance $c\Delta t_A$. In the meantime, the source has moved the distance $\beta c\Delta t$ at the angle ϕ to the line of sight, to the point B when it emits another signal that takes time Δt_B to reach the observer. Therefore the *observed interval* that has passed between the reception of signals from A and B by the stationary observer is

$$\Delta t_{rec} \equiv \Delta t + \Delta t_B - \Delta t_A = \Delta t - \Delta t \frac{v}{c} \cos \phi = \Delta t(1 - \beta \cos \phi) \quad (1.1)$$

hence shortened with respect to the time it takes the source to get from A to B. Another effect, time dilation, causes the *emission timescale* to appear longer in the reference frame of the observer than in the frame of the moving emitter by a factor of Γ

$$\Delta t_e = \Delta t'_e \Gamma \quad (1.2)$$

Therefore

$$\Delta t_{rec} \equiv \Delta t'_e \Gamma(1 - \beta \cos \phi) = \frac{\Delta t'_e}{\delta} \quad (1.3)$$

that is, the time interval that marks the time it takes the *stationary observer* to *receive* a signal emitted by a moving source contains also the retardation term of $1 - \beta_{jet} \cos \phi$ with respect to the time during which *emission* occurs in the frame of the *stationary observer* (Δt_e), and also an additional dilation factor, Γ , with respect to the time during which *emission* occurs in the frame of the *moving emitter*³ ($\Delta t'_e$). This combined effect of retardation and dilation is described by the Doppler factor δ , which is a parameter that describes the transformation of

³the corresponding power calculations, emitted and received, are calculated in accord with the appropriate time intervals.

most physical quantities between the different frames of reference

$$\delta \equiv \frac{1}{\Gamma_{jet}(1 - B_{jet} \cos \phi)} = \Gamma_{jet}(1 + B_{jet} \cos \phi') \quad (1.4)$$

where $\Gamma_{jet} = 1/\sqrt{1 - B_{jet}^2}$ is the Lorentz factor of the jet (as an example), and B_{jet} the betafactor of the jet, that is, the jet velocity in units of the speed of light. The smaller the observation angle, the more strongly the emission is beamed and the flux enhanced.

Since the aberration effects affect the angles as well, the emission patterns will be distorted. Isotropic radiation in the rest frame of the emission region (henceforth denoted with a prime) will be beamed in the forward direction in the observer's frame (unprimed quantities). The transformation of the polar angle of the photon (measured from the jet axis)

$$\cos \phi = \frac{\beta + \cos \phi'}{1 + \beta \cos \phi'} \quad (1.5)$$

$$\tan \phi = \frac{\sin \phi'}{1 + \beta \cos \phi'} \quad (1.6)$$

implies that one half of the radiation emitted isotropically in the relativistically moving region's frame, between the angles $\phi' = -\frac{\pi}{2}$ and $\phi' = +\frac{\pi}{2}$ will be concentrated in a narrow cone of the half angle $\phi \sim \frac{1}{\gamma}$, after the boosting of these angles into the observer's frame.

Below are given some of the main transformation laws (see Rybicki & Lightman 1979)

$$\nu = \delta \nu' \quad (1.7)$$

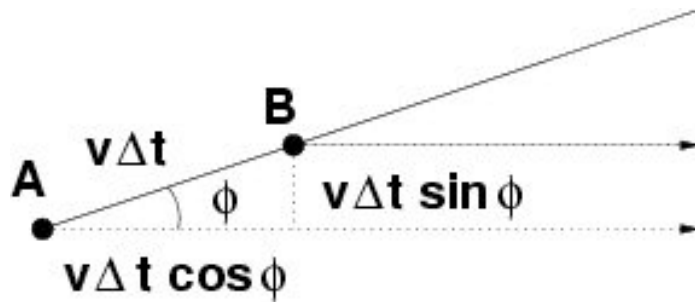


Figure 1.6: Superluminal motion

1.3. BLAZARS

for the frequency (the same as for energy) ν [Hz],

$$dV = \delta dV' \quad (1.8)$$

for the volume element dV [m^{-3}],

$$d\Omega = \frac{1}{\delta^2} d\Omega' \quad (1.9)$$

for the solid angle element $d\Omega$ [sr],

$$I(d\nu, d\Omega) = \delta^3 I'(d\nu', d\Omega') \quad (1.10)$$

for the specific intensity $I(d\nu, d\Omega)$ [$J s^{-1} m^{-2} Hz^{-1} sr^{-1}$],

$$j(d\nu, d\Omega) = \delta^2 j'(d\nu', d\Omega') \quad (1.11)$$

for the emission coefficient per unit frequency $j(d\nu, d\Omega)$ [$J s^{-1} m^{-3} Hz^{-1} sr^{-1}$]. (Note that throughout this thesis a variable that a particular quantity is a function of but not differential in will be quoted inside the bracket without the letter “d” in front of it and separated by a semicolon from the variables that the quantity is differential in⁴.)

This amplification of the jet radiation flux is an extremely important and fortunate effect, for it is the reason why we can study the blazar radiation at all.

Note that to boost the observed timescales into the co-moving frame of the relativistic emission region (and hence put constraints on its size) one would need to multiply with an appropriate Doppler factor δ as in equation 1.4. However, to obtain its size in the AGN rest frame, one would need to multiply observed timescales with an additional factor of Γ_{jet} , for an observer at 90° (in AGN frame) to the moving region.

Another consequence of a relativistically moving emitter is the apparent **superluminal motion** of the transverse velocity component

$$\beta_{obs} \equiv \frac{x_\perp}{\Delta t_{rec}} = \frac{\beta \sin \phi}{1 - \beta \cos \phi} \quad (1.12)$$

⁴This is a somewhat non-standard notation. Here it is used for clarity and in order to avoid a myriad of subscripts and subsubscripts that would ensue from the “ F_ν ”-style notation for differential quantities.

1.4 Models of Jet Radiation

The jet matter content is one of the most debated issues in the high-energy astrophysics, as are the mechanisms that govern their acceleration and energy loss. These two issues are closely related – the composition of the plasma (proton-electron or electron-positron pairs) will determine which energy loss processes will be dominant. The jet content is closely connected to the jet origin, since models expect protons to originate from the accretion disc which powers the jets, while electron-positron pairs are believed to be created by the black hole spin extraction mechanism (Coppi 2002). Therefore, by learning about the nature of the radiation mechanism that operates in jets, one hopes to get an insight into the most central parts of AGN – the inner accretion disc and the SMBH.

Depending on which type of plasma produces the observed radiation – pair plasma (electrons & positrons) or “ordinary” plasma (electrons and protons) – the models that describe the blazar SED are generally divided into leptonic and hadronic. In the leptonic models, pairs synchrotron radiate in the tangled and randomly oriented magnetic field lines that are frozen in the jet material, giving rise to a lower peak, and these photons produced internally to the jet can be upscattered to gamma-ray energies by the same electrons via the Inverse Compton process, thus accounting for the higher SED peak. This is the most widely used model of the blazar SED – Synchrotron Self-Compton (SSC) from a simple, one-zone, spherical emission region. Another possibility for the Compton target photons is the radiation external to the jet (External Compton, EC). The main contributors are believed to be the accretion disc and the BLR, and the torus is sometimes considered (see e.g. Sikora & Madejski 2001 and the references therein). See figure 1.7.

Hadronic models postulate the dominance of the proton-electron plasma, and the gamma-radiation is a sum of several components. The protons can interact with the (soft) photon fields either internal or external to the jet to initiate a cascade of particles (Proton Induced Cascade – PIC – model, e.g. Mannheim 1993) through the pion photoproduction. In this scenario gamma rays can come from the decay of the resulting neutral pions, from the synchrotron radiation of the secondary ultra-relativistic electron-positron pairs (that can originate from the muon decays or from the electromagnetic sub-cascade), and also from the secondary electrons’ Compton-upscattering the photons. In addition to these,

1.4. MODELS OF JET RADIATION

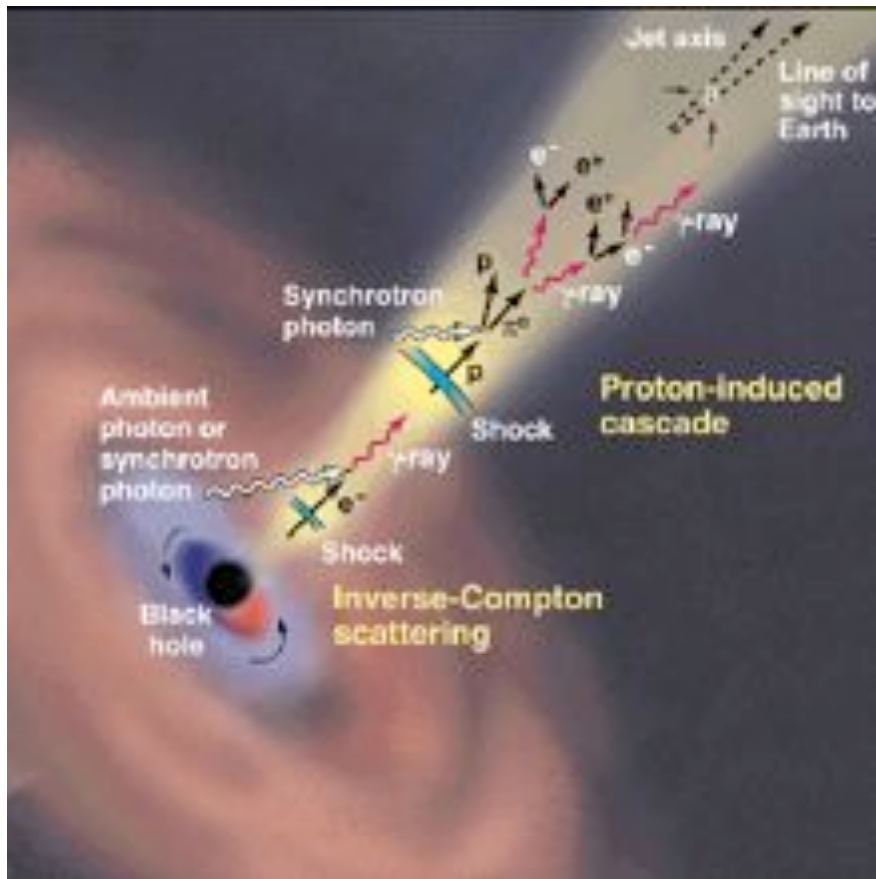


Figure 1.7: Leptonic and hadronic models of the gamma-ray production in relativistic jets are schematically presented (from Buckley 1998). In the leptonic models, seed photons originate either internally or externally to the jet. Hadron collisions initiate the cascade of various particles, which subsequently radiate and give different contributions to the overall double-humped photon spectrum.

there is also the synchrotron radiation of the protons themselves, as the means of the direct production of the gamma-ray photons (Aharonian 2000, 2002). In this model synchrotron radiation comes from the high-energy protons which are co-accelerated with the electrons, that should be responsible for the low-energy component. The picture can be further complicated by introducing the muon synchrotron radiation (e.g. Mücke et al. 2003). A possible test for the nature of the jet plasma is the measurement of the neutrino flux, since it is only expected in the hadronic scenario, as the secondary charged pions produce neutrino signature, through the cascades they initiate⁵.

1.4.1 Difficulties of the Current Models

Major arguments against the hadronic models are the extreme parameters that they require. A proton's radiative efficiency for synchrotron radiation is much lower than electron's due to its high mass (about 2000 times that of an electron), causing the proton to be on one hand easily accelerated to very high energies, but also making the synchrotron cooling ineffective. Also, the rate of pion-production is a few orders of magnitude lower than that of the electron Inverse Compton process (due to the difference in the cross-sections for these processes), which argues for the much slower times for the gamma-ray fluxes to die out in the hadronic case (Buckley 1998). This makes the very rapid variability of BL Lacs harder to explain. Short timescales are also a problem because they put a tighter constraint on the size of the emission region of the high-energy protons. To satisfy this, one needs much higher particle densities and very high magnetic fields (see Coppi 2002), tens of Gauss rather than a milliGauss or centiGauss as required by electrons (which seem to be in agreement with the constraints imposed by the observations). Perhaps the greatest difficulty with the hadronic models is that most of them do not directly predict the good correlation of the two peaks that we observe in some blazar SEDs, e.g. Mrk 421 and Mrk 501, have shown in the past correlations of the X-ray and TeV fluxes (Fossati et al. 2004 see figure 1.9).

In the past, simple, homogeneous one- and two-zone pure SSC models have been largely successful in reproducing the observed time-averaged data, and ex-

⁵Nearly all of the time charged pions decay into muons and muon neutrinos, which subsequently decay into electrons/positrons (depending on the pion charge) and the corresponding electron and muon neutrinos; very seldom (about 0.01% of the time) they decay directly into an electrons/positrons and corresponding electron neutrinos.

1.4. MODELS OF JET RADIATION

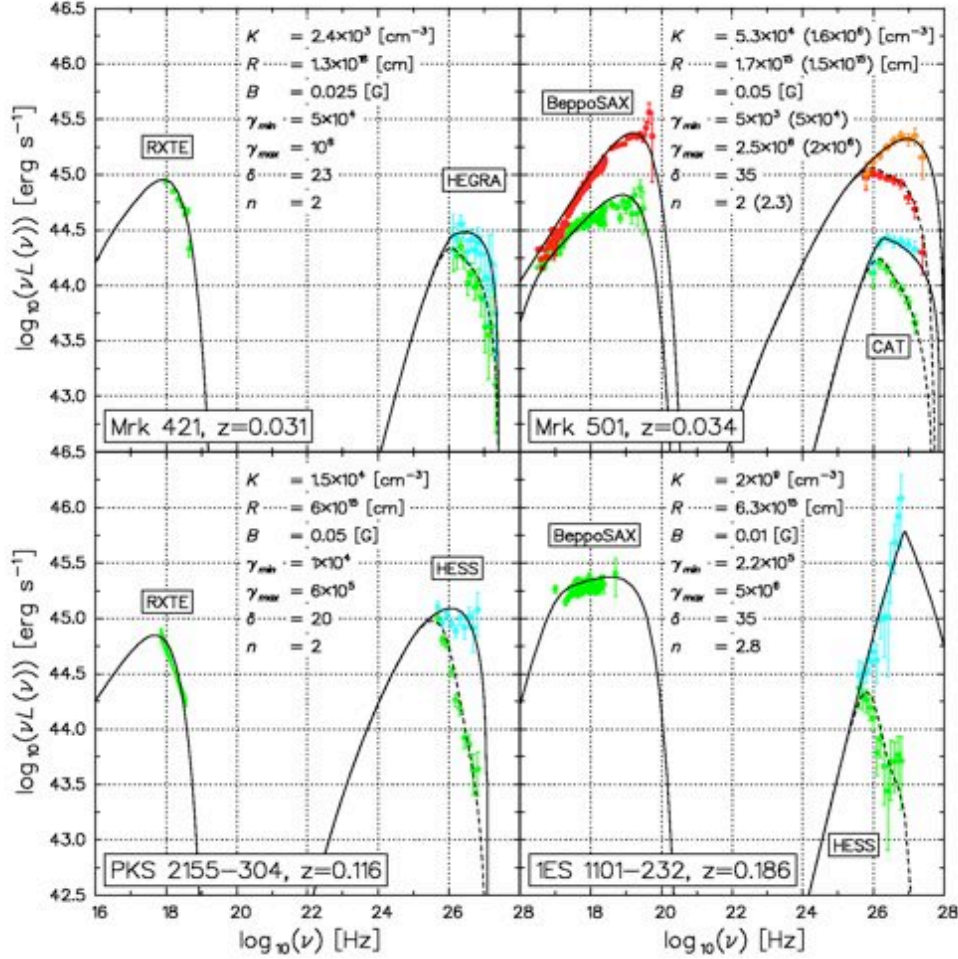


Figure 1.8: Photon spectra of Mrk 421, Mrk 501, PKS 2155 and 1ES 1101 by Katarzynski et al. (2006) modelled with the pure SSC scenario. Dashed lines represent the predictions of the observed spectra, superimposed with the data points from observations, while solid lines are the intrinsic spectra before the absorption takes place, with superimposed unabsorbed data that is corrected for the EBL effects. K is related to the total number density n_e through $K = n_e \frac{1-p}{\gamma_{\max}^{1-p} - \gamma_{\min}^{1-p}}$. The spectrum for 1ES 1101 shows a peculiar shape, influenced by the choice of the extremely narrow and steep electron spectrum. These distant objects are difficult to fit due to a large uncertainty that stems from the extragalactic absorption.

plaining the flux correlation of the two peaks in the BL Lac SEDs (see e.g. Krawczynski et al. 2002; Petry et al. 2000 for Mrk 501, Mastichiadis & Kirk 1997 for Mrk 421). Katarzynski et al. (2006) get excellent agreement with observations using a time-constant, one-zone, homogeneous SSC model (1.8). However, these simple models are not as successful in reproducing the time-resolved spectra. In particular, the observed isolated TeV flares, without any X-ray counterpart – “orphan” flare of 1ES 1959 (Krawczynski et al. 2004; see figure 1.9) and in Mrk 421 (several flares, Blazejowski et al. 2005) – challenge simple SSC models that have no obvious way of reproducing it, and may possibly require a two component emission region, subregions, feedback mechanisms, and hadronic models offer no explanation. Another possible challenge for these models comes from their prediction of the magnetic field values, that seem to be orders of magnitude below the equipartition with the particle energy density. There may also be a problem with the predicted Doppler factor values being extremely high (around 50) after correcting for the high-energy IR absorption (see Tavecchio 2005 for a review).

One of the greatest difficulties that most of the models face is having too many free parameters. The constraints from the flux measurements and light curves are often not very strong, and the degeneracy in the parameters is therefore often present, leaving most of the models without definite statements about the physics of the source. For example, fitting phenomenological power-laws to observed photon SEDs at the high end of X-ray and TeV (frequencies in between are unobservable) does not provide any information about the parameters and structure of the ambient photon fields in AGN, or the emission region, or pin down the acceleration mechanism. For that, particular scenarios should be tested, and it is necessary to specify certain assumptions about the source and test them in a consistent manner.

Another problem is modelling a long train of data, sometimes months- and years-worth, with a unique emission region, and hence as a single flare. This is almost certainly not the case – rather, it is due to a superposition of many individual flares. The only real physics can be extracted from the well defined flares, with fluxes significantly above the detector’s threshold energy to produce the spectrum, sampled closely and resolved down to timescales of minutes (sampling should hopefully become less of a problem now that three major gamma-ray telescope arrays are coming online). This way time-dependent calculations can be performed and averaged over minutes to hours, which should hopefully reproduce

1.4. MODELS OF JET RADIATION

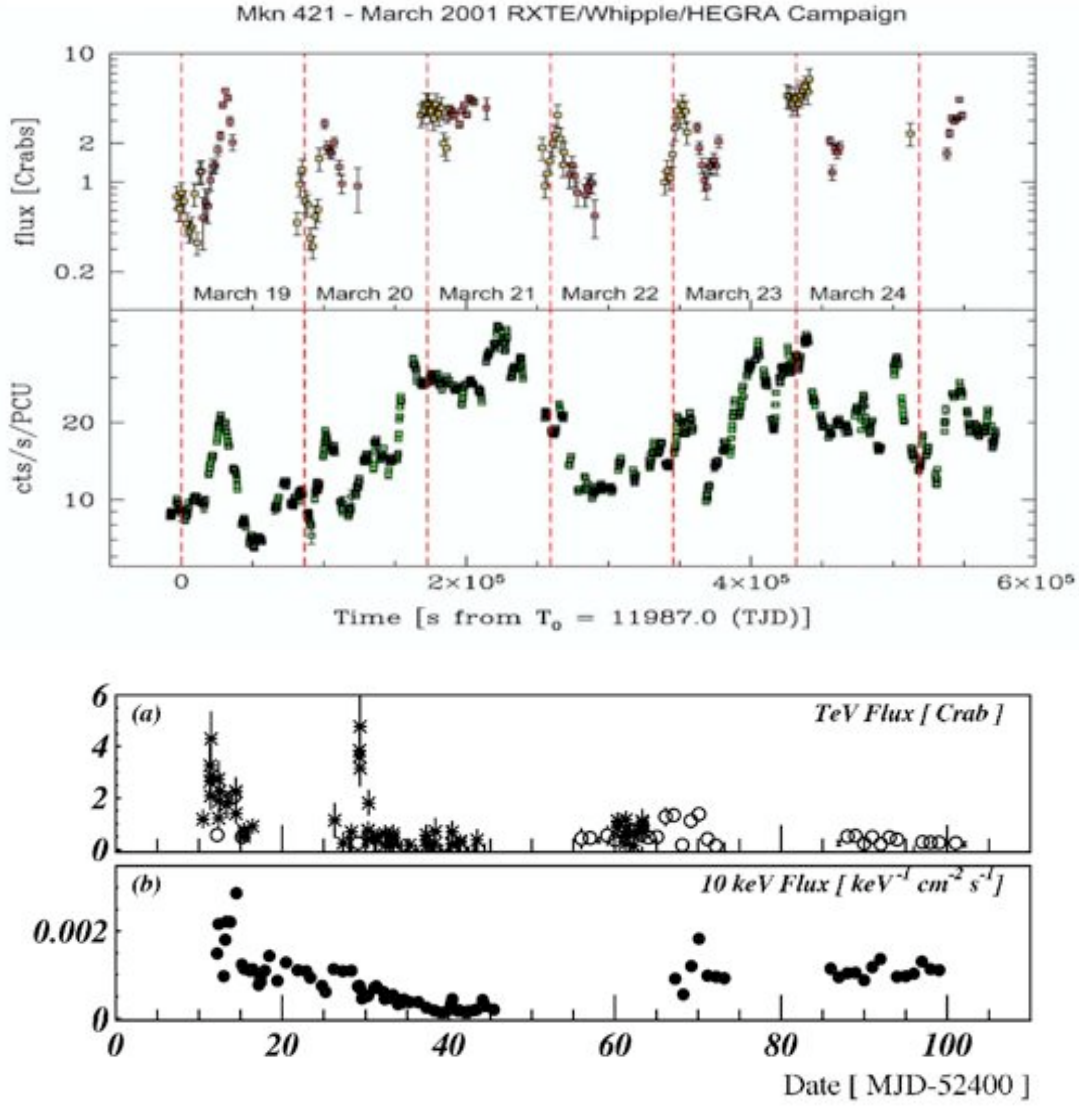


Figure 1.9: Upper panel: an example of good X-ray – TeV correlation typically observed in TeV sources for the source Mrk 421 (Fossati et al. 2004), and an observation of 1ES 1959 TeV “orphan” flare which shows no X-ray counterpart (Krawczynski et al. 2004).

well the evolution of the flare. This is why having a detailed, self-consistent, time-dependent model is crucial in analysing the spectral behaviour. To date, there are very few models that are concerned with the time-evolution of the particle distribution (Böttcher et al. 1997; Krawczynski et al. 2002; Katarzynski et al. 2001).

It is sometimes said that the relative importance of the SSC and the EC component in the jet SED could be assessed by measuring the time lag between the low- and high-energy component in the flares (Coppi & Aharonian 1999). SSC predicts a time lag associated with the light crossing time (R_b/c , R_b being the radius of the blob and c the speed of light), since the IC component is only emitted once the synchrotron photons radiated by the accelerated/injected electrons have had time to propagate through the blob. So far, there has been no confirmation of this behaviour, at least not with high confidence (Krawczynski 2004), although there has been some indication of lags which were much too long to be explained with the SSC scenario (Blazejowski et al. 2005). On the other hand there may be other reasons why one component would be lagging the other, such as the effect of ambient photon fields which is explored later in this thesis. With VERITAS and HESS flares can be resolved down to timescales of hours to as short as a few minutes for strong flares (Weekes et al. 2002; Hinton 2004), therefore making it possible to check for this behaviour in near future (see figure 1.10). Detailed studies of the northern source Mrk 421, the closest of all TeV blazars, should prove invaluable in spectral studies of jets. Remarkable flares from Mrk 501 and PKS 2155 have already been observed by HESS and MAGIC, respectively, in the past few years (Aharonian et al. 2007; Albert et al. 2007).

1.4.2 External Compton Models

A possible resolution for all of these difficulties may come from an introduction of an additional radiation field (or fields) that is external to the jet. EC models have been a necessity in many of the EGRET blazars (Hartman et al. 1999) that could not by any account be described by the SSC models. Their spectra displayed high gamma ray fluxes, relative to the synchrotron peak, which indicates strong Compton cooling, and hence probably high external fluxes. However, these objects are FSRQs, a class of blazars whose SED shows strong emission lines, among which are broad emission lines, and hence provides direct evidence for

1.4. MODELS OF JET RADIATION

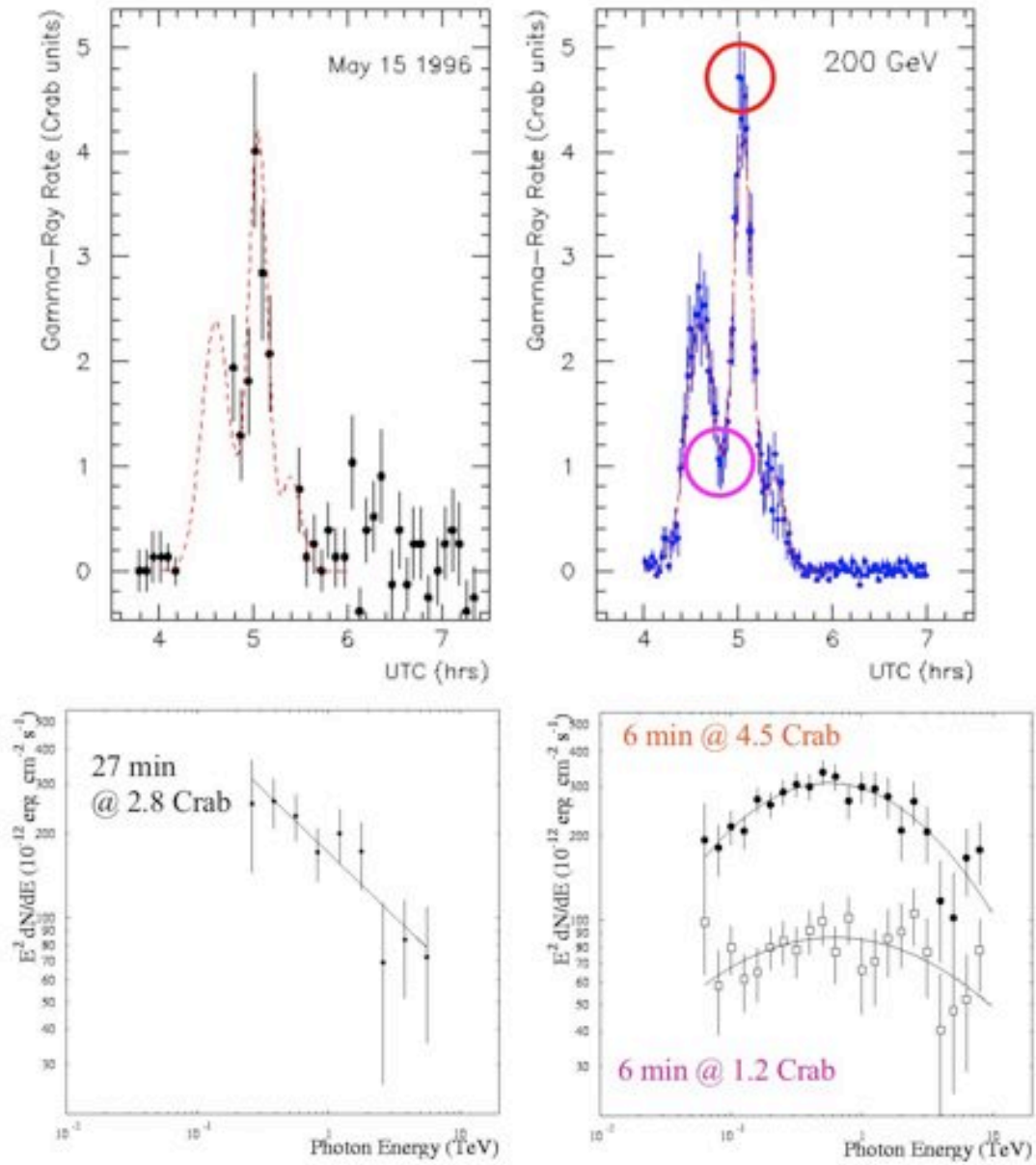


Figure 1.10: An illustration of what is expected from VERITAS. It shows an observation of the rapid flare from Mrk 421 (upper left), observed by Whipple on May 15, 1996 (Gaidos et al. 1996) during which the flux doubled in a matter of an hour. Superimposed on it is a hypothetical flux variation which matches the VHE data (dashed). To the right of it is the simulation of what VERITAS would record for such an event above 200 GeV (for both lightcurves see Weekes et al. 2002). The lower panel shows the corresponding spectra with the notes on the expected flux in terms of the Crab flux for various observation intervals (Frank Krennrich, private communication).

the existence of the BLR and the strong accretion discs (from the UV bump), as well as the IR dust radiation from the torus. However, in high-peaked BL Lacs, the observed SED does not show strong emission lines and this is very often interpreted as the external photon fields in these objects not being important, leaving the SSC to dominate the Compton losses of the jet electrons.

There is, however, evidence for the low-luminosity BLR in at least some BL Lacs. Observations of BL Lacertae have measured the weak broad H_α line corresponding to the luminosity of about $10^{41} \text{ erg s}^{-1}$ (Corbett et al. 2000), and in Mrk 421 and Mrk 501 the BLR luminosities have been inferred to be $1.5 \cdot 10^{40} \text{ erg s}^{-1}$ and $4 \cdot 10^{41} \text{ erg s}^{-1}$, respectively (see review by Donea & Protheroe 2003). The typical values for the BLRs of BL Lac objects are in the range $10^{41} - 10^{43} \text{ erg s}^{-1}$ (Dai et al. 2007). Even if these objects do have intrinsically weak BLRs, these photon fields appear boosted to very high energies in the frame of the relativistic jet and could dominate the IC processes.

In the view of the unification theory, it is often suggested that BL Lacs and FR I represent the same physical class of objects viewed from different angles. In addition, it has also been suggested that a FR I – FR II dichotomy might be critically influenced by the opening angle of the torus, with FR-I having tori that with a large opening angle that would hide to a certain extent the internal regions (including the BLR) from the observer (Falcke et al. 1995). FR I sources Hydra A and Centaurus A, for example, show signatures of IR obscuration. The same argument can be applied to explain the underluminous BL Lacs' accretion discs, that can also contribute to the EC component either directly or after being scattered/reprocessed by the BLR (Dermer & Schlickeiser 1993; Sikora et al. 1997).

The EC models may be very useful in mapping the location where the jet flares occur, since they are sensitive to the distance and nature of the target field in question (BLR clouds, accretion disc, torus dust), so they directly tell us about the physics and structure of the source. The complications, however, arise from the fact that it is most likely that SSC component overlaps with EC, which itself may be a superposition of components from various target field.

1.5 This work

This thesis presents a comprehensive, self-consistent, time-dependent model of spectral evolution of the blazar jet radiation, that is still computationally fast enough to be used as a fit to the future time-resolved observed spectra. It aims to reproduce the observational features of blazars, such as fast rise times of flares, slower fall-off times of synchrotron component w.r.t. those of the gamma-ray peak, orphan TeV flares. It is also of interest to model time-lags of the two components, since in future multiwavelength observations could be able to check for this kind of behaviour.

The variability in blazars is commonly believed to be caused by emitting blobs of high-density plasma that travel with relativistic speeds outwards along the sub-pc jet perpendicularly to the accretion disc. The *internal shocks* scenario is currently the favoured one to explain the acceleration of high particles that produce the observed TeV emission (Ghisellini 2001). It assumes that the central engine discontinuously ejects material of different masses and Lorentz factors into the jet. When two shocks/plasma blobs that are travelling down the jet with different speeds catch up with each other, they form a shock. The resulting shocks' bulk kinetic energy is transferred to the particles, accelerating them to high energies. The shock is also responsible for the creation of tangled magnetic fields of high strength. The equipartition assumption is usually made, so that the equal fractions of shock's bulk motion energy are put into the particles and the magnetic field. The efficiency of this energy transfer will depend on the gamma factors of the colliding shocks. High values of the magnetic field confine the accelerating region and provide quick acceleration timescales, which are reflected in the short rise-times of the observed flux.

As mentioned previously, the injection/shock formation phase is characterised by the acceleration time scale, which can cause quick observed flare rise times, while the fall-off phase marks the start of the shock dissipation/particle escape to the region downstream of the jet, where they cool down radiatively. It is often assumed that the electron maximum energy is caused by the competition of the acceleration gains and the radiative losses. It should be noted, however, that the magnetic field strengths, inferred from the synchrotron peak positions in the available spectra, appear to be many orders of magnitude lower than those predicted for the shock acceleration region (i.e. energy density of the radiating

particles is many orders of magnitude higher than the magnetic energy density). Given that the magnetic field is usually assumed to decay quickly across the shock, this might point to the quick acceleration phase (in which particles have not time to cool radiatively) followed by a longer cooling phase in the region with a lower magnetic field.

The accelerated particles from the emission region interact through various processes with the ambient radiation as well as the self-generated synchrotron photons (in the presence of the ambient magnetic field). If a shock forms during the emitting region's (blob's) passage through the BLR, the clouds' emitted photons can provide the targets for the same population of electrons to Inverse Compton upscatter.

If the external component dominates over the SSC one, the IC peak in the observed SED should quickly diminish after the blob recedes from the BLR region, and possibly just show some sign of the remaining weak SSC activity (Skelton 2001; see also Sikora et al. 1994), along with the synchrotron peak. This would provide a viable explanation for the observed difference in the flare timescales between the extremely rapidly variable high-energy component and the low-energy component which can continue to flare for months and years.

The EC model also offers a possible explanation for the orphan TeV flares (Krawczynski et al. 2004). Time-variable profiles of the external fields (Wehrle 1997), for example due to the emission region's passage through the BLR (whose parameters change with the distance from the centre), could generate TeV fluxes without a detectable synchrotron counterpart if the magnetic field is weak enough (other causes may include: intrinsic variability in the disc; the precession in the jet that would cause a great change in the gamma-ray flux with only a slight change in the synchrotron flux due to the narrower beaming angle of the TeV component; the magnetic field alignment along jet axis, since the view along the B-field axis would provide no observable synchrotron flux whilst gamma-rays still being detectable. See Krawczynski et al. 2004 for discussion). In the case of the external scenarios, one should observe the IC emission to vary linearly with the synchrotron component for any change in the electron population (Sikora et al. 1994).

The model described in this thesis reproduces the TeV spectra with the little explored EC model that also includes an SSC component. The external target field of primary interest is the Broad Line Region photons but the accretion disc

1.5. *THIS WORK*

photons are included as well. By assuming a particular structure of the BLR (derived from the observations of BLRs, Kaspi & Netzer 1999) and the disc, as well as the peculiarities of their radiation whilst evolving the particle population in a self-consistent manner, it is possible to learn more about the physical processes and the geometry of the AGN.

Chapter 2

Radiative Processes

This chapter discusses in detail the elementary processes that influence the electron energy distribution as well as the emitted photon spectrum of the blazar jet emission region. The essential derivations are also outlined to provide a more rounded overview of the problem.

Interactions that lead to Gamma-ray production

In astrophysics, the two scenarios that are normally invoked to explain the origin of TeV gamma-ray emission involve Inverse Compton scattering and neutral pion decay. In principle, other processes such as Bremsstrahlung (the radiation from a charged particle in the Coulomb field of another charged particle) and synchrotron radiation (radiation from a charged particle in the magnetic field) can also lead to gamma-ray production. These two processes, however, are not normally considered. Bremsstrahlung is of minor importance in pair plasmas as lepton's deceleration is much weaker in the presence of another lepton than in the presence of a much more massive (inert) proton, where it leads to a much greater momentum transfer. Also for electron synchrotron radiation to produce gamma-rays enormous magnetic fields and particle energies would be required, many orders of magnitude above the highest values that one might expect from AGN. On the other hand synchrotron radiation is sometimes invoked in hadronic scenarios as the direct way of producing gamma-rays (see Section 1.4 for an overview and discussion of the importance and difficulties of hadronic processes). However, Inverse Compton scattering (Jones 1968; Blumenthal & Gould 1970) remains the most probable and natural way of TeV gamma-ray production in

2.1. INVERSE COMPTON SCATTERING

astrophysical environments. For an evaluation and a discussion on the relative importance of various radiative processes in pair plasmas see Coppi & Blandford (1990); Coppi (1992).

2.1 Inverse Compton Scattering

Inverse Compton scattering is essentially the same process as the Compton scattering but viewed from a different reference frame. While the Compton process describes a photon scattering off an electron (or indeed any charged particle) at rest, Inverse Compton represents the scattering off a moving electron. The interaction of ultrarelativistic charges and low-energy photons typically results in a high energy gain for the photons, boosting them as high as gamma-ray range¹.

The scattering cross-section is influenced by the photon energy relative to that of the electron. Based on the ratio of the two, one can clearly distinguish between the regime that can be well approximated by Thomson scattering, and that where the interaction has to be treated with a full Klein-Nishina cross-section.

The requirement for the scattering to be in the Thomson regime is that the energy of the incoming photon ($\epsilon = E_{ph}/mc^2$, in units of electron rest mass), as well as the scattered photon energy, is much less than that of the electron energy ($\gamma = E_e/mc^2$). In such a case, the change in photon energy in the electron rest frame (ERF) is considered negligible – the photon simply bounces off the electron, changing only its own direction (see e.g. Rybicki & Lightman 1979). In the lab frame, this typically increases the photon energy by γ^2 (one factor of γ is picked up from boosting into the ERF and another one after the scattering, from boosting back into the lab frame). The condition of the approximation can be written as

$$\gamma^2 \epsilon \ll \gamma \quad (2.1)$$

The total scattering cross-section is then simply the Thomson cross-section

$$\sigma_T = \frac{8\pi}{3} r_0^2 \quad (2.2)$$

where

$$r_0 = \frac{1}{4\pi\epsilon_0} \frac{e^2}{m_e c^2} \quad (2.3)$$

¹Theoretically, an electron can actually gain energy, but this is an extremely unlikely case of an overtaking collision that happens when electron and photon directions are exactly the same.

2.1. INVERSE COMPTON SCATTERING

is the classical electron radius. All the equations in this thesis will be given in SI (although some quantities may be quoted in other systems, like CGS).

In the regime where the photon's ERF energy is comparable to or greater than the electron rest energy, the electron energy losses become considerable and the classical approximation no longer holds. In such case the outcome of the scattering will be crucially influenced by the incoming photon's energy and direction. The basic relativistic kinematic equations for the scattering conserve the 4-momenta of the photon plus electron. The probability of particular final states are governed by the Klein-Nishina cross-section for IC scattering (see Blumenthal & Gould 1970 for details).

For a correct treatment of the Compton scattering of high energy photons one has to use the full Klein-Nishina cross section (σ) in order to derive the emitted photon spectrum. The scattering rate is obtained by summing over the initial electron and photon distributions (see e.g. Jones 1968; Weaver 1976)

$$\dot{n}_{ph}(d\epsilon_s, d\Omega_s) = c \int_{\gamma} \int_{\Omega_e} n_e(d\gamma, d\Omega_e) \left[\int_{\epsilon} \int_{\Omega_{ph}} n_{ph}(d\epsilon, d\Omega_{ph}) \frac{d\sigma}{d\epsilon_s d\Omega_s} (1 - \beta \mu_{ph,e}) d\epsilon d\Omega_{ph} \right] d\gamma d\Omega_e \quad (2.4)$$

where $n_e(d\gamma, d\Omega_e)$ and $n_{ph}(d\epsilon, d\Omega_{ph})$ are the electron and the incoming photon number densities differential in the dimensionless energy and the solid angle, given in $[\text{m}^{-3} \text{sr}^{-1}]$ and $\mu_{ph,e}$ the cosine of the angle between the directions of the incoming photon and electron (see end of Chapter 1.3.3 for the explanation on the notation used). The differential cross section $\frac{d\sigma}{d\epsilon_s d\Omega_s}$ (that is also a function of electron and photon energies and directions) gives the probability of a photon of initial energy ϵ_i and incoming angle (φ_{ph}, μ_{ph}) interacting with an electron $(\gamma, \varphi_e, \mu_e)$ and producing an outgoing photon $(\epsilon_s, \varphi_s, \mu_s)$, where μ denotes the cosine of the polar angle of the particle and φ the azimuthal angle (where the polar axis coincides with the jet axis). The term inside the square brackets is essentially the differential scattering rate for a single electron, where $\mu_{ph,e}$ represents the cosine of the angle between the electron and the incoming photon. The above expression, when integrated over the observing time, directly gives the photon spectrum at a particular viewing angle.

The emission region is usually modelled as a sphere of isotropically distributed electrons. In this case, it is useful to have an analytical expression for the scat-

2.1. INVERSE COMPTON SCATTERING

tering rate that is already integrated over the electron directions, of the form

$$\dot{n}_{ph}(d\epsilon_s, d\Omega_s) = \int_{\gamma} n_e(d\gamma) \int_{\Omega_{ph}} \int_{\epsilon} n_{ph}(d\epsilon, d\Omega_{ph}) \frac{dC}{d\epsilon_s d\Omega_s} d\epsilon d\Omega_{ph} d\gamma \quad (2.5)$$

where

$$\frac{dC}{d\epsilon_s d\Omega_s} = c \int_{\Omega_e} \frac{d\sigma}{d\epsilon_s d\Omega_s} (1 - \beta \mu_{ph,e}) d\Omega_e \quad (2.6)$$

represents a differential probability per unit time (with $C(\epsilon, \mu_{ph}, \gamma)$ and $\sigma(\epsilon, \mu_{ph}, \gamma, \mu_e)$).

A detailed analytical treatment of such a case was presented in Reimer et al. (2006). Calculating the rates and spectra this way is very advantageous from a numerical point of view, since it removes one dimension of integration, resulting in a much faster and more reliable calculation. The scattering rate in the blob frame is then

$$\begin{aligned} \dot{n}_{ph}(d\epsilon_s, d\Omega_s) = & \frac{3}{16\pi} \sigma_T c \epsilon_s \int_{\gamma} \int_{\epsilon} \int_{\varphi} \int_{\mu} n_e(d\gamma) n_{ph}(d\epsilon, d\Omega_{ph}) \Theta(\epsilon_s - \epsilon_{s1}) \quad (2.7) \\ & \times \frac{1}{\beta \gamma^2 \epsilon \sqrt{\epsilon_s^2 - 2\mu_{ph,s} \epsilon \epsilon_s + \epsilon^2}} \\ & \times \left[1 - \frac{1}{(2\epsilon_s \gamma \beta)^2} \left(\frac{\mu_+ + \mu_- + 2b}{((\mu_+ + b)(\mu_- + b))^{\frac{3}{2}}} + \frac{\mu_+ + \mu_- + 2a}{((\mu_+ + a)(\mu_- + a))^{\frac{3}{2}}} \right) \right. \\ & \left. - \left(\frac{\epsilon(1 - \mu_{ph,s})}{2\gamma\beta} - \frac{\epsilon\epsilon_s(1 - \mu_{ph,s}) + 1}{\gamma\beta\epsilon_s^2(1 - \mu_{ph,s})} \right) \right. \\ & \left. \times \left(\frac{1}{((\mu_+ + b)(\mu_- + b))^{\frac{1}{2}}} + \frac{1}{((\mu_+ + a)(\mu_- + a))^{\frac{1}{2}}} \right) \right] d\varphi d\mu d\epsilon d\gamma \end{aligned}$$

where $\mu_{ph,s}$ is the cosine of the photon scattering angle

$$\mu_{ph,s} = \mu_{ph} \mu_s + \sqrt{1 - \mu_{ph}^2} \sqrt{1 - \mu_s^2} \cos(\varphi_{ph} - \varphi_s) \quad (2.8)$$

The coordinate system is defined so that the polar axis coincides with that of the jet. The other quantities used in this formula are defined below

$$a = -\frac{1}{\beta} \quad (2.9)$$

2.1. INVERSE COMPTON SCATTERING

$$b = -\frac{1}{\beta} - \frac{\epsilon(1 - \mu_{ph,s})}{\beta\gamma} \quad (2.10)$$

$$\mu_{\pm} = \frac{AB \pm C_1 \sqrt{B^2 + C_1^2 - A^2}}{B^2 + C_1^2} \quad (2.11)$$

where μ_{\pm} are the limits on the cosine of the incoming electron angle, and

$$A = \epsilon_s \left(1 + \frac{\epsilon(1 - \mu_{ph,s})}{\gamma} \right) - \epsilon \quad (2.12)$$

$$B = \beta(\epsilon_s - \epsilon\mu_{ph,s}) \quad (2.13)$$

$$C_1 = \beta\epsilon\sqrt{1 - \mu_{ph,s}^2} \quad (2.14)$$

The argument of the Heaviside step function $\Theta(\epsilon_s - \epsilon_{s1})$ controls the maximum possible energy of the scattered photon ϵ_s for given set of parameters

$$\epsilon_s \leq \epsilon_{s1} = \frac{\gamma^2 \epsilon (1 + \beta)(1 - \beta\mu_{ph,s})}{1 + \gamma\epsilon(1 + \beta)(1 - \beta\mu_{ph,s})} \quad (2.15)$$

If ϵ_s is larger than the maximum value, the argument of the Heaviside step function is negative, hence the step function returns 0. However, this condition can be rewritten to obtain the minimum value for initial photon energy ϵ when the final energy of the photon ϵ_s is fixed. This puts a constraint on the lower energy integration limit in the equation 2.7

$$\epsilon \geq \frac{\epsilon_s}{(\gamma - \epsilon_s)\gamma(1 + \beta)(1 - \beta\mu_{ph,s})} \quad (2.16)$$

The scattering rate expression given in equation 2.5 can be rewritten to obtain the losses at each energy in the particle spectrum by integrating over the final photon's energies and directions instead

$$\dot{n}_e(d\gamma) = n_e(d\gamma) \int_{\Omega_s} \int_{\epsilon_s} \int_{\Omega_{ph}} \int_{\epsilon} n_{ph}(d\epsilon, d\Omega_{ph}) \frac{dC}{d\epsilon_s d\Omega_s} d\epsilon d\Omega_{ph} d\epsilon_s d\Omega_s \quad (2.17)$$

(c.f. equation 2.7 for $n_{ph}(d\epsilon, d\Omega_{ph})$). Similarly, the gains in number density at each energy, due to electrons migrating down from higher energies, are

$$\dot{n}_e(d\gamma_s) = \int_{\Omega_s} \int_{\epsilon_s} \dot{n}_{ph}(d\epsilon_s, d\Omega_s; \gamma) \delta(\gamma_s - (\gamma - \epsilon_s)) d\epsilon_s d\Omega_s \quad (2.18)$$

2.1. INVERSE COMPTON SCATTERING

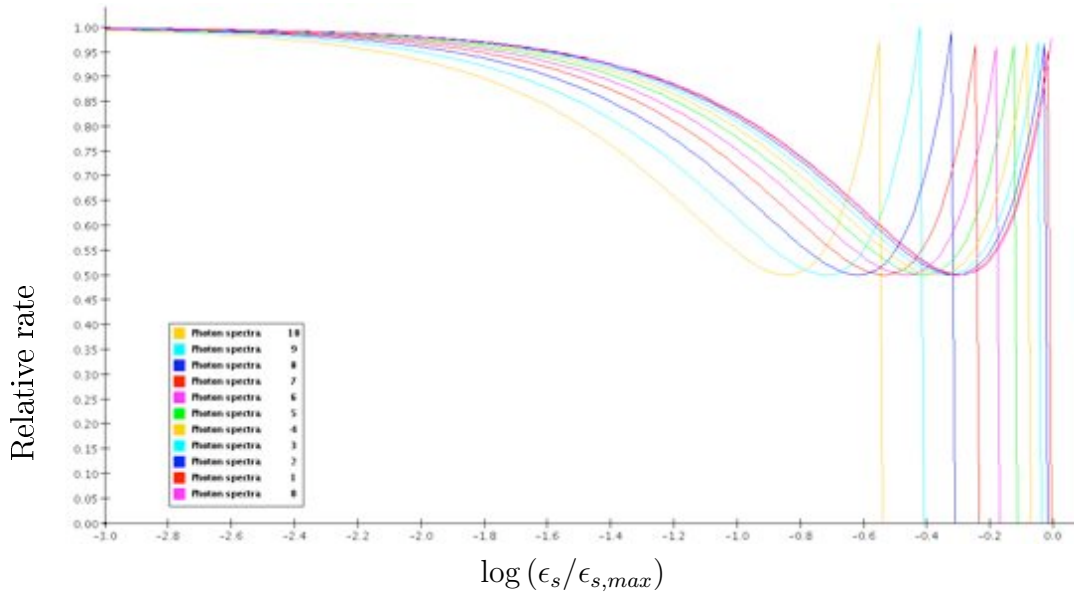


Figure 2.1: Relative rate (per unit ϵ_s) for a parallel beam of target photons $\epsilon = 10^{-7}$ scattering with the monoenergetic electrons of energy $\gamma = 10^5$. Spectra are plotted for several different scattering angles (hence, in this case, different angles between the source's velocity and the observer), starting from π rad (in steps of 0.2 rad). For $\theta_s \simeq 0$ we see mostly photons that suffered head-on collision and thus have highest possible energy $\epsilon_{s,max}$ (for isotropic scattering, number of such photons would be negligible). The peaks should all be at the same height (at 1) and their misalignment in this plot is an artifact of binning.

2.1. INVERSE COMPTON SCATTERING

γ_s being the scattered electron's Lorentz factor. Here the δ -function fixes the final photon energy, given the initial and final energy of the electron. The initial energy of the photon is typically so small, that it is negligible in comparison to γ , γ_s and ϵ_s (so that $\gamma_s \simeq \gamma - \epsilon_s$). One can then write the gain rate at energy γ_s

$$\dot{n}_e(d\gamma_s) = \int_{\Omega_s} \int_{\epsilon_s} \int_{\gamma} n_e(d\gamma) \int_{\Omega_{ph}} \int_{\epsilon} n_{ph}(d\epsilon, d\Omega_{ph}) \frac{dC}{d\epsilon_s d\Omega_s} \delta(\gamma_s - (\gamma - \epsilon_s)) d\epsilon d\Omega_{ph} d\gamma d\epsilon_s d\Omega_s \quad (2.19)$$

The above integrals need to be calculated numerically. To perform this efficiently, the integration limits need to be tightly constrained:

- Electron energy γ for the photon outgoing spectrum (equation 2.5) runs through $[\epsilon_s, \gamma_{max}]$ (as the initial electron energy has to be at least that of the outgoing photon); for the calculation of the gain (equation 2.19) this variable runs through $[\gamma_s, \gamma_{max}]$.
- Scattered photon solid angle Ω_s runs over the full solid angle.
- Scattered photon energy ϵ_s runs through $[0, \gamma_{max}]$.
- Initial photon angle Ω limits depend on the geometry of the target field.
- Initial photon energy ϵ limits depend on the target field, but will not necessarily run over the full range of target energies – there is also a constraint from the condition given in the equation 2.16.

The limits on incoming photons' energies ϵ and angles Ω shall be discussed individually for each field. It should also be noted that it is assumed that there is an azimuthal symmetry in the targets fields, about the jet axis, and so the differing limits on the angles really only concern the polar angle θ . The azimuthal angle limits go over the full range $[0, 2\pi]$.

One should note that evaluating these calculations in practice is not a straightforward affair. Numerical problems arise from the fact that $\frac{\mu_+ - \mu_-}{\mu_+}$ can become extremely small, due to a subtraction of two very similar numbers (μ_+ and μ_-), which causes large uncertainties in the calculation (equation 2.7). In such a case an approximation needs to be used (see Appendix B).

2.2. SYNCHROTRON SPECTRUM

Isotropic target photons. For isotropically distributed target photons, such as the electrons' own synchrotron photons, the calculations of the spectra are highly simplified due to the absence of any angular dependence. In such a case one can use the angle integrated probability per unit time

$$\frac{dC(\epsilon, \gamma)}{d\epsilon_s} = \frac{3}{4} \sigma_T c \frac{1}{\gamma^2 \epsilon} \left(1 + q - 2q^2 + 2q \ln q + \frac{(Gq)^2(1-q)}{2(1+Gq)} \right) \quad (2.20)$$

(see Jones 1968; Blumenthal & Gould 1970), with

$$q = \frac{\epsilon_s}{4\gamma\epsilon(\gamma - \epsilon_s)} \quad (2.21)$$

$$G = 4\gamma\epsilon \quad (2.22)$$

The ranges for ϵ_s and q are

$$\epsilon_s \in \left(\epsilon, \frac{4\gamma^2\epsilon}{1+4\gamma\epsilon} \right) \quad (2.23)$$

$$q \in \left(\frac{1}{4\gamma(\gamma - \epsilon)}, 1 \right) \quad (2.24)$$

2.2 Synchrotron Spectrum

Synchrotron radiation is generated by a charged particle that is spiralling down the magnetic field lines, which causes it to be accelerated and emit photons of radio to X-ray energies.

The spectral power (power per unit frequency) radiated by an electron of dimensionless energy γ in plasma is given by (Rybicki & Lightman 1979; Blumenthal & Gould 1970)

$$P(d\nu; \gamma) = \frac{\sqrt{3}}{4\pi\epsilon_0} \frac{e^3 B_\perp}{m_e c} \left(1 + \left(\frac{\gamma\nu_p}{\nu} \right)^2 \right) F \left(\frac{\nu}{\nu'_c} \right) \quad (2.25)$$

in $[\text{W Hz}^{-1} = \text{J}]$, where $B_\perp = B \sin \theta_B$ is the component of the magnetic field perpendicular to the electron velocity vector, with a pitch angle θ_B , and a critical

frequency (near which the emission peaks) in plasma

$$\nu'_c(\gamma) \approx \nu_c(\gamma) \left(1 + \left(\frac{\gamma \nu_p}{\nu} \right)^2 \right)^{-\frac{3}{2}} \quad (2.26)$$

with $\nu_c(\gamma) = \frac{3}{4\pi} \frac{eB_\perp}{m_e} \gamma^2$ being the critical frequency in vacuum and

$$F\left(\frac{\nu}{\nu'_c}\right) = \frac{\nu}{\nu'_c} \int_{\frac{\nu}{\nu'_c}}^{\infty} K_{5/3}(\xi) d\xi \quad (2.27)$$

is the synchrotron photon distribution function, which peaks at $\nu \simeq 0.3\nu_c$. Here $K_{5/3}$ is a modified Bessel function. Note that in this section the subscript “sy” for “synchrotron” will be omitted from the equations for the sake of clarity (but will be used later on to mark the distinction from other processes).

However, in a randomly oriented magnetic field, one can average the power over all pitch angles. The treatment that incorporates the angle averaging as well as the effects of radiation in a plasma were outlined by several authors (see e.g. Böttcher et al. 1997; Böttcher & Chiang 2002; Crusius & Schlickeiser 1988)

$$P(d\nu; \gamma) = \frac{\alpha \pi h \nu}{\sqrt{3} \gamma^2} \left(1 + \left(\frac{\gamma \nu_p}{\nu} \right)^2 \right) CS(x) \quad (2.28)$$

where α is the fine structure constant, and

$$CS(x) = W_{0, \frac{4}{3}}(x) W_{0, \frac{1}{3}}(x) - W_{\frac{1}{2}, \frac{5}{6}}(x) W_{-\frac{1}{2}, \frac{5}{6}}(x) \quad (2.29)$$

(see Crusius & Schlickeiser 1988) where W are the Whittaker functions and

$$x = \frac{2}{3\gamma^2} \frac{\nu}{\nu_e} \left(1 + \left(\frac{\gamma \nu_p}{\nu} \right)^2 \right)^{\frac{3}{2}} \quad (2.30)$$

where $\nu_e = eB/(2\pi m_e)$ is the nonrelativistic electron gyrofrequency and the relativistic plasma frequency (the natural frequency of nonpropagating electrostatic oscillations of a charged species, in this case electrons) is

$$\nu_p = \frac{1}{2\pi} \sqrt{\frac{n_e e^2}{\varepsilon_0 m_e \langle \gamma \rangle}} \quad (2.31)$$

where n_e is the total electron number density (as opposed to the differential

2.2. SYNCHROTRON SPECTRUM

number density $n_e(d\gamma)$). Note that for pair plasmas this standard frequency needs to be modified to correct for the fact that instead of heavy ions one has positrons, so both negatively and positively charged particles move with respect to their centre of mass, so the total plasma frequency for pairs is $\nu_{p,tot} \equiv \sqrt{\nu_{p,+}^2 + \nu_{p,-}^2} = \nu_p\sqrt{2}$ (see e.g. Verheest 2006). This slightly modified frequency should not affect the spectrum in any detectable way.

The emission coefficient for the synchrotron radiation [$\text{J Hz}^{-1} \text{s}^{-1} \text{m}^{-3} \text{sr}^{-1}$] is obtained by summing through the power contributions from the electron throughout the spectrum ($n(d\gamma)$)

$$j(d\nu) = \int_1^\infty \frac{P(d\nu; \gamma)}{4\pi} n_e(d\gamma) d\gamma \quad (2.32)$$

Isotropic electrons of energy γ will then have an average synchrotron cooling rate of

$$\dot{\gamma}_{sy} = -\frac{4}{3}\sigma_T c \frac{U_B}{m_e c^2} \gamma^2 \quad (2.33)$$

with the magnetic energy density U_B dependent on the magnetic field strength

$$U_B = \frac{B^2}{2\mu_0} \quad (2.34)$$

where μ_0 is the magnetic permeability of free space. For a power-law distribution of electrons of the slope p , the resulting synchrotron spectrum will have a slope of $\frac{p-1}{2}$, over the range of frequencies above the self-absorption frequency. An example of a synchrotron spectrum from a power-law distribution of electron is given in figure 2.2.

2.2.1 Synchrotron Self-Absorption

Electrons can become opaque to their own radiation and start absorbing the synchrotron photons. The transition from the optically thick to optically thin part of the synchrotron spectrum is marked by the point where the electron kinetic temperature is to exceed that of a black body of intensity I_ν , which is not permitted.

The self-absorption frequency marks the division between the two regions,

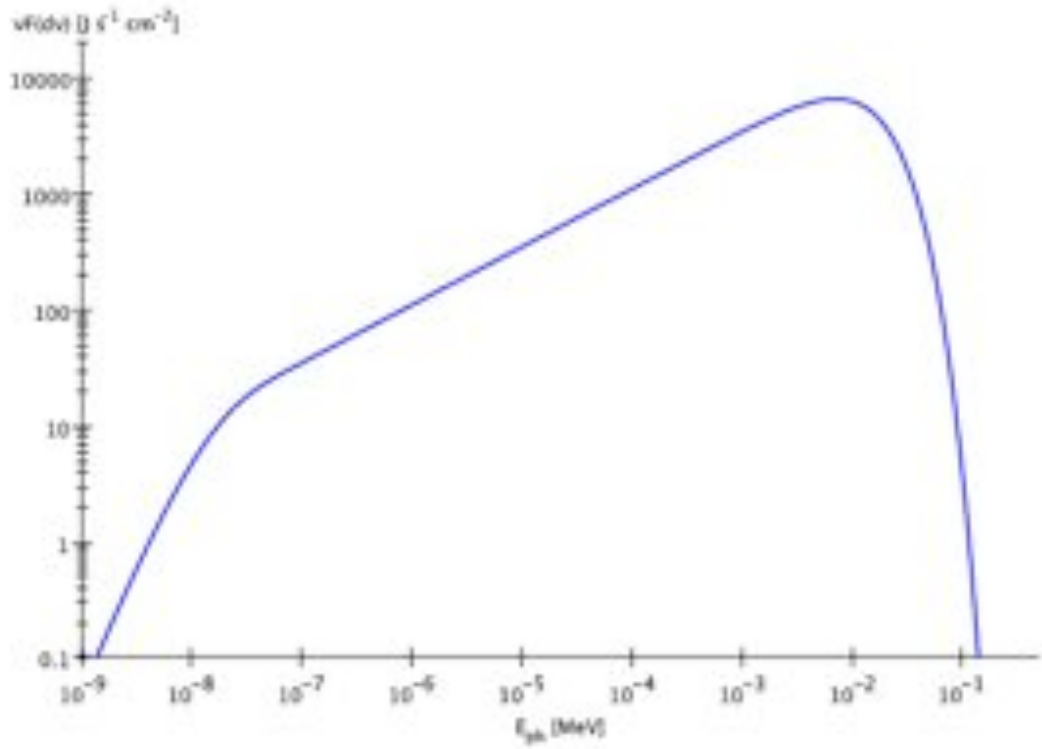


Figure 2.2: Synchrotron spectrum (in $\nu F(d\nu)$ representation) due to an ensemble of electrons with a power-law distribution $p = 2$ (with the synchrotron self-absorption accounted for).

2.2. SYNCHROTRON SPECTRUM

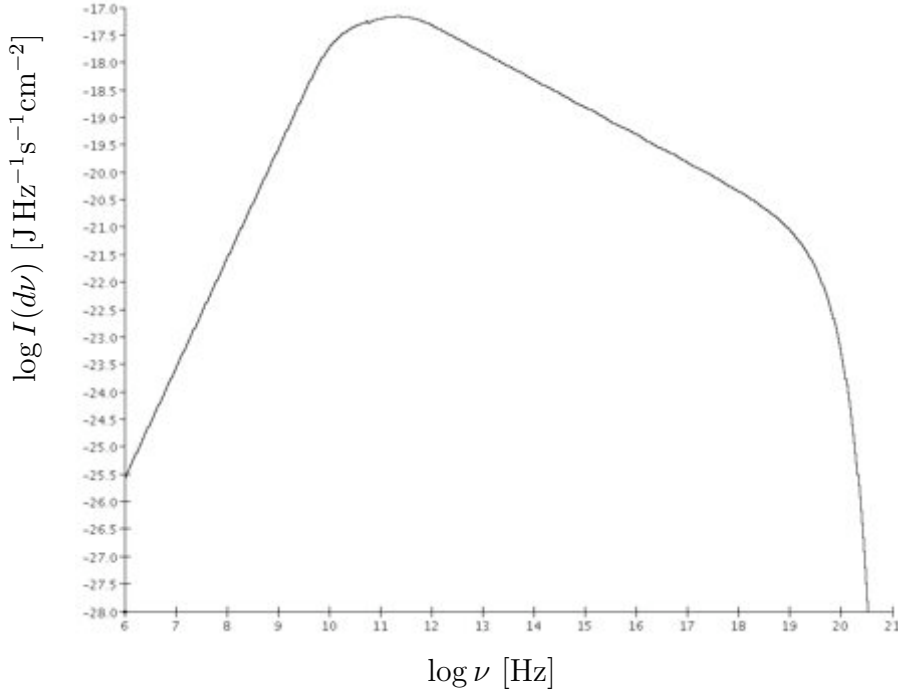


Figure 2.3: Synchrotron self-absorption causes the slope of the intensity spectrum to be around 2.5 below the self-absorption frequency. Here the plot shows the synchrotron radiation from a power law distribution of electrons, between the Lorentz factors of 10^2 and 10^6 .

below which the self-absorption optical depth is greater than one. Below this frequency, the (absorbed) synchrotron spectrum is independent of the electron spectrum and typically has a slope around 2.5. The absorption coefficient [m^{-1}] can be calculated as

$$\alpha(\nu) = \frac{1}{8\pi m_e \nu^2} \int_1^\infty P(d\nu; \gamma) \gamma^2 \frac{d}{d\gamma} \left(\frac{n_e(d\gamma)}{\gamma^2} \right) d\gamma \quad (2.35)$$

The synchrotron intensity (see figure 2.3) for the case of the spherical region with a uniform emission coefficient (Bloom & Marscher 1996; Kataoka et al. 1999) can be calculated by solving the transfer equation, and gives

$$I(d\nu_{sy}) = \frac{j(d\nu_{sy})}{\alpha(\nu_{sy})} \left(1 - \frac{2}{\tau^2(\nu_{sy})} (1 - e^{-\tau(\nu_{sy})} (\tau(\nu_{sy}) + 1)) \right) \quad (2.36)$$

in [$\text{J Hz}^{-1} \text{s}^{-1} \text{m}^{-2} \text{sr}^{-1}$], with $\tau(\nu_{sy}) = 2R_b \alpha(\nu_{sy})$ being the optical depth for the sphere of radius R_b .

2.2.2 Razin-Tsytoich Effect

Razin-Tsytoich effect describes the suppression of the synchrotron emission at low frequencies due to the effect of the plasma. It occurs when the medium has a negative refractive index (n), i.e. when the phase velocity of the light in the plasma is greater than that in vacuum (c). This widens the angle (θ) into which emission is beamed and hence suppresses the beaming as $\theta \sim 1/\gamma = \sqrt{1 - (n\beta)^2}$. The medium will be important when $\nu \ll \gamma\nu_p$ since $n = \sqrt{1 - (\nu_p/\nu)^2}$ and there will be a suppression of synchrotron radiation at frequencies less than the Razin-Tsytoich frequency ν_R

$$\nu_R \equiv \frac{2\nu_p^2}{3\nu_e} \frac{1}{\sin\theta_B} = \frac{1}{3\pi} \frac{e}{\varepsilon_0} \frac{n_e}{\langle\gamma\rangle B \sin\theta_B} = 1.9 \cdot 10^4 \frac{n_{e4}}{\langle\gamma_3\rangle B_{-2} \sin\theta_B} \text{Hz} \quad (2.37)$$

$\langle\gamma_3\rangle = \langle\gamma\rangle/10^3$ being the average electron Lorentz factor in units of 10^3 , $n_{e4} = n_e/10^4 \text{cm}^{-3}$ and $B_{-2} = B/10 \text{mG}$. This effect puts an exponential cut-off on the synchrotron spectrum at ν_R (Simon 1969). The Razin Lorentz factor for electrons is

$$\gamma_R \equiv \frac{2\nu_p}{3\nu_e} \frac{1}{\sin\theta_B} = \frac{2}{3} \sqrt{\frac{m_e}{\varepsilon_0}} \frac{n_e^{0.5}}{\langle\gamma\rangle^{0.5} B \sin\theta_B} = 0.6 \frac{n_{e4}^{0.5}}{\langle\gamma_3\rangle^{0.5} B_{-2} \sin\theta_B} \quad (2.38)$$

Only electrons of higher energies that γ_R contribute significantly to the synchrotron emission. For electron number densities around 10^8cm^{-3} (and typical values of $B = 10 \text{mG}$, $p = 2$) SSA and Razin-Tsytoich frequencies are of the same order. For higher number densities Razin-Tsytoich effect will dominate SSA (Crusius & Schlickeiser 1988) and the lower cut-off in the synchrotron spectrum is would be due to Razin-Tsytoich effect and not the SSA.

2.3 Pair Production

Electron-positron pair production can occur through the annihilation of two photons of favourable relative energies. This effect is important in blazars for two reasons. Firstly, because the gamma rays produced in the emission region can annihilate with the ambient photons, which are either self-produced synchrotron

2.3. PAIR PRODUCTION

radiation (neglected here) in the emission region or with the fields external to the jet, and therefore get absorbed before they are able to escape to infinity. This is especially important when the emission region is very close to the central engine – inside a particular radius (gamma-ray energy dependent) no jet-produced gamma-rays would be able to escape the blob. This radius marks what is called a gamma-ray photosphere (Blandford & Levinson 1995). The second important application is the absorption of TeV photons by the extragalactic background radiation.

The optical depth for this process at a particular distance z along the jet can be calculated as a function of the energy ϵ_γ of gamma-ray photons, which are all assumed to be strongly beamed along the jet axis, by integrating the (differential) soft photon spectrum $n_{ph}(d\epsilon, d\mu; z)$ from the external fields (Jauch & Rohrlich 1980)

$$\tau_{\gamma\gamma}(\epsilon_\gamma, z_i) = \int_{z_i}^{\infty} dz \int_{-1}^{+1} d\mu \int_{\frac{2}{\epsilon_\gamma(1-\mu)}}^{\infty} d\epsilon (1-\mu) \sigma_{\gamma\gamma}(\epsilon_\gamma, \epsilon, \mu) n_{ph}(d\epsilon, d\mu; z) \quad (2.39)$$

where μ is the cosine of the polar angle of the incoming soft photons (ϵ), and $\sigma_{\gamma\gamma}(\epsilon_\gamma, \epsilon, \mu)$ is the cross section for the unpolarised and isotropic high-energy photons and is given by

$$\sigma_{\gamma\gamma}(\beta) = \frac{3}{16} \sigma_T (1 - \beta^2) \left((3 - \beta^4) \ln \left(\frac{1 + \beta}{1 - \beta} \right) - 2\beta (2 - \beta^2) \right) \quad (2.40)$$

Here

$$\beta = \sqrt{1 - \frac{2}{\epsilon_\gamma \epsilon (1 - \mu)}} \quad (2.41)$$

is the velocity (in units of speed of light) of the produced electron and positron in their centre of mass frame. Note that the whole of the calculation is carried out in the frame of the host galaxy when soft targets are local ambient photons. For the optical depth calculation due to EBL the integral is somewhat different (see Kneiske et al. 2004).

It can be seen that the threshold for the pair production is given as $\epsilon_\gamma \epsilon \geq \frac{2}{(1-\mu)}$. For $\beta = 0$ and $\mu = -1$ the cross-section peaks, at $\frac{\sigma_T}{5}$, giving the threshold energy

around $\epsilon_\gamma \sim \frac{1}{\epsilon}$. Assuming the spectrum of photons is steep enough (i.e. spectral index is < -1), the opacity is dominated by soft photons just above the threshold energy. Optical depth for a photon ϵ_γ can be approximated as (Costamante 2001)

$$\tau(\epsilon_\gamma) = \frac{1}{5} \frac{\sigma_T}{4\pi m_e c^3} \frac{L_{soft}(\frac{1}{\epsilon_\gamma})}{R} \quad (2.42)$$

For values of $\tau \gtrsim 1$ the emitting region is opaque to photons with energies higher than the electron rest energy.

The compactness parameter l is a convenient way to check the relevance of this and other processes on the escaping luminosity. It is defined as the soft photon energy in units of electron mass, intercepted per Thomson cross-section in a photon crossing time (Frank et al. 1992, p. 231)

$$l \equiv \frac{L_{soft}}{m_e c^2} \frac{\sigma_T}{4\pi R^2} \frac{R}{c} = 2.16 \cdot 10^{-25} \frac{L_{soft}}{R} \text{J}^{-1} \text{s m} = 2.16 \frac{L_{soft44}}{R_{14}} \quad (2.43)$$

or in other words, it expresses the ratio between the produced luminosity L_{soft} and the size of the emitting region R , as a dimensionless quantity (here $L_{soft44} = L_{soft}/10^{44} \text{erg s}^{-1}$ and $R_{14} = R/10^{14} \text{cm}$). An alternative way of defining it is to omit the factor of 4π from the denominator, which is how it is usually defined (Fabian et al. 1986). Using the latter definition, the internal compactness of a region is derived from the synchrotron luminosity L_{soft} and is related to the optical depth (equation 2.42) as

$$\tau(\epsilon_{sy}) \simeq \frac{l(\frac{1}{\epsilon_{sy}})}{60} \quad (2.44)$$

In other words, the region becomes opaque for $l \gtrsim 60$.

Radius of the gamma-ray sphere, $z_\gamma(\epsilon_\gamma)$, is defined by

$$\int_{\ln z_\gamma}^{\infty} d \ln \tau_{\gamma\gamma}(\epsilon_\gamma, z) = d \ln r \tau_{\gamma\gamma}(\epsilon_\gamma, z) = 1 \quad (2.45)$$

This can be inverted to get the escape energy at a given radius $z_\gamma(\epsilon_{\gamma,esc}(r))$. Then only gamma-rays with $\epsilon_\gamma < \epsilon_{\gamma,esc}$ can escape.

Figure 2.4 shows the comparison of optical depths due to different photon fields (see next chapter), at various distances along the jet (c.f. figure 4.9, optical depth due to EBL). The disc seems to be insignificant for gamma-ray pair pro-

2.3. PAIR PRODUCTION

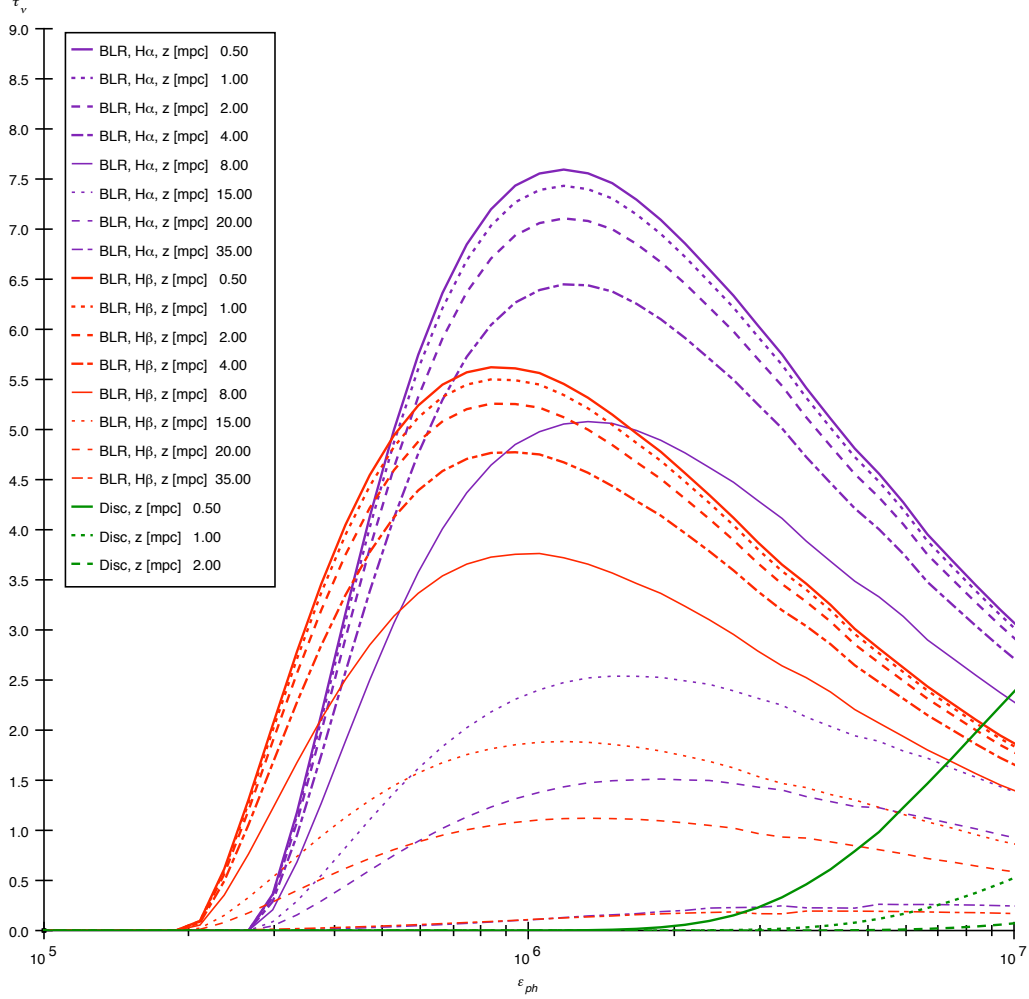


Figure 2.4: Optical depth due to the accretion disc photons and the BLR photons (photon energy is given in units of mc^2). For the latter, both a monoenergetic case of BLR radiating at $H\alpha$ and in $H\beta$ are presented. It can be seen that the optical depth due to BLR photons decreases with the distance from the central engine, but this slows down near the outer edge of the BLR (40 mpc) and the optical depth profiles converge. Below about 100 GeV the optical depth goes quickly to zero. The disc curves display a profile similar to that of the BLR curves, but peaking at much higher gamma-ray energies. For the disc photons below about 10 TeV the optical depth quickly drops to zero.

duction, due to the small $(1 - \mu)$ term in the optical depth calculation, since the disc photons and the gamma rays travel nearly in the same direction. The optical depth plot demonstrates this – the disc only starts being significant at several TeV, and only for the closest distances of the blob w.r.t. to the disc (0.5 mpc); it goes to zero already at 2 mpc. On the other hand, gamma-rays encounter low-energy photons from all directions due to the BLR radiation while the blob is inside of it (there is also an isotropic background, EBL). The BLR can absorb a significant amount of the produced gamma radiation before the emission region emerges out of it. For very small distances of the blob to the centre, the BLR becomes opaque at gamma-ray energies as low as a couple of hundred GeV. This point slowly shifts towards the higher energies as the blob passes through the BLR, which finally becomes transparent to the blob radiation as it approaches the BLR's outer edge.

Chapter 3

Target Fields

In the leptonic scenario, electrons are responsible for the primary synchrotron radiation, which produces the low-energy peak in the observed SED. In the case of SSC, the seed photons for the subsequent IC scattering process are internal to the jet – they are simply the synchrotron-produced photons. In the EC scenario, the situation is much more complicated, because the photons originate externally to the jet. The complication arises from the fact that there are several different target fields in the AGN that can react with the emission region electrons – they could contain components from the BLR clouds, accretion disc, the reprocessed radiation from the dust in the torus (disc radiation absorbed then re-radiated at longer wavelengths), or it could be the synchrotron photons from the jet reflected (hence reprocessed again) from the disc or BLR clouds (see e.g. Sikora et al. 1994; Böttcher 2005). Here we shall concentrate on what are widely considered to be the three most important target fields – synchrotron, accretion disc and Broad Line Region photons.

3.1 Synchrotron Photons

The number density of emitted synchrotron photons in a homogeneous spherical region of isotropically moving electrons is (Katarzynski et al. 2001)

$$n_{ph}(d\epsilon) = \frac{3}{4} 4\pi \frac{1}{\epsilon h c} \frac{j(d\nu)}{\alpha(\nu)} (1 - e^{-\alpha(\nu)R_b}) \quad (3.1)$$

where $\epsilon = \nu \frac{h}{m_e c^2}$ (see end of Chapter 1.3.3 for the explanation on the notation used). The correction term of 3/4 is used to account for the fact that the syn-

chrotron density is not uniform but decreases along the radius, away from the centre of the blob. This equation is valid once photons have had time to travel through the blob, so after one crossing time. Thus the emitted distribution is also isotropic, so the scattering rate integral is then

$$\dot{n}_{ph}(d\epsilon_s, d\Omega_s) = \frac{1}{4\pi} \int_{\gamma} n_e(d\gamma) \int_{\epsilon} n_{ph}(d\epsilon) \frac{dC(\epsilon, \gamma)}{d\epsilon_s} d\epsilon d\gamma \quad (3.2)$$

where $n_{ph}(d\epsilon)$ is the synchrotron photon number density from the equation 3.1, and $\frac{dC(\epsilon, \gamma)}{d\epsilon_s}$ is calculated according to equation 2.20.

An typical SSC spectrum from power-law electrons is given in figure 3.1.

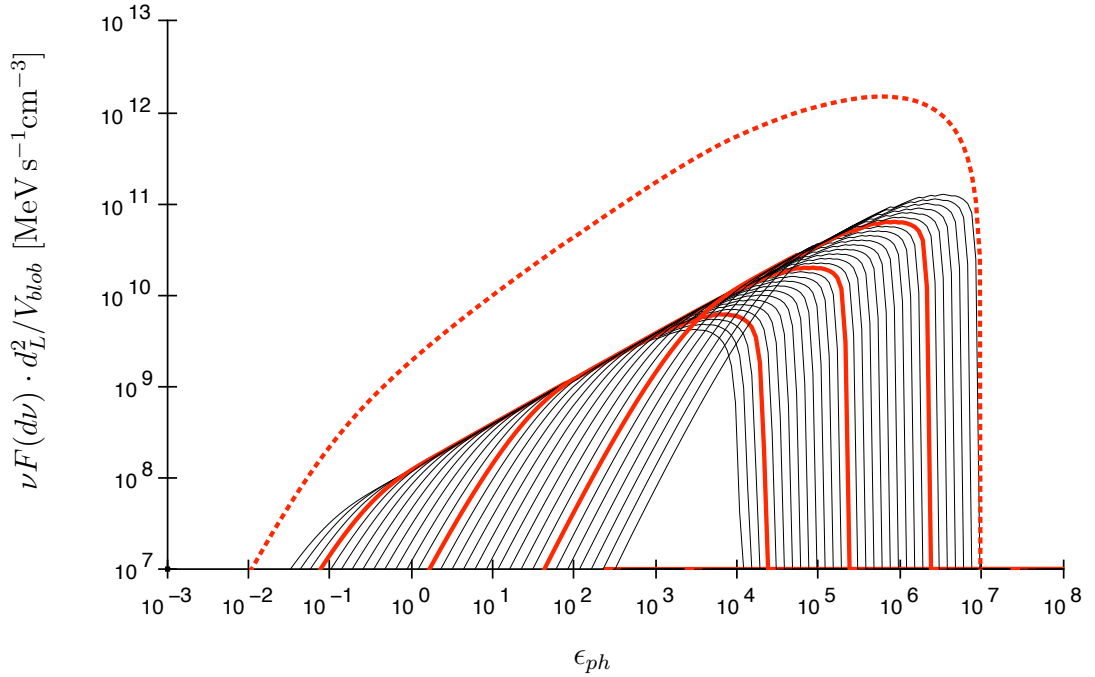


Figure 3.1: Upscattered synchrotron radiation by a power-law distributed population of electrons ($p = 2$), given in the observer's frame (dotted red line). Each black line is a spectrum from monoenergetic electrons. The red lines correspond to the spectra generated by electrons separated by a decade in energy.

The photon spectrum ($F(d\nu)$) emitted from a power law electron spectrum with a slope p is also a power law in a log-log representation with a slope of $-\frac{p-1}{2}$. This portion of the spectrum is in the Thomson regime. In the $\nu F(d\nu)$ representation this section of the spectrum corresponds to energies lower than

3.2. ACCRETION DISC PHOTONS

the energy of the spectral peak, with a slope $\frac{3-p}{2}$ (as evident from figure 3.1). At energies higher than the peak energy, slope is $1 - p$, as this marks the Klein-Nishina regime, where the cross section falls off with the scattered energy (see e.g. Skelton 1999).

3.2 Accretion Disc Photons

The treatment of the accretion disc's geometry and radiation adopted in this thesis is based on the model first proposed by Shakura & Sunyaev (1973). Dermer & Schlickeiser (1993) and Böttcher et al. (1997) also use it to describe the target field photon density for the External Compton upscattering in a blob propagating along the jet axis.

Their model is appropriate for a SMBH of masses found in AGN and it treats the disc as a series of concentric rings, each one radiating as a blackbody with a temperature which falls off with increasing radius R .

The polar angle is defined through the radius R of the ring and the blob distance z_b along the jet as $\cos \theta = \frac{z_b}{\sqrt{R^2 + z_b^2}}$. The radiated intensity (the emitted power per unit area of emitting surface, per unit solid angle, and per unit frequency) at a radius R at an angle θ from a normal is represented with a Planck distribution

$$B(d\nu; \Theta(R)) \equiv \frac{2h}{c^2} \frac{\nu^3}{e^{h\nu/k_B T(R)} - 1} \cos \theta = \frac{2h}{c^2} \left(\frac{m_e c^2}{h} \right)^3 \frac{\epsilon^3}{e^{\epsilon/\Theta(R)} - 1} \cos \theta \quad (3.3)$$

where the normalised temperature distribution $\Theta(R)$ is given by¹

$$\Theta(R) \equiv \frac{k_b T(R)}{m_e c^2} = 1.44 \left(\frac{M}{M_\odot} \right)^{-\frac{1}{2}} \left(\frac{\dot{M}}{M_\odot / \text{yr}} \right)^{\frac{1}{4}} \left(\frac{R}{R_g} \right)^{-\frac{3}{4}} \left(1 - \sqrt{6 \frac{R_g}{R}} \right)^{\frac{1}{4}} \quad (3.4)$$

where $R_g = GM/c^2$ is the gravitational radius and $\dot{M} = L_{disc}/(\eta_{acc} c^2)$ is the mass accretion rate, where η_{acc} is the efficiency of gravitational energy conversion into radiation. The energy arriving at the blob per unit time per unit frequency at a polar angle θ equals the intensity of the radiation emitted from the ring of the

¹see Böttcher et al. (1997)

corresponding radius R and emitting area dA_e into a solid angle $d\Omega$

$$\frac{dE}{dtd\nu} = B(d\nu; \Theta(R)) dA_e d\Omega \quad (3.5)$$

By dividing this through with a volume element one gets the expression for the number density

$$n(d\epsilon, d\Omega) = \frac{B(d\nu; \Theta(R))}{\epsilon h} dA_e \frac{dt}{dV} \quad (3.6)$$

where $dV = c dt dA$, dA being the observed projection of the emitting area that is reduced as $dA = dA_e \cos \theta$. The final expression for the number density is then²

$$n(d\epsilon, d\Omega) = \frac{B(d\nu; \Theta(R))}{\epsilon h c} \frac{1}{\cos \theta} \quad (3.7)$$

By using the Lorentz invariance of the quantity $n_{ph}(d\epsilon, d\Omega)/\epsilon^2$ this is then boosted into the blob frame as

$$(n_{ph}(d\epsilon, d\Omega))_{blob} = \left(\frac{\epsilon^{blob}}{\epsilon^G} \right)^2 (n_{ph}(d\epsilon, d\Omega))_G \quad (3.8)$$

where “G” stands for the “galaxy frame” and “blob” for the blob frame.

Integration Limits. The disc geometry constrains the integration limits for the photon incoming angle in scattering rate integrals. The problem has the azimuthal symmetry, and the polar angle limits are defined by the polar angles of the inner and outer disc radii. In the galaxy frame the limits for the cosine of the polar angle (μ) are then

$$\mu_{min}^G = \frac{z_b}{\sqrt{R_{disc,out}^2 + z_b^2}} \quad (3.9)$$

$$\mu_{max}^G = \frac{z_b}{\sqrt{R_{disc,in}^2 + z_b^2}} \quad (3.10)$$

where the inner disc radius $R_{disc,in}$ is typically of the order of several gravitational radii R_g (Donea & Protheroe 2003). Each limit then needs to be boosted into the blob frame according to

$$\mu^{blob} = \frac{\mu^G - \beta_{jet}}{1 - \beta_{jet} \mu^G} \quad (3.11)$$

²note that the result by Böttcher et al. (1997) differs from this by a factor of $\frac{1}{4 \cos \theta}$

3.2. ACCRETION DISC PHOTONS

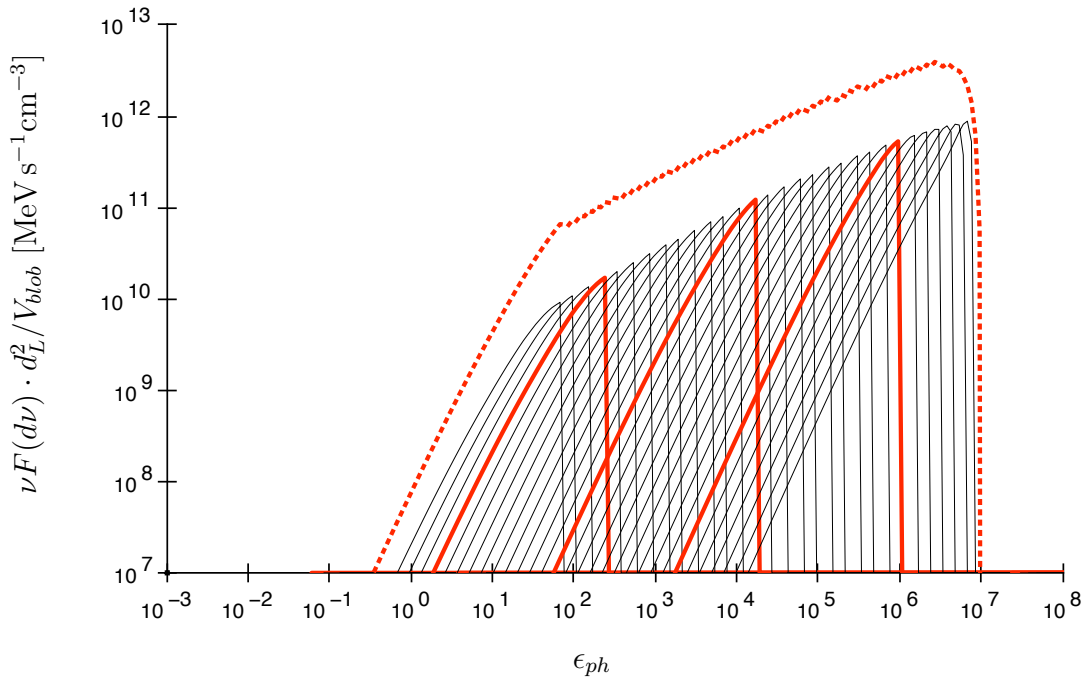


Figure 3.2: The dashed red line represents the upscattered disc radiation by a power-law distributed electrons ($p = 2$), given in the observer's frame. Each black curve is a spectrum from monoenergetic electrons. The solid red lines correspond to the spectra generated by electrons separated by a decade in energy.

The integration over the photon energy ϵ in scattering rate integrals (equations 2.17, 2.19) is in principle only constrained at the lower end by the condition given by the equation 2.16. An example of the upscattered disc spectra is shown in figure 3.2.

3.3 Broad Line Region Photons

Sikora et al. (1994) have proposed the disc radiation reprocessed in the BLR as important target fields in blazars, arguing that the accretion disc radiation may not make a significant contribution at the distances outside the gamma-ray photosphere. The reason is geometrical – the disc is assumed to be geometrically thin and for all practical purposes (in terms of providing important scattering targets) very small, hence its radiation should be redshifted. The BLR and torus, on the other hand, contribute from a wide range of angles.

The BLR is often invoked when considering the target fields for the EC models, since it should exist at the subparsec scale at which the observed TeV radiation originates. The BLR consists of gas clouds moving near the SMBH at speeds of the order of thousands km/s, which are inferred from the broadening of the emission lines. The clouds absorb the radiation in EUV – X-ray region and are consequently heated, so the incident accretion disc radiation is in effect re-radiated in the form of a BLR thermal continuum of about 20,000 K (Skelton 1999). Clouds are believed to be radiating anisotropically, being heated more from the side facing the central region. The luminosity of individual clouds should be a function of their distance from the central region, and there is an indication that the BLR luminosity depends to a certain extent on how powerful the host AGN is.

The Broad Line Region is not spatially resolved in HBLs, but some knowledge of the structure and parameters of these objects is inferred indirectly from reverberation mapping. The sizes of BLRs are known to be of the order of light months in quasars and light weeks in Seyferts (Donea & Protheroe 2003). The extremely weak observed radiation from the BLR in TeV blazars is often interpreted as an intrinsic feature, and the BLR photons as the scattering targets in these objects are therefore often dismissed. However, it can be argued that this goes against the Unified theories, which unify FR I and BL Lacs. As mentioned before, FR I objects can show signs of IR obscuration, which some authors interpret as the

3.3. BROAD LINE REGION PHOTONS

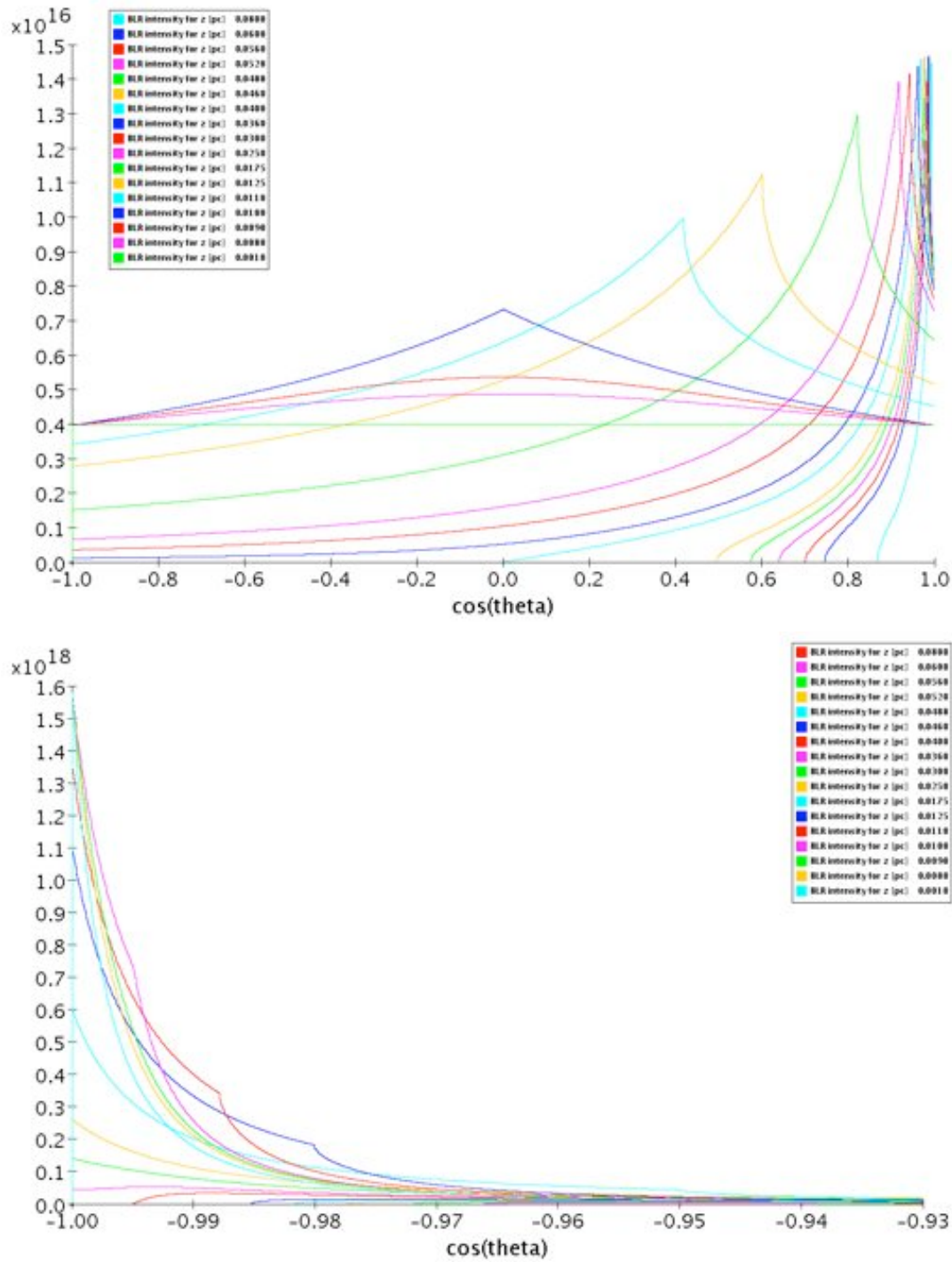


Figure 3.3: Unboosted and boosted incoming number densities of the BLR photons plotted against their incoming angle to the blob. The $\cos \theta_s = -1$ corresponds to the radiation coming head on relative to the emission region velocity (β_{jet}) direction, and $\cos \theta_s = +1$ means the radiation is hitting the blob in the back. Note that the scales on horizontal axes are different. The second plot shows a strongly boosted incoming spectrum for $\Gamma_{jet} = 10$.

3.3. BROAD LINE REGION PHOTONS

existence of a torus with a large opening angle (Falcke et al. 1995) which hides the BLR and prevents the observer from making a correct estimate of the BLR luminosity.

The formation of the BLR clouds is still an open question, however their radiation is closely linked with the accretion disc luminosity. To describe the Broad Line Region, a simplistic approach as outlined in Donea & Protheroe (2003) was adopted. The region is modelled as a spherical shell of gas clouds, that are approximated with spheres of a radius which increases with the distance from the centre. Accretion disc photons ionise the BLR gas, giving rise to a line spectrum ($H\alpha$, $H\beta$, OIII, NII). However, the simplification is made that all the luminosity is contained in the $H\alpha$ line. The BLR clouds are assumed to be optically thin ($\tau_{BLR} \ll 1$). A fraction τ_{BLR} of the total central luminosity [J s^{-1}] will then be reprocessed in the whole of the BLR

$$L_{BLR} = \tau_{BLR} L_{disc} \quad (3.12)$$

A typical blazar has the BLR luminosity of $L_{BLR} \approx 2 \cdot 10^{43} \text{erg s}^{-1}$, but this may be much lower for the BL Lac. For Mrk 421 the luminosity was observed to be $L_{BLR} = 1.5 \cdot 10^{40} \text{erg s}^{-1}$ (Morganti et al. 1992). A fraction $d\tau_{BLR}$ of central engine's luminosity will be reprocessed in a $r \rightarrow r + dr$ shell

$$d\tau_{BLR} = \tau_{cl} n_{cl} \sigma_{cl} dr \quad (3.13)$$

where $\sigma_{cl} = \pi R_{cl}^2$ is the cross-section of a cloud of radius R_{cl} (at a fixed shell at distance r), n_{cl} is the number of clouds per unit volume and τ_{cl} is the optical depth of a cloud. The emission coefficient of reprocessed radiation at the distance r from the centre is

$$j(r) = \frac{dL_{BLR}}{d\Omega dV} \quad (3.14)$$

which, for a spherical, isotropic shell translates into

$$j(r) \equiv \frac{L_{disc} d\tau_{BLR}}{(4\pi) (4\pi r^2 dr)} = \frac{L_{disc}}{16\pi^2 r^2} \frac{d\tau_{BLR}}{dr} \quad (3.15)$$

The BLR model outlined in Kaspi & Netzer (1999) assumes the number den-

3.3. BROAD LINE REGION PHOTONS

sity of clouds in the BLR region falls off with distance r as

$$n_{cl} = n_0 \left(\frac{r}{r_{in}} \right)^\alpha \quad (3.16)$$

The radius of clouds in the BLR region increases with distance r according to

$$R_{cl} = R_0 \left(\frac{r}{r_{in}} \right)^\beta \quad (3.17)$$

In Kaspi & Netzer (1999) the best fits for NGC 5548 were $\alpha = -1.5$ and $\beta = 0.6$. Note that r_{in} and r_{out} denote inner and outer radii of the BLR (for the sake of simplicity, in this section the subscript “BLR” will be omitted).

One can now rewrite the equation 3.13, after substituting for cloud number density and radius, as

$$d\tau_{BLR} = \tau_{cl} n_0 \pi R_0^2 \left(\frac{r}{r_{in}} \right)^{\alpha+2\beta} dr \quad (3.18)$$

The total optical depth is then

$$\tau_{BLR} \equiv \int_{r_{in}}^{r_{out}} \tau_{cl} n_0 \pi R_0^2 \left(\frac{r}{r_{in}} \right)^{\alpha+2\beta} dr = \tau_{cl} n_0 \pi R_0^2 \int_{r_{in}}^{r_{out}} \left(\frac{r}{r_{in}} \right)^{\alpha+2\beta} dr \quad (3.19)$$

By dividing the previous two equations (to conveniently eliminate the constant $\tau_{cl} n_0 \pi R_0^2$) one gets

$$\frac{d\tau_{BLR}}{dr} = \frac{\tau_{BLR}}{\int_{r_{in}}^{r_{out}} \left(\frac{r}{r_{in}} \right)^{\alpha+2\beta} dr} \left(\frac{r}{r_{in}} \right)^{\alpha+2\beta} \quad (3.20)$$

The value of the integral is

$$\int_{r_{in}}^{r_{out}} \left(\frac{r}{r_{in}} \right)^{\alpha+2\beta} dr = \frac{1}{r_{in}^{\alpha+2\beta}} \frac{1}{\alpha+2\beta+1} \left(r_{out}^{\alpha+2\beta+1} - r_{in}^{\alpha+2\beta+1} \right) \quad (3.21)$$

One can now write

$$\frac{d\tau_{BLR}}{dr} = \frac{\tau_{BLR}(\alpha+2\beta+1)}{r_{out}^{\alpha+2\beta+1} - r_{in}^{\alpha+2\beta+1}} r^{\alpha+2\beta} \quad (3.22)$$

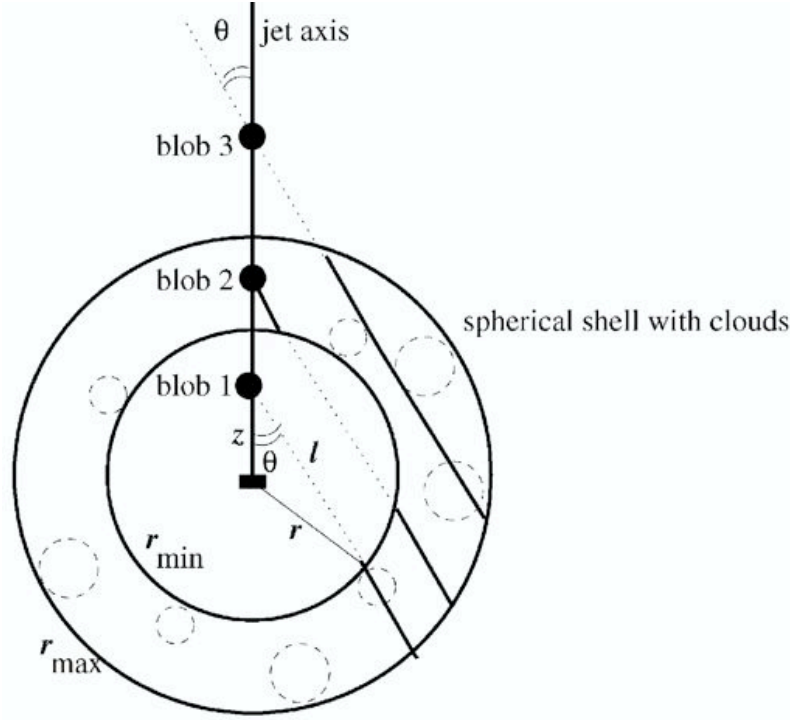


Figure 3.4: The schematic representation of a model of the Broad Line Region. Depending on its position along the jet, the blob will see a different angular distribution of the BLR photons. The drawing is taken from Donea & Protheroe (2003).

After substituting for $d\tau_{BLR}/dr$ in equation 3.15 one arrives at the expression for the emission coefficient as a function of radius

$$j(r) = \frac{L_{disc}}{16\pi} \frac{\tau_{BLR}(\alpha + 2\beta + 1)}{r_{out}^{\alpha+2\beta+1} - r_{in}^{\alpha+2\beta+1}} r^{\alpha+2\beta-2} \quad (3.23)$$

where r is given by $r^2 = z^2 + l^2 - 2zl \cos \theta$ (θ being the polar angle measured with respect to the blob position from the jet axis).

3.3.1 Position of the blob relative to the BLR

The intensity of radiation I arriving at the blob from a particular direction is calculated by integrating the emission coefficient j along the line of sight. Depending on where the blob is relative to the BLR, the integral over emissivity along the line of sight will have different limits. One has to consider three separate cases (illustrated in figure 3.4):

3.3. BROAD LINE REGION PHOTONS

1. Closer than the inner BLR radius (position “blob 1” in figure 3.4): the photons arrive at the blob from all directions. The line of sight integral will run from the interception of the line of sight with the sphere of the radius r_{in} to the interception with the sphere with the radius r_{out} .
2. Inside the BLR (“blob 2”): there will be contributions from all directions. One distinguishes between two cases:
 - (a) If one is looking towards the central cavity, which corresponds to angles θ (w.r.t. the jet axis) lower than that defined by the tangent to the inner radius: one needs to add up the contributions from the points between the blob position (at the distance z_b from the centre) and the first point of interception of the line of sight with the sphere defined by the radius r_{in} , as well as the contributions between the second point of interception and the interception with the sphere defined by the outer radius r_{out} .
 - (b) Anywhere else: single integral from the blob position to the interception with the outer sphere.
3. Outside the BLR (“blob 2”), further than r_{out} : the contributions are seen only from the lines of sight with angles to jet axis lower than that defined by the tangent to the outer radius. One distinguishes between three cases:
 - (a) If one is looking towards the central cavity: contributions come from between the first point of intercept with the outer sphere and the first interception with the inner sphere and also from between the second interception with the inner sphere and the second interception with the outer sphere.
 - (b) At angles θ that lie between the angles defined by the tangents to the inner and outer radius: single integral between the first and the second interception with the outer sphere.
 - (c) Anywhere else (θ greater than the angle defined by the tangent to the outer radius): integral is zero.

For the case when the blob is within the BLR and looking towards the central cavity, the intensity of radiation along the line of sight l at the angle θ from the jet axis at the distance z from the central point is

$$I(z, \theta) = \int_0^{l_{min1}} j(r) dl + \int_{l_{min2}}^{l_{max}} j(r) dl \quad (3.24)$$

where

$$l_{min1,2} = z_b \cos \theta \mp z_b \sqrt{\cos^2 \theta + \left(\frac{r_{in}}{z_b}\right)^2 - 1} \quad (3.25)$$

$$l_{max} = z_b \cos \theta + z_b \sqrt{\cos^2 \theta + \left(\frac{r_{out}}{z_b}\right)^2 - 1} \quad (3.26)$$

(all other cases are simpler and require a single integral in the intensity calculation).

From the knowledge of intensity we can calculate the incoming photons' number density from the BLR as

$$n(d\Omega) = \frac{I(d\Omega)}{\epsilon m_e c^3} \quad (3.27)$$

The integration over the photon energy ϵ in scattering rate integrals (equations 2.17, 2.19) is a δ -function in this case, and so the innermost integral now becomes

$$\begin{aligned} \int_{\epsilon} n_{ph}(d\epsilon, d\Omega_{ph}) \frac{dC(\epsilon, \mu_{ph}, \gamma)}{d\epsilon_s d\Omega_s} \delta(\epsilon - \epsilon_\alpha \gamma (1 - \beta \mu_{ph})) d\epsilon \\ = n_{ph}(d\Omega_{ph}) \frac{dC(\epsilon = \epsilon_\alpha \gamma (1 - \beta \mu_{ph}), \mu_{ph}, \gamma)}{d\epsilon_s d\Omega_s} \end{aligned} \quad (3.28)$$

where $\epsilon_\alpha \gamma (1 - \beta \mu_{ph})$ is the H α line energy boosted in to the blob frame.

3.3.2 Monoenergetic Approximation for BLR Radiation

It is interesting to compare how the observed IC spectra would depend on the frequency at which the BLR radiates using the model described in this section. The IC produced luminosity scales with the energy density of the EC targets below the peak energy. Above the peak energy, however, it scales with their number density (as the IC cross section falls off with incoming photon energy in the Klein-Nishina regime). Given the same BLR luminosity, an H β radiating

3.3. BROAD LINE REGION PHOTONS

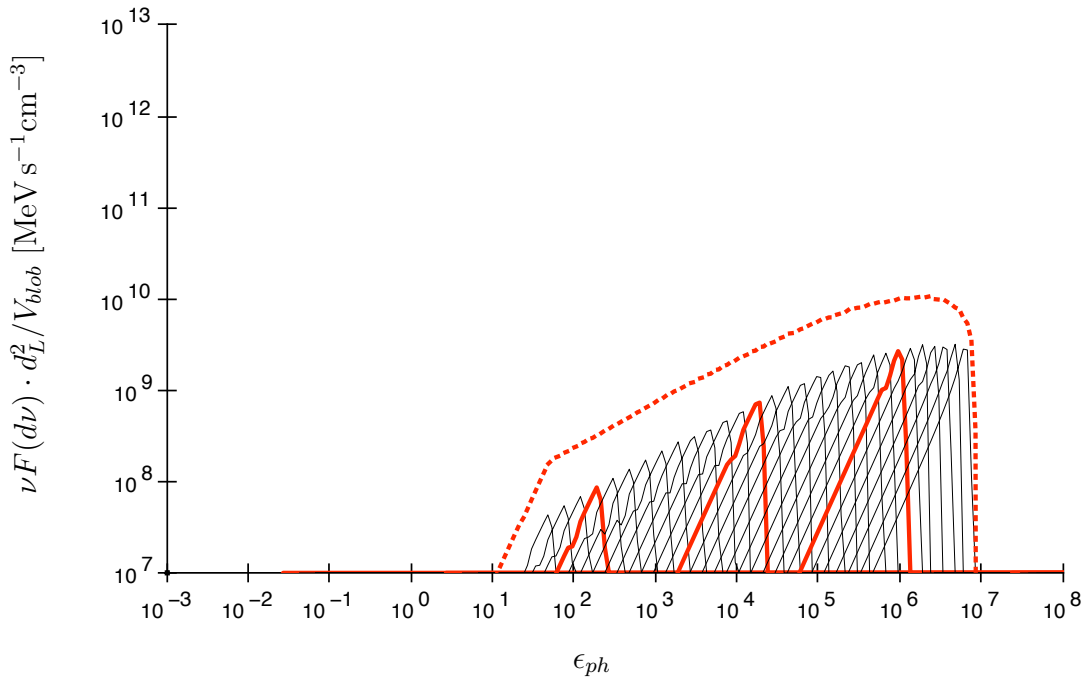


Figure 3.5: The dashed red line represents the upscattered BLR radiation by a power-law distributed electrons ($p = 2$), given in the observer's frame. Each black curve is a spectrum from monoenergetic electrons. The solid red lines correspond to the spectra generated by electrons separated by a decade in energy.

BLR will have a lower number density than a BLR that is radiating in $H\alpha$, since the $H\beta$ frequency is about 1.3 times higher than $H\alpha$. However, optical depth due to $H\alpha$ is higher than $H\beta$, giving rise to a deeper absorption feature in TeV part of the spectrum. This is evident from the comparison of spectra in figure 3.6. It can be also seen that $H\alpha$ and $H\beta$ BLR spectra converge after a few hours in observer's frame, i.e. the $H\alpha$ TeV spectrum gives rise to a more dramatic flux rise and the change of the slope (see Chapter 5 for further details on simulations of spectra).

3.3.3 Estimating the BLR radius

The size of the BLR r_{out} can be derived from the knowledge of the ionisation parameter, which is the ratio of ionising photon density to electron density, U (see e.g. Wandel 1997)

$$U = \frac{Q_{ion}}{4\pi r_{out}^2 c n_e} \quad (3.29)$$

where the ionising photon flux (number of ionising photons per unit time) is

$$Q_{ion} = \int_{E_n}^{\infty} \frac{F(E)}{E} dE \quad (3.30)$$

where $F(E)$ is the luminosity per unit energy, and the lower limit $E_n = 13.6$ eV. The ionising luminosity is then

$$L_{ion} = \int_{E_n}^{\infty} F(E) dE \quad (3.31)$$

We can now define the mean energy of ionising photon

$$\langle E_{ion} \rangle = \frac{L_{ion}}{Q_{ion}} \quad (3.32)$$

This then gives a theoretical estimate of the BLR radius

$$r_{out} \equiv \left(\frac{Q_{ion}}{4\pi c U n_e} \right)^{\frac{1}{2}} = \left(\frac{L_{ion}}{4\pi c \langle E_{ion} \rangle U n_e} \right)^{\frac{1}{2}} \quad (3.33)$$

3.3. BROAD LINE REGION PHOTONS

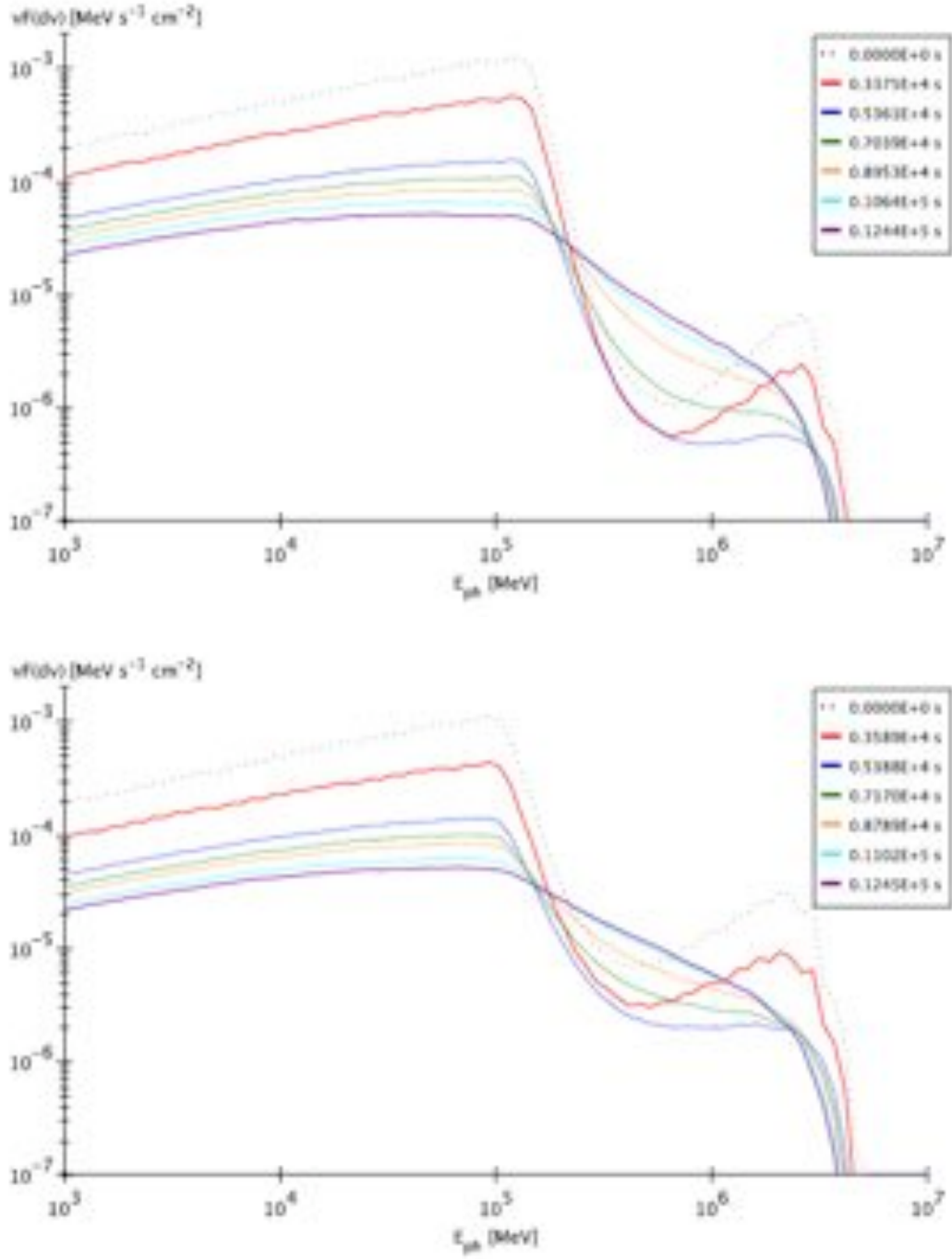


Figure 3.6: Spectra due to BLR photons radiating at $H\alpha$ (656 nm, upper panel) and at $H\beta$ (486 nm lower panel) from 1 GeV to 10 TeV. For a constant BLR luminosity, $H\alpha$ radiating BLR shows a stronger absorption feature than for the $H\beta$ radiating case. The ridges seen are an artifact of binning (here 20 energy bins per decade) as the integration routine used has the requested accuracy of about 10%.

3.3. BROAD LINE REGION PHOTONS

Typical values in the gas emitting the high-excitation broad lines are $U \sim (0.1-1)$ and $n_e \sim (10^{10}-10^{11} \text{ cm}^{-3})$ (e.g. Rees et al. 1989). However, this is a simplistic estimate. In reality how the BLR radius depends on other quantities given in equation above will depend on the waveband. Kaspi et al. (2005) have derived empirical relationships between the characteristic BLR size and Balmer emission line, X-ray, UV and optical luminosities. The slope of the power law is no longer 0.5 but varies, going up to 0.7 for the X-ray waveband.

Integration Limits. Limits on the incoming photon solid angle (Ω) will depend on whether the blob is inside or outside of the BLR. If the blob is inside, then the radiation is arriving at the blob from all angles ($\mu = [-1, +1]$). However, depending on the relative size of the disc, it may present a significant obstruction, and so the line of sight integral may only extend as far as the disc (i.e. in the case of angles lower than $\arctan\left(\frac{R_{disc,out}}{z_b}\right)$). This would also be true when the blob is outside of the BLR, but in that case there would be an outside limit on the angles, be put by the tangent to the outer BLR radius, $\arcsin\left(\frac{r_{out}}{z_b}\right)$.

The photon energy ϵ is constrained by the condition given by the equation 2.16. It should also be noted that even in the case of the approximation in which all the BLR power is radiated at a single frequency, the boosted radiation will still have a spread of incoming frequencies in the blob frame. However, this spread is only due to the incoming (boosting) angle. The blob will see a monochromatic beam of a different energy coming in from each direction. The incoming photon energy is therefore a direct function of its angle, which removes one dimension of integration (ϵ) in the scattering rate calculation

$$\dot{n}_{ph}(d\epsilon_s, d\Omega_s) = \int_{\gamma} n_e(d\gamma) \int_{\Omega_{ph}} \int_{\epsilon} n_{ph}(d\epsilon, d\Omega_{ph}) \frac{dC(\epsilon, \mu_{ph}, \gamma)}{d\epsilon_s d\Omega_s} \delta(\epsilon - \epsilon_{\alpha} \gamma (1 - \beta \mu_{ph})) d\epsilon d\Omega_{ph} d\gamma \quad (3.34)$$

where ϵ_{α} corresponds to the energy of the H α line (656.3 nm).

An example of the spectrum resulting from the upscattering of the BLR photons is presented in figure 3.5.

Chapter 4

Temporal Evolution of Particle and Photon Spectra

In this chapter the mathematical details of the temporal evolution of the particle population are discussed, as well as the evolving observed photon spectra and lightcurves. Some examples of the evolving spectra are then given, as a comparison with other authors' time-dependent models. Applications (with various scenarios) and results are discussed in detail in the next chapter.

Technique. There are two techniques that are used to predict the observed time-dependent spectra. One technique is Monte Carlo simulation and the other is the kinetic equation treatment (see Coppi 1992). The Monte Carlo technique simulates the history of interactions for individual particles, and calculates the values of the quantities such as particle flux and the SED by averaging over a large number of such histories. Monte Carlo is not a method suitable for the time-dependent calculations. Apart from being too slow, fluctuations in random numbers that it generates make it difficult to use in fits to the observational data which rely on the numerical calculations of the gradients. It also tends to have quite poor statistics at the high energies. The kinetic equation approach, on the other hand, provides complete information on the system, and is suitable for describing the temporal evolution of SEDs, by solving the integro-differential equations and calculating the SEDs in discrete time steps. The difficulties of this method lie mainly in having to deal with widely differing timescales that depend on both energy and the process in question. Apart from this, numerical integrations can be very time-consuming. In this thesis the kinetic equation treatment is used, since the motivation for this work is to eventually be able to

perform fits to the observations.

4.1 Continuity equations for electron spectra

It is noteworthy that in this thesis emission is modelled to originate in pair plasmas. Both electrons and positrons undergo the same interactions. Here both types of particles are referred to just as “electrons”.

The kinetic equation that describes the change of the electron spectrum in time due to various competing particle energy loss and gain processes can be written as

$$\frac{\partial n_e(d\gamma; t)}{\partial t} = Q_e(\gamma, t) - \frac{\partial}{\partial \gamma} (\dot{\gamma} n_e(d\gamma; t)) + \int_{\gamma}^{\infty} n_e(d\gamma; t) F(\gamma, \gamma_k) d\gamma_k - \frac{n_e(d\gamma; t)}{T_{KN}} \quad (4.1)$$

where $n_e(d\gamma, t)$, the electron number density per unit interval of γ (see e.g. Zdziarski 1988) is also a function of time t as measured in the emitting blob frame (1.2) and it is calculated from the start of a simulation (see end of Chapter 1.3.3 for the explanation on the notation used). The **first term** in equation 4.1 is the injection rate $Q_e(\gamma, t)$ of electrons and positrons into the emission region that is usually described by a power law between energies γ_{min} and γ_{max}

$$Q_e(\gamma, t) = Q_0 \gamma^{-p} \Theta(\gamma - \gamma_{min}) \Theta(\gamma_{max} - \gamma) f(t) \quad (4.2)$$

where $f(t)$ can be a time constant or a discontinuous injection (Q_0 and p are typically kept as free parameters, due to the lack of the detailed knowledge of the central engine’s energy extraction mechanisms). In the simulations in this thesis injection is assumed to be instantaneous.

In the **second term** in equation 4.1, the energy change $\dot{\gamma}$ in equation 4.1 describes the continuous processes, for which the evolving spectrum can be well described by the average change of all particles within one energy bin. Continuous gains have a positive sign and are due to the acceleration process. Here a simplistic treatment is employed in one of the scenarios, rather than a detailed modelling of the shock acceleration (see Drury 1983). Particles accelerate on a unique, energy-independent timescale t_{acc} . Continuous losses are negative in sign and are due to

4.2. COEFFICIENTS

the synchrotron radiation¹, with the magnetic energy density $U_B = B^2/(2\mu_0)$

$$\dot{\gamma} \equiv \dot{\gamma}_{acc} + \dot{\gamma}_{sync} = \frac{\gamma}{t_{acc}} - \frac{4}{3} \frac{\sigma_T}{m_e c} U_B \gamma^2 \quad (4.3)$$

The **third** and the **fourth term** in equation 4.1 describe the (discrete) IC gains and losses at a particular electron energy γ , respectively (as described in equations 2.19 and 2.17). Factor $1/T_{KN}$ marks the fractional decrease of the number of electrons at energy γ .

Note that sometimes other losses, such as adiabatic expansion, particle escape or pair annihilation are considered. Adiabatic expansion may not be significant at the timescales considered here. Pair annihilation should also not be of importance in relativistic environments with densities up to about 10^9 cm^{-3} (see Böttcher et al. 1997). Particle escape is a process that can in practice only be parametrised (it is typically done with an energy-independent escape timescale). Here it is not included.

4.2 Coefficients

In the rate calculations, one can in practice disentangle the term that describes the geometry of the ambient fields and the cross section of their interaction with particles from the term that describes the conditions in the emission region. This can be utilised in numerical calculations of rates and spectra, which typically suffer from being too slow. By “pre-calculating” the coefficients that do not depend on the emitting region, a lot of computing time can be saved, and allows the experimentation with the different particle number densities and spectral shapes, magnetic field strengths, blob radii and shock formation distances along the jet.

If one defines λ_{ij} as the fraction of electrons leaving bin i to *enter* bin j per unit time, then the rate of electrons migrating from i to j is

$$\dot{N}_{ij} = \frac{dN_{ij}(t)}{dt} = \lambda_{ij} N_i(t) \quad (4.4)$$

where $N_i(t)$ is the particle content of the bin i at time t .

¹Also the Inverse Compton energy loss in Thomson regime can be modelled with a continuous loss term $\dot{\gamma}_T$, with a photon energy density U_{ph} averaged over all energies and angles.

Similarly, the total rate of electrons that have left bin i in a given timestep, and redistributed themselves over a range of lower electron energies, is

$$\dot{N}_i = \frac{dN_i(t)}{dt} = -\lambda_i N_i(t) \quad (4.5)$$

It is obvious that $\lambda_i = \Sigma \lambda_{ij}$. The physical meaning of λ_i and λ_{ij} is, respectively, the inverse of the typical lifetime of electrons in energy bin i before migrating from it and for electrons to migrate from bin i to bin j due to the loss processes (here, only ICS is modelled with this scheme). These coefficients represent the geometry of the target photon fields and the physics of the photon-electron interaction, which in the case of the external fields does change as the blob progresses outwards, but one can take it to be constant over a chosen small timestep T on which the particle spectrum changes. For EC this term does not depend on the parameters of the blob, but only its surroundings (and the nature of the interaction). Even during the typical observation times of 15 min – few hours, which typically translates into about a couple of hours to about a day in the AGN frame (depending on the Doppler factor), this term will change slowly. It is therefore convenient to calculate this matrix λ_{ij} at different distances along the jet, and then interpolate for the intermediate values. This also gives the numerical flexibility to experiment with different electron spectra and blob parameters, for the same ambient conditions².

The quantities in equation 4.4 and 4.5 are integrated over energy bins. If one writes the quantities as number density differential in energy as³

$$\dot{n}(d\gamma_j; t) = \int_{\gamma_i} n_i(d\gamma_i, t) \left[\int_{\Omega_s} \int_{\Omega} \int_{\epsilon} n_{ph}(d\epsilon, d\Omega) \frac{dC(\epsilon, \gamma)}{d\epsilon_s d\Omega_s} \delta(\gamma_j - (\gamma - \epsilon_s)) d\epsilon d\Omega d\Omega_s \right] d\gamma_i \quad (4.6)$$

for electron gains at energy γ_j , due to electron arriving from all possible higher

²Note that for SSC the target field is dependent only on blob parameters, so the approach of λ_{ij} coefficients cannot be applied, however, one can still speed up the subsequent numerical calculations by pre-calculating the coefficients which represent the term that is still independent - the angle integrated IC cross-section.

³Note that the subscript e in n_e is dropped here for simplicity.

4.2. COEFFICIENTS

energies, and

$$\dot{n}(d\gamma_i; t) = \int_{\gamma_j} n_i(d\gamma_i, t) \left[\int_{\Omega_s} \int_{\Omega} \int_{\epsilon} n_{ph}(d\epsilon, d\Omega) \frac{dC(\epsilon, \gamma)}{d\epsilon_s d\Omega_s} d\epsilon d\Omega d\Omega_s \right] d\gamma_j \quad (4.7)$$

for losses at energy γ_i (these two are the same as the equations 4.8 and 4.9), it is obvious that only the outer integrals differ. The term in square brackets in effect represents the previously defined λ_{ij} divided by the width of energy bin j , if the spectrum is in the form of a histogram. Then the total gain at bin j due to the electrons coming from all upper bins (i) can be calculated as a summation

$$\frac{\Delta \dot{n}(t)}{\Delta \gamma_j} = \sum_i \frac{\lambda_{ij}}{\Delta \gamma_j} \frac{n_i(t)}{\Delta \gamma_i} \Delta \gamma_i = \sum_i \lambda_{ij} \frac{n_i(t)}{\Delta \gamma_i} \frac{\Delta \gamma_i}{\Delta \gamma_j} \quad (4.8)$$

and the total loss in bin i is then

$$\frac{\Delta \dot{n}(t)}{\Delta \gamma_i} = -\sum_j \frac{\lambda_{ij}}{\Delta \gamma_j} \frac{n_i(t)}{\Delta \gamma_i} \Delta \gamma_j = -\lambda_i \frac{n_i(t)}{\Delta \gamma_i} \quad (4.9)$$

The approach in which the spectrum is divided into a number of energy bins of finite widths may have a poor treatment of losses that are lower than the binwidth. In theory one should integrate over all energies in the initial energy bin i and all energies in the final energy bin j to get the precise rate. Then the number density could still be kept constant over energy bin, since it does not change significantly. In most cases one finds that the two methods yield the same results⁴. For the “problematic” cases, an approach as outlined in Appendix A may be used to avoid numerical problems of the code.

From the numerical point of view, the continuity equation 4.1 needs to be rewritten in terms of the particle number density n integrated over the energy bin

$$\frac{\Delta n_i}{\Delta t} = Q(\gamma_i, t) \Delta \gamma_i - \frac{\dot{\gamma}_{i+1} n_{i+1}}{\Delta \gamma_{i+1}} + \frac{\dot{\gamma}_i n_i}{\Delta \gamma_i} + \sum_{k=i+1}^{k_{max}} \lambda_{ki} n_k - \lambda_i n_i \quad (4.10)$$

Here the second and the third term on the right hand side are gains and losses in bin i due to continuous processes, and the fourth and the fifth are the discrete

⁴Numerical note: In many cases the double integral over the initial and final energy bin needs only a few function evaluations. However, a large number of function evaluations may be required in cases when the initial and final electron energies are close together the function may have large gradients or when the function may require a large number of integration steps.

gains and losses i , with $\lambda_i = \frac{1}{T_{KN}}$.

The emitted photon spectrum can also be calculated as a sum over the pre-calculated coefficients multiplied with the electron spectrum

$$\dot{n}_{ph}(d\epsilon_s, d\Omega_s) = \sum_i n_i(d\gamma_i) \zeta_{i,s} \quad (4.11)$$

Calculation of the coefficients λ_{ij} and $\zeta_{i,s}$, although numerically intense, allows to subsequently simulate the changes in emission region parameters with minimal computational effort. Also, it allows the resulting IC scattered photon spectra to be calculated as a simple sum.

4.3 Observed Spectrum

The observed flux density [$\text{J Hz}^{-1} \text{s}^{-1} \text{m}^{-2}$], after accounting for the boosting (δ) and the redshift (z) of the object, can be calculated as

$$F_{obs}(d\nu_{obs}; \varphi_{obs}, \theta_{obs}) = \delta^3 I(d\nu, d\Omega) \frac{\pi R_b^2}{d_L^2} (1+z) \quad (4.12)$$

from the intrinsic intensity $I(d\nu, d\Omega)$ (see e.g. Katarzynski et al. 2001), or from the emitted number density $\dot{n}_{ph}(d\epsilon, d\Omega)$ as

$$F_{obs}(d\nu_{obs}; \varphi_{obs}, \theta_{obs}) = \delta^3 \epsilon \dot{n}_{ph}(d\epsilon, d\Omega) \frac{V_b}{d_L^2} h (1+z) \quad (4.13)$$

where h is the Planck constant and d_L is the luminosity distance to the source which for Einstein – deSitter universe ($\Omega_0 = 2q_0 = 1$)

$$d_L = \frac{2c}{H_0} \left(1 + z - \sqrt{1+z} \right) \quad (4.14)$$

(see e.g. Lang 1999, or any earlier editions). The photon energy or frequency transforms as

$$\epsilon_{obs} = \frac{\delta}{1+z} \epsilon \quad (4.15)$$

The quantity that is usually plotted is $\nu F(d\nu)$, which transforms as

$$\nu_{obs} F_{obs}(d\nu_{obs}; \varphi_{obs}, \theta_{obs}) = \delta^4 \epsilon^2 \dot{n}_{ph}(d\epsilon, d\Omega) \frac{V_b}{d_L^2} mc^2 \quad (4.16)$$

4.3. OBSERVED SPECTRUM

These formulae are valid providing the blob is small enough so that the light crossing time is shorter than other relevant timescales that govern electron SED. However, when this condition is not met, the observed spectrum at any instant is a superposition of photon spectra produced by electrons from different parts of the blob, and hence from different epochs (see Chiaberge & Ghisellini 1999). Even for an emission region that evolves uniformly, the observer would at first only see the emission from the layers closest to them, as seen in the observer's frame (this direction, to which the slices are perpendicular, is obviously oriented at a very different angle in the blob frame). Later the deeper layers, with older electron spectra, would start to be observable along with the recently emitted radiation from top layers. Therefore the observer sees at any point in time the convolution of recently produced spectra from top layers and earlier spectra from the farther ones. For a spherical geometry, the observed instantaneous spectrum (before boosting) at a particular point in time could be written as

$$\dot{n}_{ph,inst,N} = \sum_{k=1}^N \dot{n}_{ph,N-k+1} \frac{V_k}{\sum_{k=1}^N V_k} \quad (4.17)$$

where N is the number of timesteps elapsed since the start of the changes in electron spectrum, and k is the number of the volume element ($k = 1$ being the slice closest to the observer). Here $n_{ph,N-k+1}$ is the differential number density as calculated in the equation 4.11. By integrating the instantaneous spectra in time one can obtain the received (unboosted) photon spectrum over the observing time Δt_{obs}

$$\dot{n}_{ph,integ}(M_1, M_2) = \frac{\sum_{N=M_1}^{M_2} \dot{n}_{ph,inst,N} \Delta t_N}{\Delta t_{obs}} \quad (4.18)$$

where M_1 and M_2 mark the point of the start and end of one observation, Δt_N is the length of the N th simulation timestep. The timestep of a simulation depends on the shortest timescale in the system (on which the electron spectrum changes). More precisely, it is derived from the largest fractional change $f_{i,max}$ in electron number density (over the spectrum) in the previous timestep and the permitted fractional change f_0 as $\Delta t_{N+1} = \Delta t_N \frac{f_0}{f_{i,max}}$. The volume slices of the sphere V_k , that are taken to be of a constant width equal to the distance of light travelled

4.4. NUMERICAL TREATMENT OF TEMPORAL EVOLUTION

in a timestep, are calculated as

$$V_k = \pi \int_{z_1}^{z_2} (R_b^2 - z^2) dz \quad (4.19)$$

By noting that $z_1 = kc\Delta t$ and $z_2 = (k+1)c\Delta t$, it is trivial to show that the volume element is

$$V_k = \pi \left(R_b^2 c\Delta t - \frac{1}{3} (c\Delta t)^3 (3k^2 + 3k + 1) \right) \quad (4.20)$$

In order to obtain the lightcurves, one sums the observed spectrum (after boosting) given by the equation 4.18 over all energies above the instrument's threshold, to get the total flux received over a particular observation time.

4.4 Numerical Treatment of Temporal Evolution

A static spectrum of particles, with a matching synchrotron distribution, is present in the emission region at time $t = 0$ s. This spectrum is modelled with a simple, truncated power law, with lower and upper cut-offs γ_{min} and γ_{max} and the slope p

$$n_e(d\gamma) = n_e \gamma^{-p} \frac{1-p}{\gamma_{max}^{1-p} - \gamma_{min}^{1-p}} \Theta(\gamma - \gamma_{min}) \Theta(\gamma_{max} - \gamma) \quad (4.21)$$

From this starting point, particles are allowed to cool down radiatively. The first observed spectrum always results from averaging over the observer's time interval which starts only at the observer's time equivalent to $t_{blob} = 2R_b/c$ from the start of the simulation. At this point the blob synchrotron number density is not dominated anymore by the initial synchrotron spectrum.

Synchrotron photons suffer attenuation due to self-absorption and they escape the emitting volume on an average timescale of $3R_b/4c$

$$\frac{dn_{ph,sy}(d\epsilon_{sy})}{dt} = A_{ph,sy}(d\epsilon_{sy}) - \alpha(\nu)cn_{ph,sy}(d\epsilon_{sy}) - \frac{n_{ph,sy}(d\epsilon_{sy})}{3R_b/4c} \quad (4.22)$$

where $A_{ph,sy}(d\epsilon_{sy})$ is the production rate of synchrotron photons of energy ϵ_{sy} . It can be seen that the loss timescale due to the joint effects of attenuation and

4.5. EXAMPLES OF SPECTRA

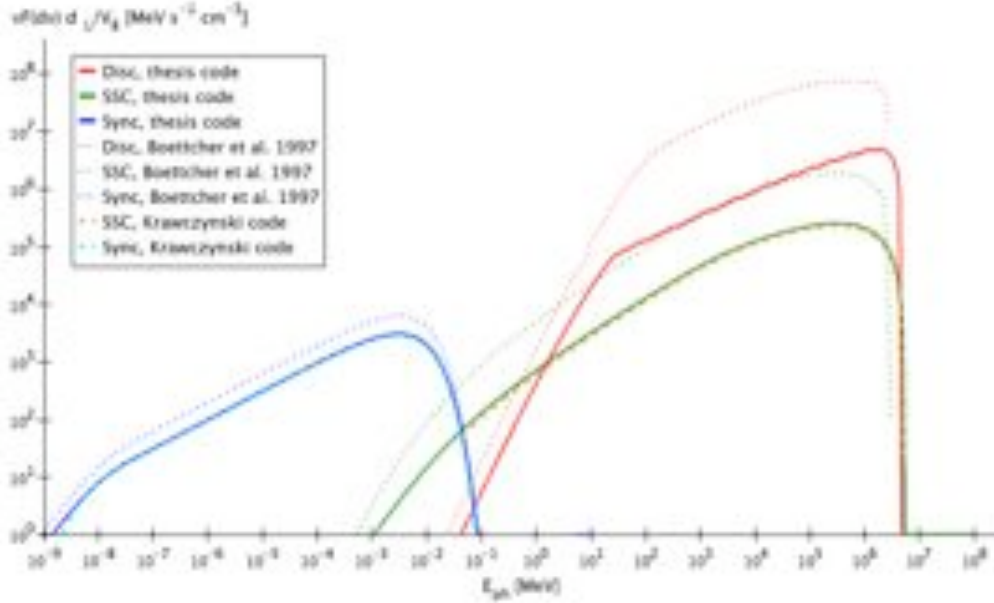


Figure 4.1: Comparison of individual instantaneous photon spectral components with Böttcher et al. (1997) parameters and against the code presented in Krawczynski et al. (2004), calculated in the observer’s frame of reference for $t = 0$ s. Spectra are normalised to the distance d_L to the observer and the volume of the emitting region V_B .

the photon escape from the volume is $T = (\alpha(\nu)c + 4c/3R_b)^{-1}$. By integrating this expression over a time interval $\Delta t = t_2 - t_1$ one arrives at the equation of evolution of the synchrotron number density in a timestep Δt

$$n_{ph,sy}(d\epsilon_{sy}; t) = n_{ph,sy}(d\epsilon_{sy}; t - \Delta t)e^{-\Delta t/T} + A_{ph,sy}(d\epsilon_{sy})T(1 - e^{-\Delta t/T}) \quad (4.23)$$

4.5 Examples of spectra

To test the method used in this thesis’ code, this section reproduces observations and scenarios that were fitted by several different authors with and without time-dependent numerical codes (namely Böttcher et al. 1997; Katarzynski et al. 2006).

Böttcher et al. (1997) employ a time-dependent model to study the effects of both EC and SSC on the particle distribution, the external component being ascribed to the accretion disc photons. They use the full Klein-Nishina cross-section to calculate the instantaneous emitted spectra at different points in time. The high-flux states of Mrk 421 are due to the synchrotron/IC cooling that fol-

4.5. EXAMPLES OF SPECTRA

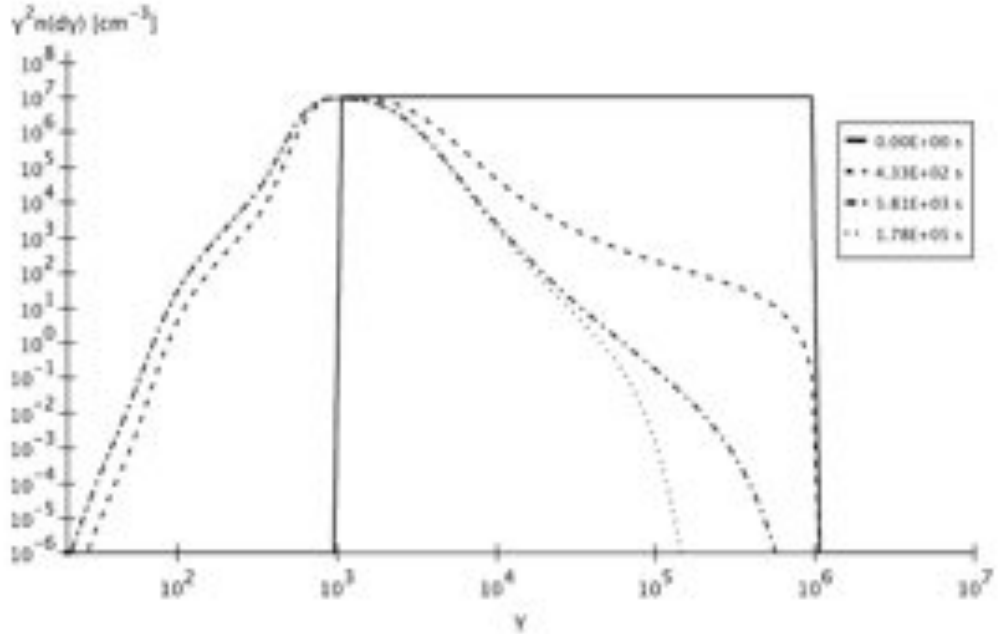


Figure 4.2: Evolving electron spectrum for the parameters as used in Böttcher et al. (1997): $n_e = 10^4 \text{ cm}^{-3}$, $R_b = 5 \cdot 10^{14} \text{ cm}$, $B = 0.05 \text{ G}$, $\gamma_{min} = 10^3$, $\gamma_{max} = 10^6$, $\Gamma = 20$, $p = 2$ (all of these are in the blob frame) and the observing angle of $\theta = 5^\circ$ (observer's frame); $z_b = 0.5 \text{ mpc}$ (the starting point along the jet), $L_{disc} = 10^{44} \text{ erg s}^{-1}$, $M_{BH} = 10^6 M_\odot$, $R_{disc,in} = 6R_g = 2.87 \cdot 10^{-4} \text{ mpc}$, $R_{disc,out} = 6 \cdot 10^6 R_g = 287 \text{ mpc}$ (given in the rest frame of the AGN). Note that times here are given in the observer's frame of reference, but the spectra themselves are plotted in the blob reference frame, unlike the corresponding photon spectra further on.

4.5. EXAMPLES OF SPECTRA

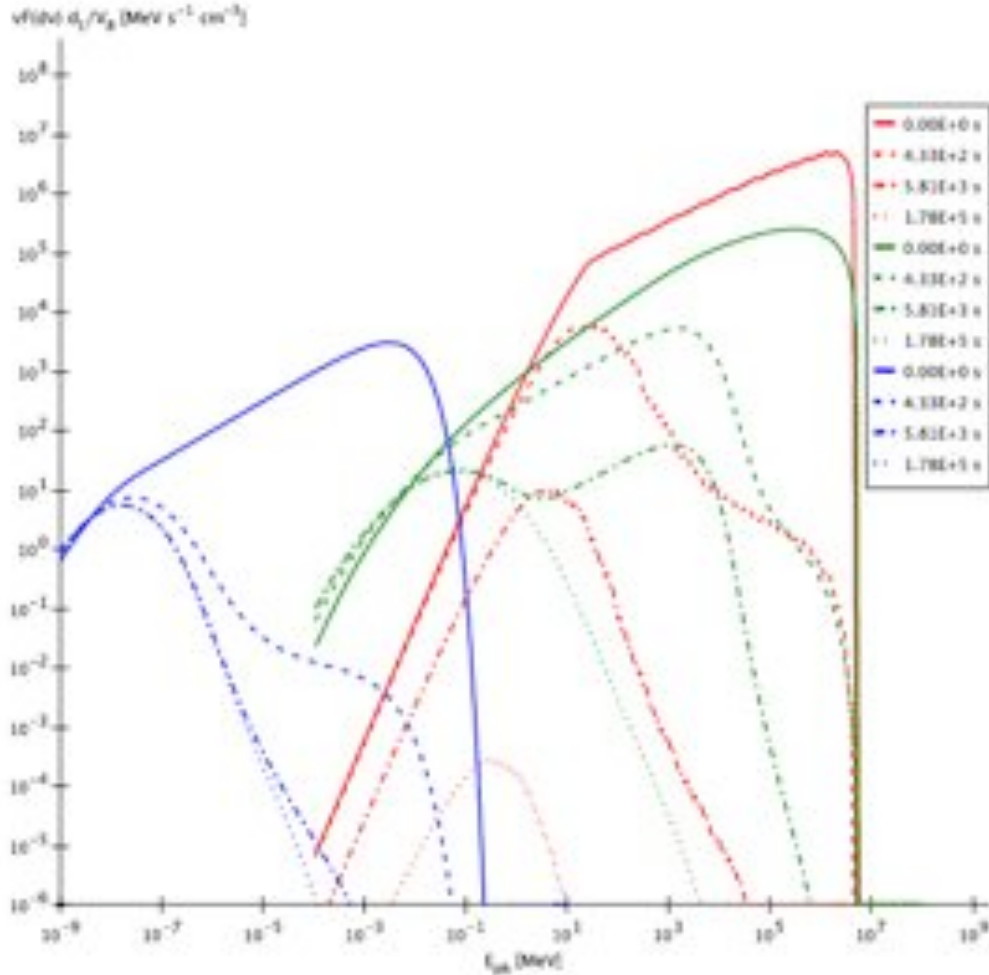


Figure 4.3: Evolving instantaneous photon spectrum due to synchrotron (blue lines), accretion disc EC (red) and SSC (green) losses without accounting for the different travel times of the light originating in various parts of the blob. Note that the observable parts of the spectrum are about an order or two of magnitude below the position of the synchrotron and the SSC peak, respectively. Here the scale is extended to many orders of magnitude below (causing the code's set lower boundary of the plotted IC spectra to be visible here) to give a better appreciation of various features in the evolving photon spectra and the connection to the shape of the corresponding electron spectra. Times are given in the observer's frame of reference.

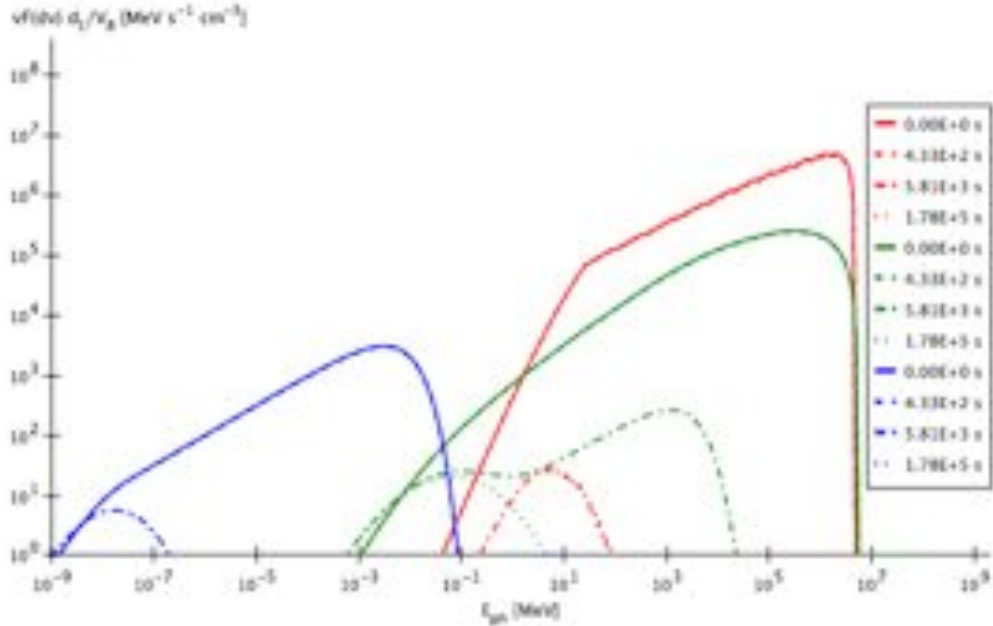


Figure 4.4: Evolving instantaneous photon spectrum due to synchrotron (blue lines), accretion disc EC (red) and SSC (green) losses, after correcting for the effect of the different travel times of the light arriving from various parts of the blob.

lows the injection/acceleration phase that is the cause of the initial power law spectrum of emitting particles. This scenario is reproduced here, for the same set of parameters. Observed instantaneous spectra are plotted for four different points in time (figure 4.3).

There seems to be a disagreement of about a factor of a few in the synchrotron peak height (figure 4.1). This might be due to the differences in the numerical treatment of the synchrotron radiation. It appears as this difference is further propagated into the calculation of the SSC spectrum, which is several times higher than the SSC peak calculated with this thesis' code. However, when the same scenario is run with the code used in Krawczynski et al. (2004), agreement is excellent with this thesis for both synchrotron and SSC spectra at $t = 0$ s (Krawczynski et al. 2004 code does not model EC processes). The EC component is just over an order of magnitude lower than in Böttcher et al. (1997). These differences may be ascribed to the fact that this thesis' model is considering the Planck energy distribution for the accretion disc radiation rather than a single-energy approximation, which can be off by as much as five orders of magnitude in

4.5. EXAMPLES OF SPECTRA

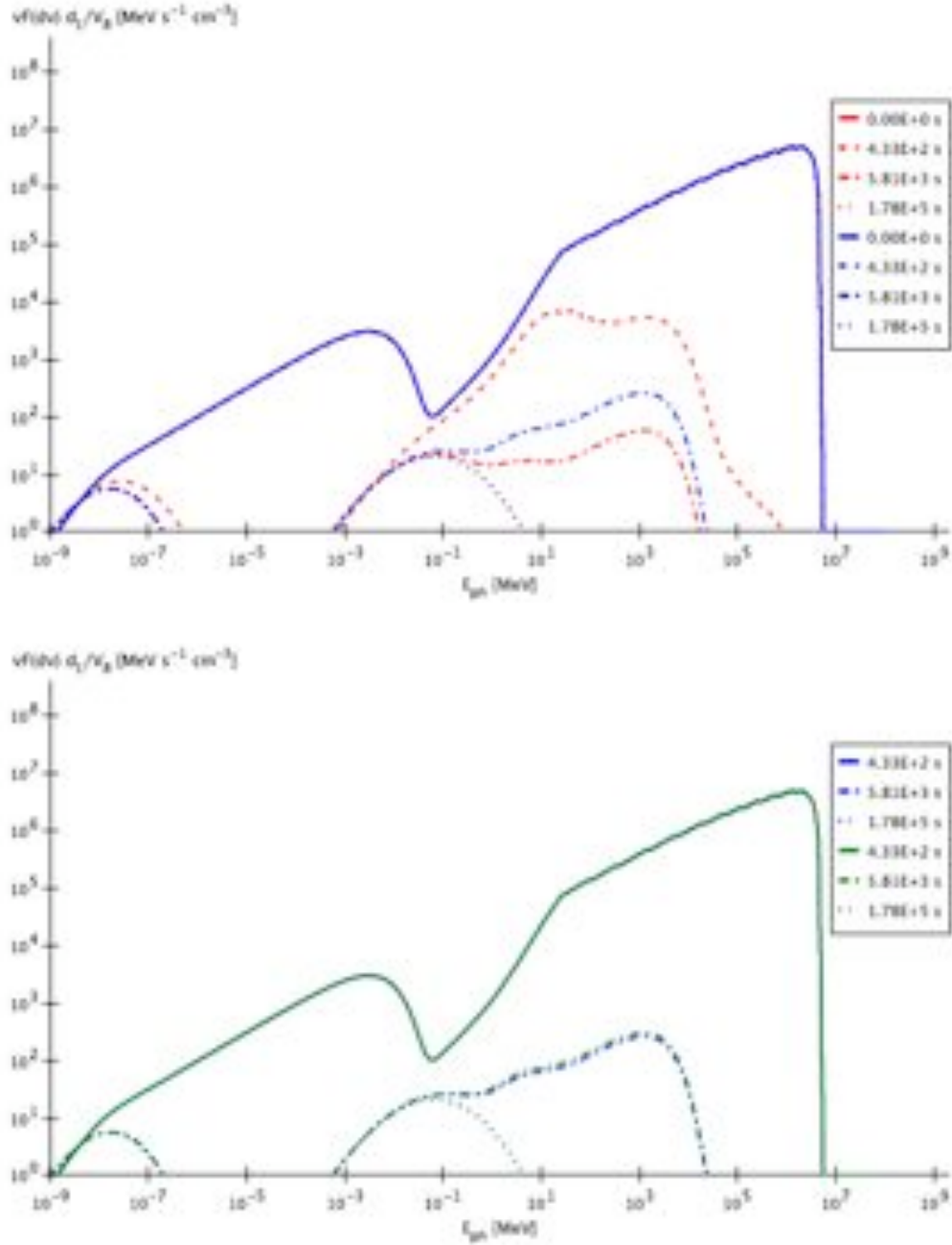


Figure 4.5: The photon spectra from figure 4.4 summed up to produce the overall observed SED. Red lines (in the upper panel) represent the instantaneous spectra assuming that the radiation from all parts of the blob arrives to the observer at the same time. Blue lines (both panels) are the instantaneous spectra that have been corrected for the different light travel times. Green lines (lower panel) show the time-averaged spectra after correcting for the different travel times.

both directions. It is noteworthy that the same treatment of the disc radiation as in Böttcher et al. (1997), with the $1/4 \cos \theta$ factor included, results in the discrepancy of nearly two orders of magnitude instead⁵. Due to the heavy redshifting, the disc radiation becomes unimportant as a source of targets for ICS by about 2-3 mpc away from the central engine.

The subsequent evolution of all of the components also deviates from the behaviour seen in their model, yielding different spectral shapes. This is due to a different treatment of particle cooling. The particle losses at each energy bin are modelled here as a distribution over a range of lower-energy bins, causing there to be a competition between the gains and losses in each energy, rather than considering only the average energy loss per particle energy bin. It can be seen in figure 4.2 that this treatment yields very large electron losses for the parameters used. Within the first several minutes, a large portion of electrons has undergone strong cooling in the proximity of the disc, which radiates most strongly in the EUV – soft X-ray regime. The shape of the subsequently evolving electron spectra is characteristic of this initial cooling due to the disc. Below the initial low-energy cut-off there is a population of electrons that had suffered catastrophic losses. The bump immediately below the initial cut-off energy is characteristic of the disc cooling process, whereas the additional bump at somewhat lower energies (gamma factors of a 100) represents cooling due to SSC. The shape of the cooled electron spectra are clearly reflected in the emitted synchrotron and the EC spectra (figure 4.3). The SSC spectral shape is appropriately somewhat more complex. This scenario illustrates well the importance of a proper, self-consistent treatment of the electron cooling, as the interaction with the scattering targets gives the electron spectrum a characteristic shape, which will affect the emitted synchrotron radiation and, through it, again affect the electron cooling due to SSC. It also demonstrates the potential pivotal importance of the initial conditions of the system (including the position of the blob along the jet) for the subsequent evolution of the flare.

Figure 4.4 shows the spectra after accounting for the size of the emission region which causes spectra from different parts of the emitting blob to have different travel times. This means that the instantaneous spectra at each point are not “pure”, but mixed with the spectra from previous timesteps, i.e. from deeper

⁵This dependence on the cosine of the polar angle causes the number density to approach infinity when skimming the disc. However, for small enough angles, this term approaches $1/4$.

4.5. EXAMPLES OF SPECTRA

layers of the emission region. In such a case, the second curve will mostly consist of the spectra produced at $t = 0$ s, which is why the second curve, at about 7 min later, overlaps on this plot with the line from $t = 0$ s. The disc component is again seen to diminish rapidly as the emission region progresses outwards (all the times are in the observer's frame of reference). It can be seen that the evolution of the instantaneous spectra looks different when the size of the emission region is taken into account.

Figure 4.5 compares the total spectra (with contributions from all components summed up), for three different situations: instantaneous spectra not corrected for the light travel times in the blob and the spectra after this correction, the latter for both instantaneous and averaged case. In the upper panel, the top line is a superposition of three lines: both spectra at the $t = 0$ s, and the instantaneous spectrum corrected for travel times after about 7 min (the averaging time is 7 min also). The lower panel of figure 4.5 shows also the spectra that are averaged over a period of 7 min (the spectra are not plotted for the time $t = 0$ s). It can be seen that the instantaneous spectrum corrected for travel times is very different from the non-corrected one, but it is almost indistinguishable here from the averaged spectrum. This is due to the short averaging times which are smaller than the size of the emitting region.

Katarzynski et al. (2006) model the observed averaged spectra of four TeV blazars with a one-zone SSC scenario, having a truncated power-law electron distribution that is kept time-constant. Using the model of IR intergalactic background from Kneiske et al. (2004), they get a very good agreement with the observations. The model takes into account the full Klein-Nishina cross-section. Their scenarios are reproduced here (figure 4.7 and figure 4.8), including the EBL absorption model.

The agreement with Katarzynski et al. (2006) is excellent for Mrk 421 and Mrk 501 (figure 4.7), as is with Krawczynski et al. (2004) code when is run for the same Mrk 501 parameters (figure 4.6). There is a slightly more visible disagreement in the case of PKS 2155 and 1ES 1101 (figure 4.8). Precision of integration may also account for the discrepancies seen, as may the fact that in this thesis a newer, better resolved table from Kneiske et al. (2004) is used to model the intergalactic absorption along the line of sight. Also, in the original paper the value of the Hubble constant was 65 km/s/Mpc, lower than the one used here (70 km/s/Mpc). The overlay of the Katarzynski et al. (2006) curves

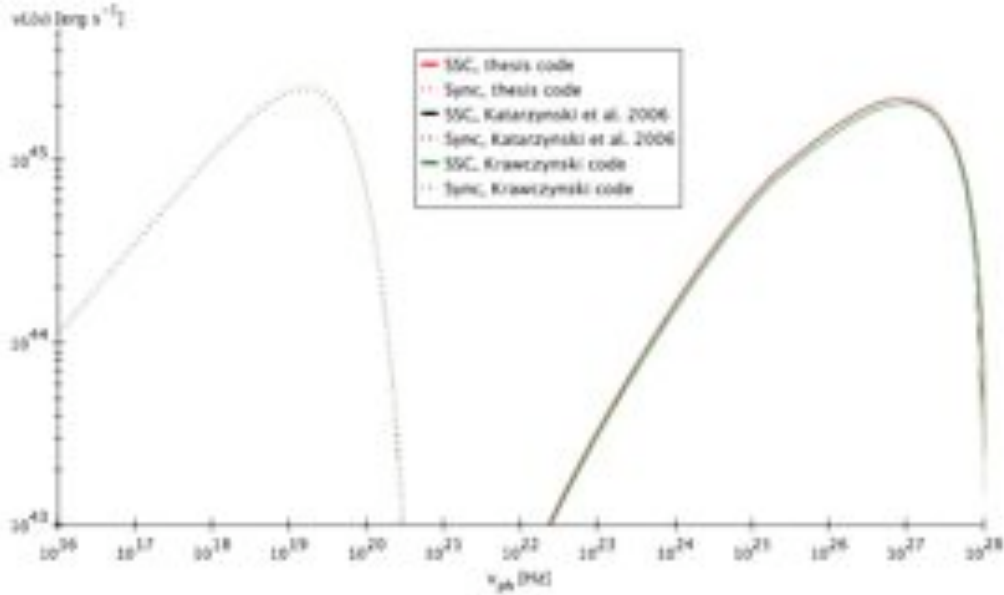


Figure 4.6: Comparison of the SSC scenario with Katarzynski et al. (2006) for Mrk 501 and against the code presented in Krawczynski et al. (2004).

with the ones produced in this thesis may have also produced some discrepancy.

Figure 4.9 shows the EBL optical depth for the redshifts relevant for the the four AGN plotted on figure 4.7 and figure 4.8.

It should be pointed out that in the code developed and used in this thesis, the integrals are evaluated with the two widely used CERN adaptive algorithm integration routines, namely Adaptive Gaussian Quadrature (DGAUSS) and Adaptive Quadrature for Multiple Integrals over N-Dimensional Rectangular Regions (DADMUL, see Genz & Malik 1980). Calculations were cross-checked against another package, CUBPACK (Cools & Haegemans 2003), and a good agreement is seen (consistent with the uncertainties).

4.5. EXAMPLES OF SPECTRA

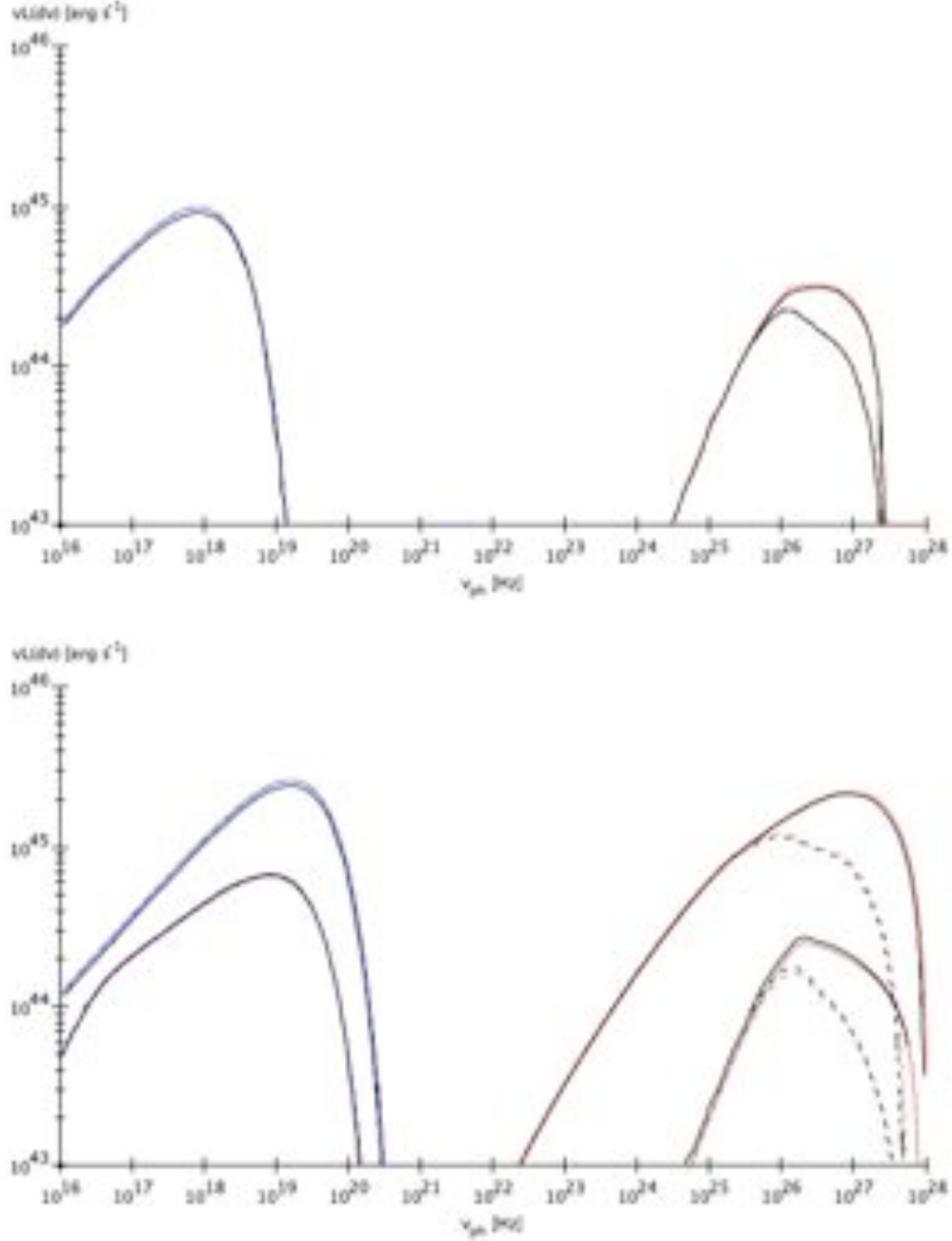


Figure 4.7: Observed spectra averaged over the observation time for Mrk 421 (upper panel) for parameters $K = 2.4 \cdot 10^3 \text{ cm}^{-3}$, $R_b = 1.3 \cdot 10^{16} \text{ cm}$, $B = 0.025 \text{ G}$, $\gamma_{\min} = 5 \cdot 10^4$, $\gamma_{\max} = 10^6$, $\delta = 23$, $p = 2$; and Mrk 501 (lower panel) for parameters $K = 5.3 \cdot 10^4$ ($1.6 \cdot 10^4$) cm^{-3} , $R_b = 1.7 \cdot 10^{15}$ ($1.5 \cdot 10^{15}$) cm , $B = 0.05 \text{ G}$, $\gamma_{\min} = 5 \cdot 10^3$ ($5 \cdot 10^4$), $\gamma_{\max} = 2.5 \cdot 10^6$ ($2 \cdot 10^6$), $\delta = 35$, $p = 2$ (2.3). For Mrk 501, values in brackets represent the parameters for the lower fluxes. Solid lines represent the intrinsic spectra, while dashed are the observed, absorbed spectra. K is related to the total number density n_e through $K = n_e \frac{1-p}{\gamma_{\max}^{1-p} - \gamma_{\min}^{1-p}}$. All the black lines represent the simulations by Katarzynski et al. 2006.

4.5. EXAMPLES OF SPECTRA

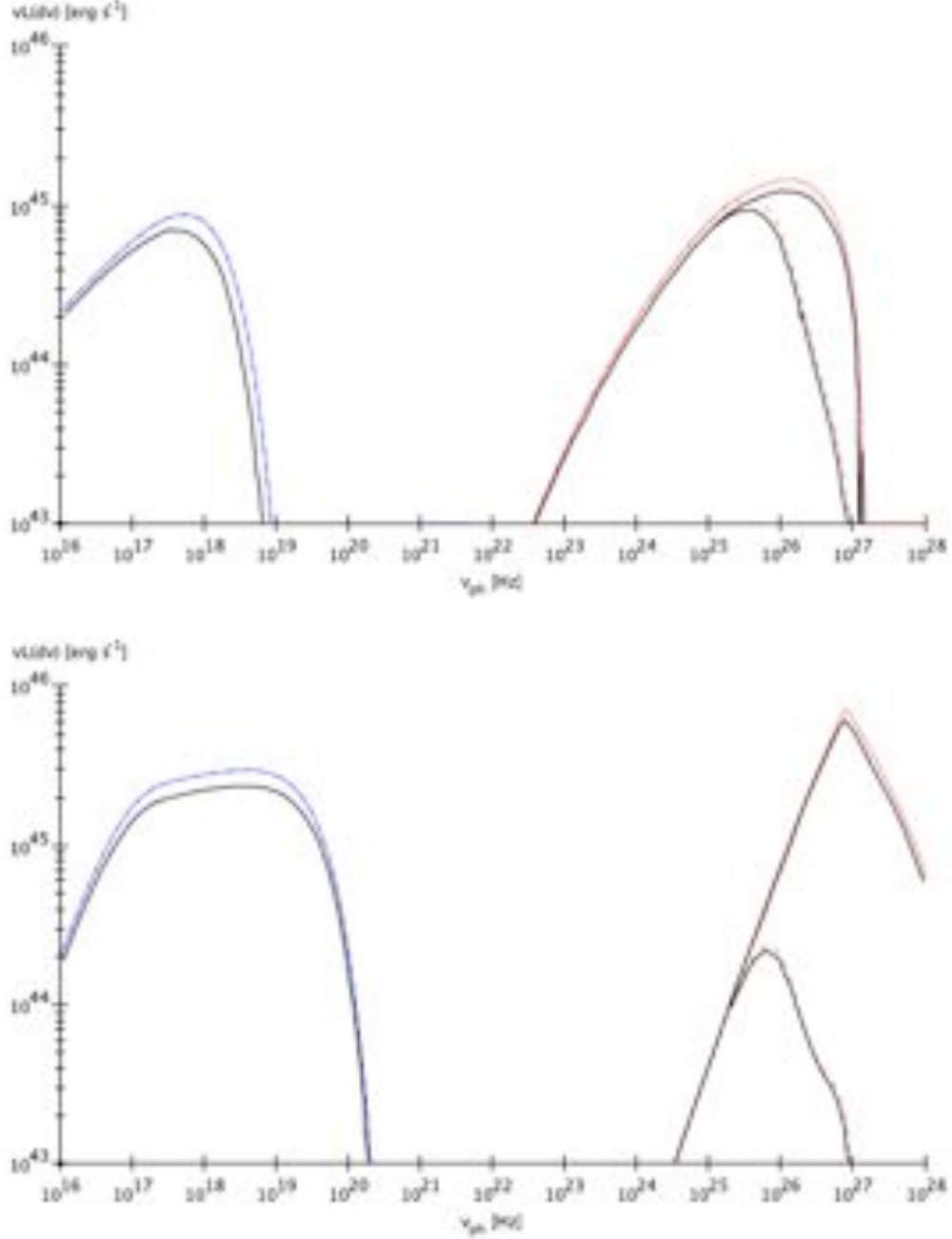


Figure 4.8: Observed spectra averaged over the observation time for PKS 2155 (upper panel) for parameters $K = 1.5 \cdot 10^4 \text{ cm}^{-3}$, $R_b = 6 \cdot 10^{15} \text{ cm}$, $B = 0.05 \text{ G}$, $\gamma_{min} = 1 \cdot 10^4$, $\gamma_{max} = 6 \cdot 10^5$, $\delta = 20$, $p = 2$; 1ES 1101 (lower panel) for parameters $K = 2 \cdot 10^9 \text{ cm}^{-3}$, $R_b = 6.3 \cdot 10^{15} \text{ cm}$, $B = 0.01 \text{ G}$, $\gamma_{min} = 2.2 \cdot 10^5$, $\gamma_{max} = 5 \cdot 10^6$, $\delta = 35$, $p = 2.8$ (note that the later simulation was done was a very dense blob).

4.5. EXAMPLES OF SPECTRA

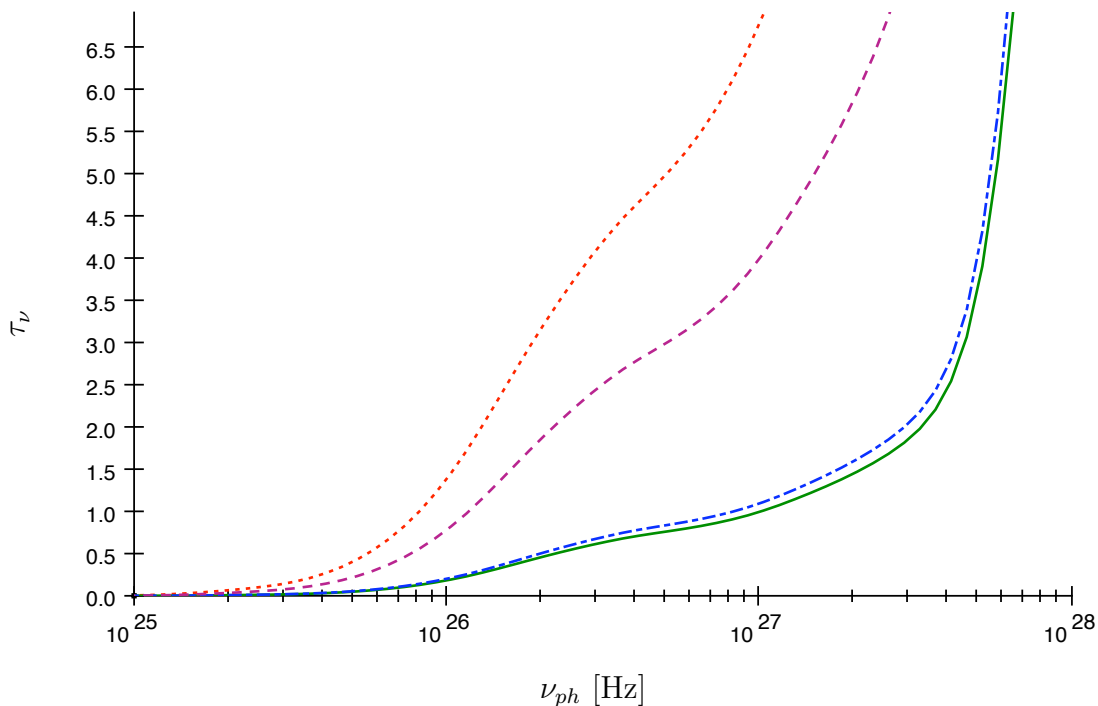


Figure 4.9: Optical depth due to the extragalactic absorption, for BL Lacs at four different redshifts: Mrk 421 at $z=0.031$ (solid line), Mrk 501 at $z=0.034$ (dot-dashed), PKS 2155 at $z=0.116$ (dashed) and 1ES 1101 at $z=0.186$ (dotted). The model for EBL is described in Kneiske et al. (2004). The slight bumps seen in the EBL curves are due to the distribution of the of the EBL soft photons (primarily redshifted starlight).

Chapter 5

Simulations of Observed Photon Spectra

This chapter explores different scenarios to model the observed BL Lac spectral distributions. The goal is to mimic the behaviour of the observed SEDs during the flare events, and reproduce features such as the rapid rise and fall-off times, X-ray – gamma-ray flux correlation, hardening of the photon spectra with the increasing flux, “orphan” TeV flares and X-ray variability without a TeV counterpart.

A simple way to test the numerical code is to compare it to the theoretical prediction in the domain of Thomson Scattering, e.g. for the electron spectrum between $\gamma = 10^2$ and $\gamma = 10^4$. The ratio of SSC to synchrotron luminosity is equal to the ratio of synchrotron to magnetic field energy density

$$\frac{L_{SSC}}{L_{sync}} = \frac{U_{sync}}{U_B} \quad (5.1)$$

Synchrotron energy density due to the a power law spectrum of electrons with cut-offs γ_{min} and γ_{max} (assuming the cut-offs don’t evolve) is

$$U_{sync} \equiv - \int_{\gamma_{min}}^{\gamma_{max}} n(d\gamma) \dot{\gamma} t_{res} d\gamma = \int_{\gamma_{min}}^{\gamma_{max}} n(d\gamma) \sigma_T c \left(\frac{3}{4} \frac{R_b}{c} \right) U_B \gamma^2 d\gamma \quad (5.2)$$

where $t_{res} = \frac{3}{4} \frac{R_b}{c}$ is the photon’s average residence time in the blob (see end of Chapter 1.3.3 for the explanation on the notation used). By substituting $n(d\gamma)$

with a normalised power law with cut-offs one arrives at

$$U_{sync} = \sigma_T R_{blob} n_e \frac{1-p}{\gamma_{max}^{1-p} - \gamma_{min}^{1-p}} \frac{\gamma_{max}^{3-p} - \gamma_{min}^{3-p}}{3-p} U_B \simeq \sigma_T R_{blob} n_e \frac{p-1}{3-p} \gamma_{min}^{p-1} \gamma_{max}^{3-p} U_B \quad (5.3)$$

Then for $p = 2$ the ratio of synchrotron to magnetic energy density is

$$\frac{U_{sync}}{U_B} = n_e \sigma_T R_b \gamma_{min} \gamma_{max} \quad (5.4)$$

and n_e the total number density of electrons (term $n_e \sigma_T R_b$ is actually the Thomson optical depth). This can now be used as a cross-check for the treatment used in the computer code (using the full Klein-Nishina cross-section):

1. For the upper cut-off of $\gamma_{min} = 10^3$ and lower there is over 20% difference. This is due to limitations of the numerical approach. The electron spectrum is divided into a fixed number of decades per bin. At low energies, electron losses due to IC are dominated by small losses and if they are lower than the binwidth, they are not included in the calculation of the photon spectrum. This causes the underestimate of the Compton luminosity. However, at these energies ($\lesssim 10^3$) electrons are feeble emitters and their contribution to the overall spectrum is mostly to the very lowest part of the IC spectrum. Also, in relativistic plasmas electrons are typically modelled with a power law with a lower cut-off $\gtrsim 10^3$.
2. For any lower cut-off and an upper cut-off of $\gamma_{max} \gtrsim 10^4$ the agreement with theory is excellent (within a percent) as for these values IC scattering is still in the Thomson regime and the emitted luminosity is strongly dominated by electrons $\gtrsim 10^3$.
3. For upper cut-offs of $\gtrsim 10^5$ there is nearly a 100% difference, and each subsequent decade in energy of γ_{max} adds an extra order of magnitude to the disagreement because of the overestimate of the IC luminosity by the Thomson approximation.

5.1 Timescales for relevant processes

The effect that some parameters can have on the emitted photon spectra can be considered by estimating the typical timescales for relevant processes which can be derived from the cooling rates in the Thomson regime

$$\dot{\gamma} = -\frac{4}{3} \frac{\sigma_T}{mc} U \gamma^2 \quad (5.5)$$

The estimates of the cooling timescales (in the blob frame) for a particle of energy γ for the synchrotron, SSC and EC due to the disc radiation in the Thomson regime are given by

$$t_{sync} \simeq \frac{77}{B_{-2}^2 \gamma^3} \text{s} \quad (5.6)$$

$$t_{SSC} \simeq \frac{1.16 \cdot 10^{14}}{n_{e6} R_{b14} B_{-2} \gamma^3} \left(\frac{1}{\gamma_{min}^{p-1} \gamma_{max}^{3-p}} \frac{3-p}{p-1} \right) \text{s} \quad (5.7)$$

$$t_{EC,disc} \simeq \frac{10^6}{\gamma} \frac{z_{b1}^2}{L_{disc44}} \Gamma_{jet}^2 \text{s} \quad (5.8)$$

where $z_{b1} = z_b/\text{mpc}$, $n_{e6} = n_e/10^6 \text{cm}^{-3}$, $R_{b14} = R_b/10^{14} \text{cm}$ and $L_{disc44} = L_{disc}/10^{44} \text{erg s}^{-1}$. Note that this approximation treats the disc as a point source and is poor for the very close distances from the disc. For the cooling timescales by EC due to the BLR photons, there does not seem to be a good approximation.

5.2 Simulations

The set of input parameters used in the first scenario is listed in table 5.1. In this case the only photon target fields considered are the disc and synchrotron photons.

It is useful to have some sort of a reference point when plotting the observed photon spectra. All of the simulated spectra here are compared to the sensitivities of the current measuring instruments. The two short lines in the X-ray energy range represent the 5σ point source detection sensitivity of the EPIC instrument on-board the XMM satellite (Watson et al. 2001) for a 1000 s integration time measurements. The lower (black solid) line shows the sensitivity in the 0.5 – 2 keV range, and the higher (navy solid) line is for 2 – 10 keV energy interval. The

5.2. SIMULATIONS

Table 5.1: Starting input parameters for the simulations (see figure 5.1, upper panel). Accretion disc parameters, given in the host galaxy rest frame: M_{BH} is the SMBH mass, L_{disc} is the accretion disc luminosity, η_{disc} is the accretion disc radiative efficiency, $R_{disc,in}$ and $R_{disc,out}$ are the inner and outer radii of the disc; blob parameters, given in the blob frame: n_e particle number density, R_b radius of the blob, B magnetic field strength, γ_{min} and γ_{max} the lower and upper cut-off Lorentz factors of the particle distribution, p slope of the particle spectrum, Γ_{jet} jet Lorentz factor; observer's parameters, given in the observers frame: θ_{obs} angle of the observer w.r.t. the jet axis, z redshift, t_{obs} observing time interval.

Disc		Blob		Observer	
M_{BH}	$10^6 M_\odot$	n_e	10^4 cm^{-3}	θ_{obs}	1°
L_{disc}	$10^{44} \text{ erg s}^{-1}$	R_b	$5 \cdot 10^{14} \text{ cm} = 0.16 \text{ mpc}$	z	0.031
η_{disc}	0.06	B	0.1 G	t_{obs}	600 s
$R_{disc,in}$	$6R_g = 2.87 \cdot 10^{-4} \text{ mpc}$	γ_{min}	10^3		
$R_{disc,out}$	$6 \cdot 10^6 R_g = 287 \text{ mpc}$	γ_{max}	10^6		
		p	2		
		Γ_{jet}	20		

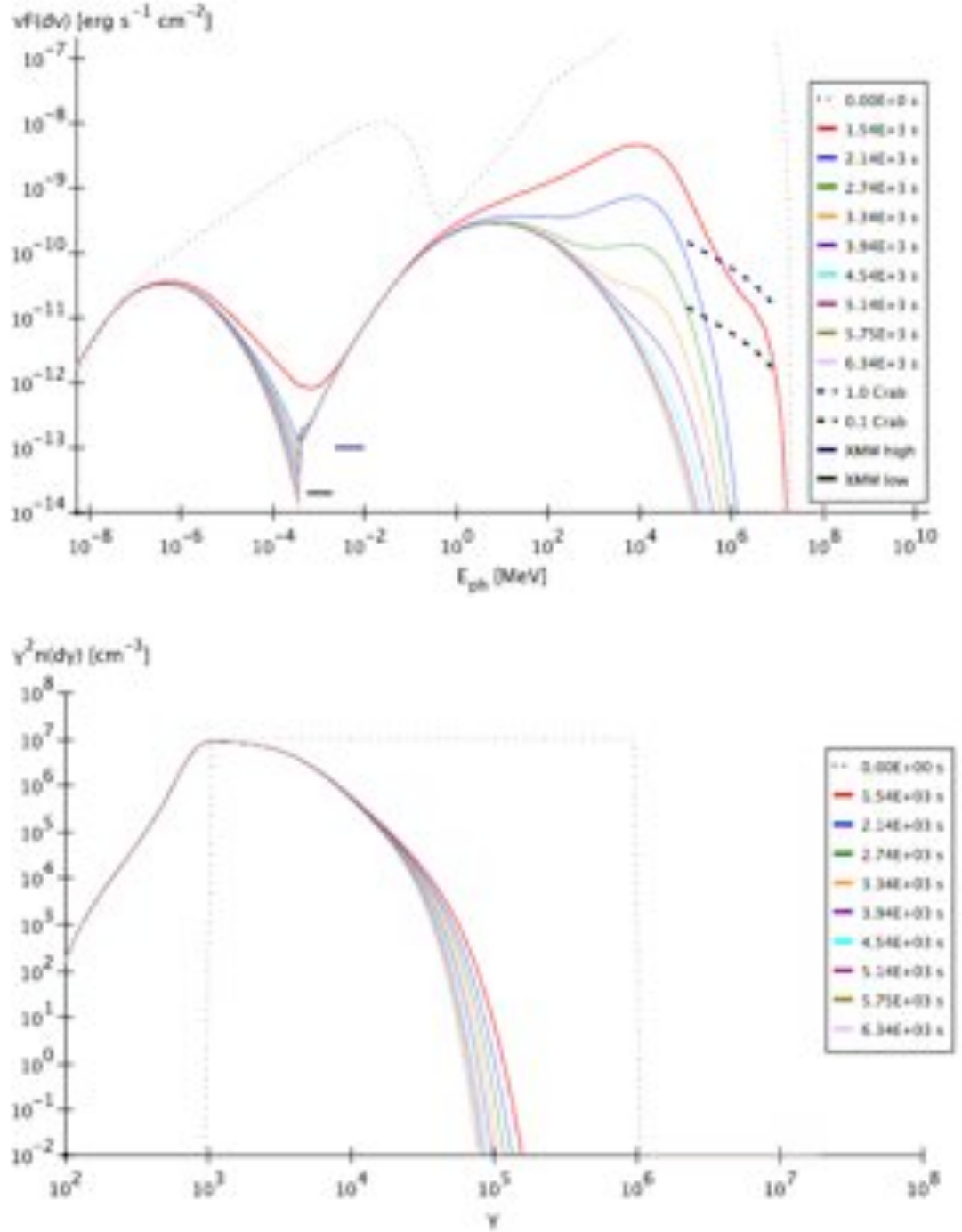


Figure 5.1: Evolving observed photon and electron spectra for a starting distance of 0.5 mpc. Photon spectra are averaged over the observer time intervals of 10 min for the parameters set in table 5.1. The first, dotted black line is the instantaneous spectrum at time 0 s, and the solid red line is an averaged spectrum over the first 10 min interval (which starts after a light crossing time of the blob, when boosted into the observer’s frame).

5.2. SIMULATIONS

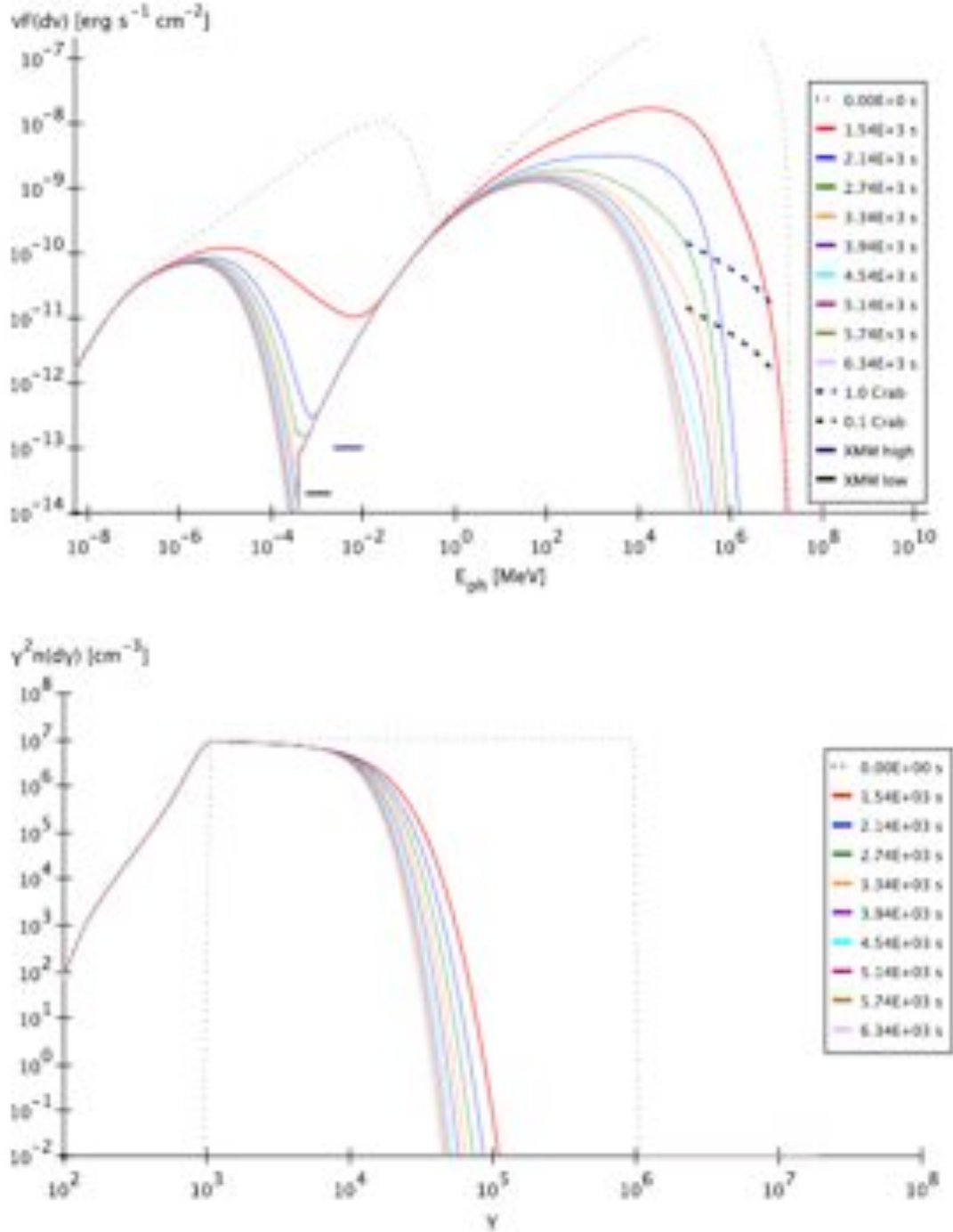


Figure 5.2: Evolving observed photon and electron spectra for a further out starting distance (2 mpc) with respect to figure 5.1 (see table 5.1).

respective flux levels are $2 \cdot 10^{-14} \text{ erg s}^{-1}$ and $10^{-13} \text{ erg s}^{-1}$. To obtain good spectra one would need higher flux levels that are at least an order of magnitude above these values.

In the TeV energy range, the Crab Nebula spectrum between 100 GeV and 10 TeV is given as the top (navy dashed) line, its slope being $p = 2.39$, with an exponential cut-off above 14.3 TeV which was recently measured with HESS (Aharonian et al. 2006). The lower (black dashed) line represents the scaled-down Crab spectrum at 0.1 fraction of the Crab flux. With VERITAS sensitivity, a 6 min measurement at a flux level lower than that of 1 Crab would produce a detailed spectrum (see figure 1.10). Both HESS and VERITAS need integration times longer than one hour to get a spectrum below 0.1 Crab, and below a milliCrab there has not yet been even a detection. Therefore, to properly study the rapid variability one needs fluxes not too far below a Crab. At the lower end of the detectors' energy range, due to various backgrounds (cosmic-ray electrons, night sky background, etc.), the still detectable signal scales with the square root of time. At the higher end, where the source of uncertainty is the lack of events, the sensitivity scales linearly with time because one always imposes a minimum number of events per energy bin. During the course of the simulation of 1 h, the blob moves a few mpc, to a distance at which the contribution of the disc becomes unimportant.

In all of the following plots the dotted black line represents the emitted spectrum at simulation time $t = 0$ s. This is only given as a reference point, since it bears no practical relevance to the observations. The spectra in all of the simulations have the EBL accounted for, using the the model of Kneiske et al. (2004). Note that the host galaxy contributes to the observed SED visibly at the IR – UV band (although in HBLs this contribution is less pronounced) and so the spectra presented here are only representative of the jet emitting region's contribution to the observed SED.

In the first simulation, only the disc EC and the SSC radiation are considered as the cooling mechanisms. Figure 5.1 shows the photon and electron spectra from the emitting blob with the **starting height of 0.5 mpc** along the jet. The black dotted line at $t = 0$ s clearly reflects the shape of the synchrotron peak and the disc which at this scale dominates the IC emission. The proximity of the disc is also reflected in the electron spectrum that has strongly cooled in about a crossing time of the blob, as evident from the TeV flux has has fallen down

5.2. SIMULATIONS

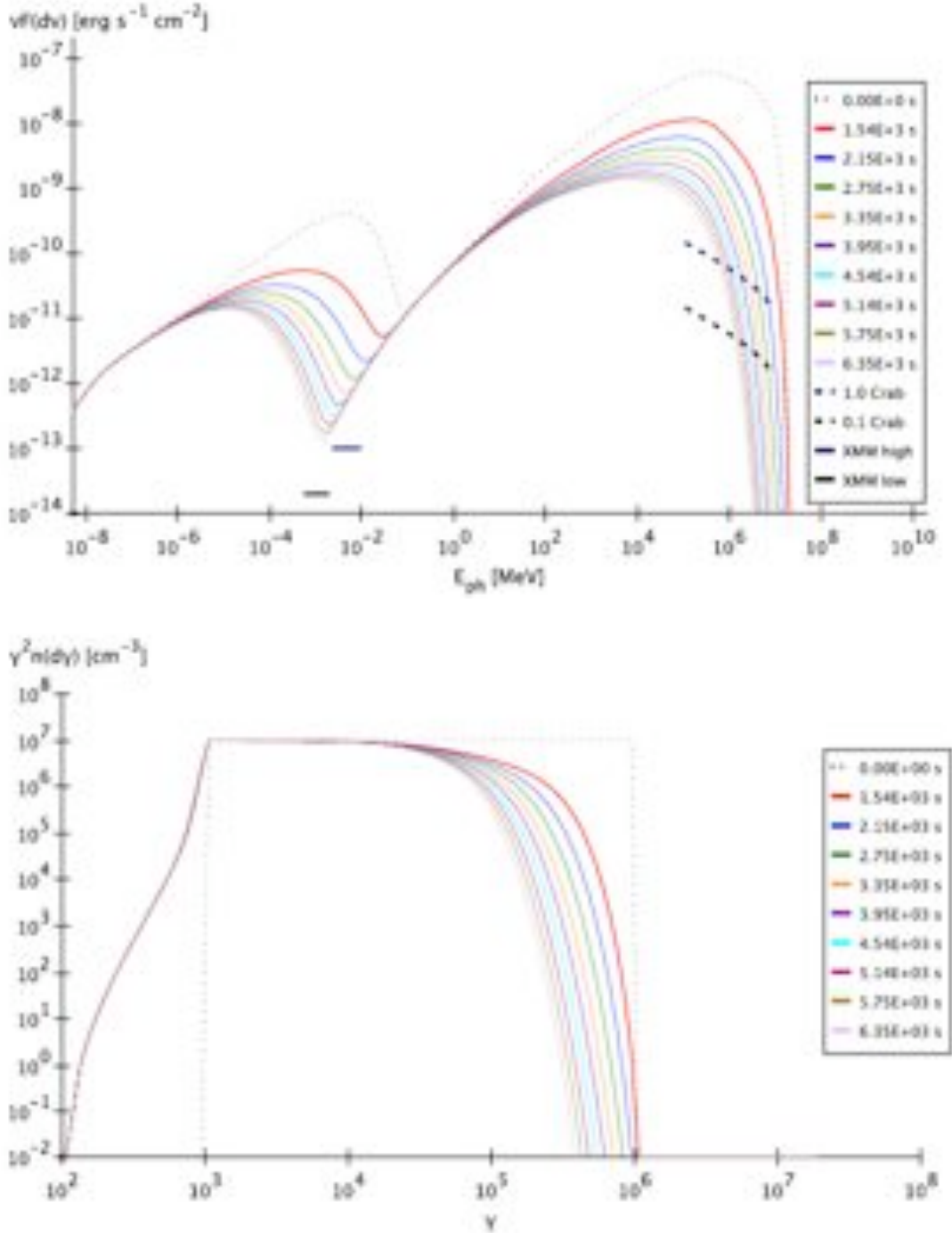


Figure 5.3: Evolving observed photon and electron spectra with a lowered magnetic field ($B = 20$ mG) with respect to figure 5.2 (see table 5.1).

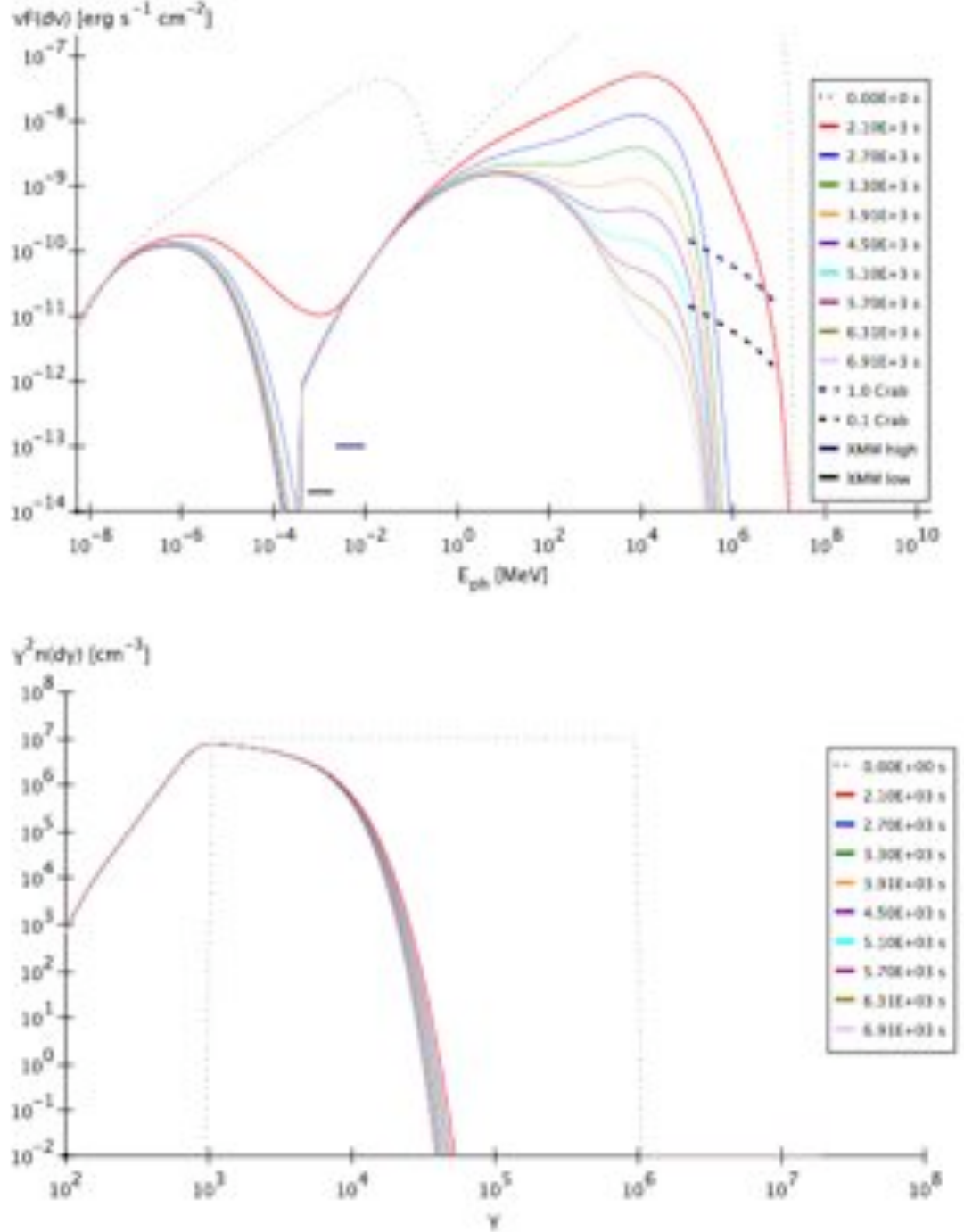


Figure 5.4: Evolving observed photon and electron spectra with a bigger blob radius ($R_b = 8 \cdot 10^{14} \text{cm}$) with respect to figure 5.2 (see table 5.1). Note that an artefact of the numerical lower boundary for the IC spectrum is visible here in the photon spectrum.

5.2. SIMULATIONS

quickly below the observable level owing to the lack of high energy electrons. By the end of the first averaging interval (which is about $2/3$ of the crossing time of the blob), the blob had moved nearly 10 mpc and the IC flux due to the disc targets is now insignificant, and the SSC component is peaking around 1 MeV. The synchrotron component had also dropped several orders of magnitude in the peak position and height since the instantaneous spectrum at $t = 0$. Thereafter, the synchrotron spectrum remains relatively steady. Both humps peak at lower energies – a strong cooling effect seen in GeV blazars – during the simulation.

The disc component stops being important very close to the central engine, at the distances of about 2 – 3 mpc, as can be seen in figure 5.2, plotted for **a farther starting point of 2 mpc**, where the spectra are only very weakly affected by the disc and are very similar to a pure SSC model. The fluxes are then comparable for the two components, as expected (there is still some disc contribution to IC in the first timestep).

Lowering the magnetic field shifts the initial synchrotron and SSC peak positions towards the lower energies by a factor of B (shifting of the IC peak position is not easily observed in the log-log representation). Initial heights of both spectral peaks are lower due a lower magnetic field (scale as B^2). However, lower B also means slower cooling and fall-off times and therefore in this case the duration of both TeV and X-ray flares is longer.

For a **bigger blob**, the initial heights of the synchrotron and SSC peaks scale up by a factor of R_b^3 and R_b^4 , respectively, as there are more particles populating the emitting region (figure 5.4). Note that the IC bump at few tens of GeV is only partially due to disc radiation (which is very weak by this point). Mostly this is due to the Klein-Nishina effect. At later times an absence of energetic electrons is reflected in the single IC bump at about 10 MeV. A slight bump at TeV energies (visible here just during the first averaging interval) is due to the time-averaging over an interval during which the peak position has shifted somewhat towards the lower energies. Note that a bigger blob means a longer crossing time of the blob, and so the first averaging interval starts later than previously. An interesting thing about this scenario is that the X-ray flux is not a signature of a synchrotron peak, but rather due to a low-energy tail of the IC spectrum.

For an order of magnitude **lower particle number density** n_e (figure 5.5), initial synchrotron peak height is lower by an order of magnitude and IC peak is

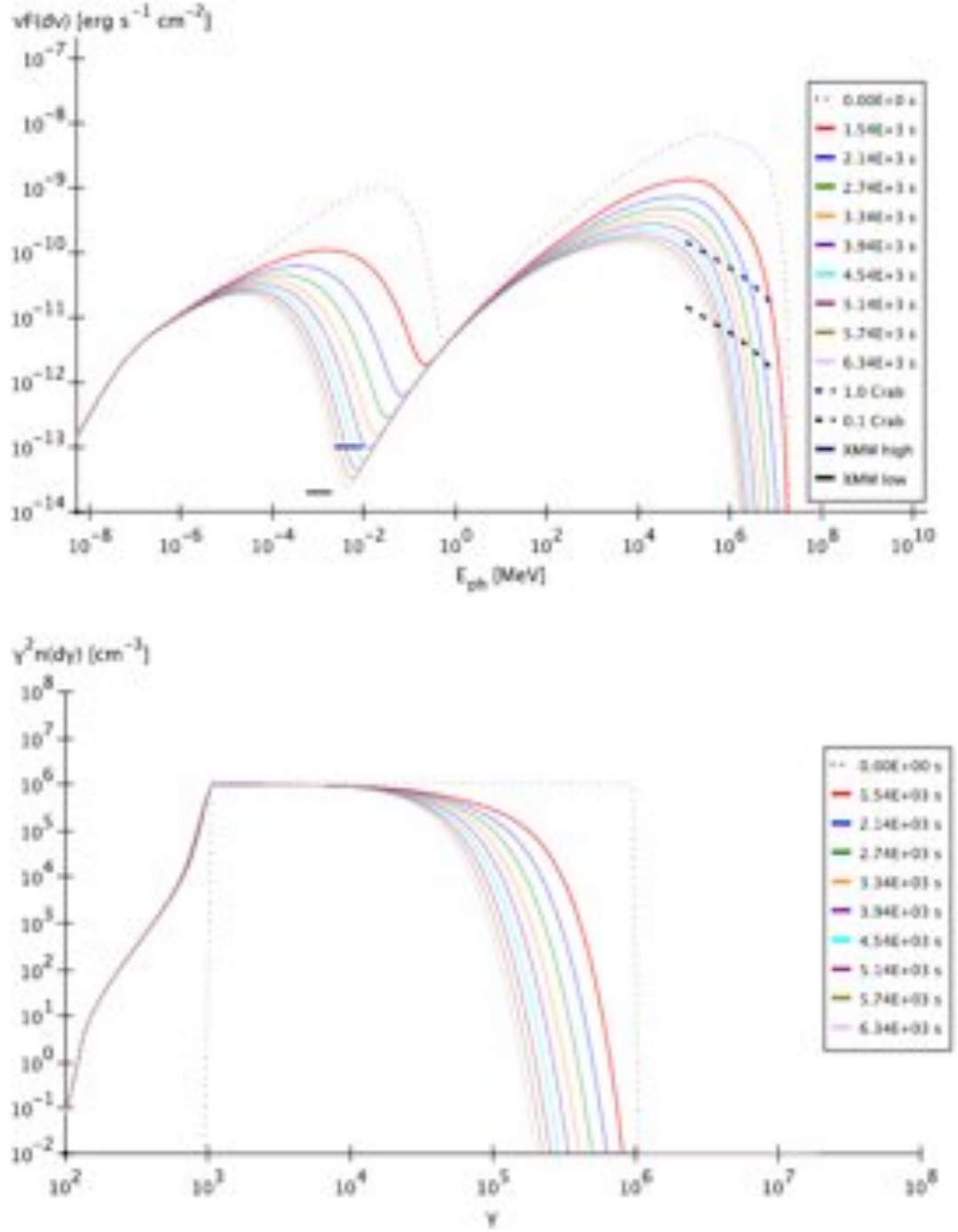


Figure 5.5: Evolving observed photon and electron spectra with a lower electron number density ($n_e = 10^3 \text{ cm}^{-3}$) with respect to figure 5.2 (see table 5.1).

5.2. SIMULATIONS

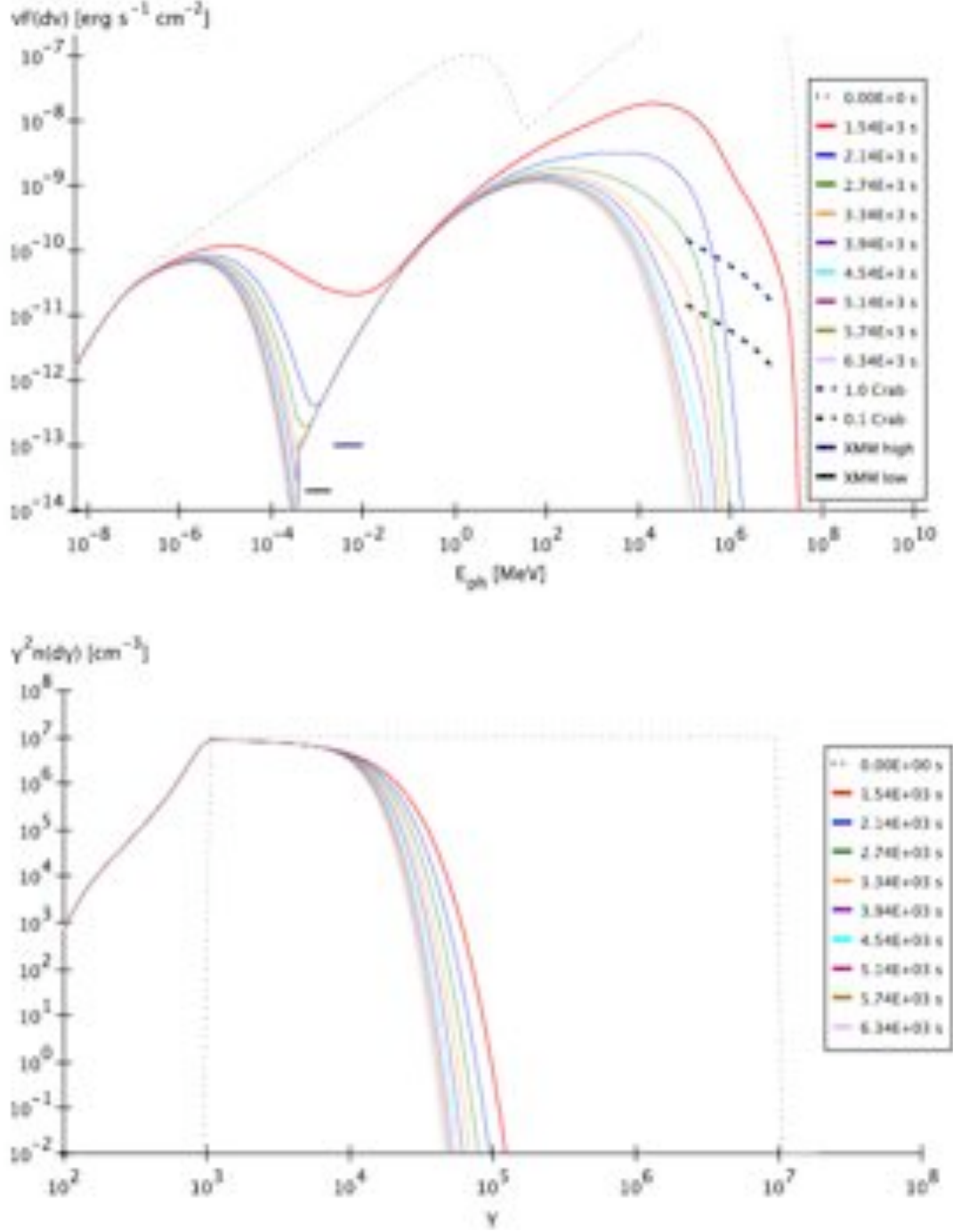


Figure 5.6: Evolving observed photon and electron spectra with a higher maximum cut-off of the electron spectrum ($\gamma_{\text{max}} = 10^7$) with respect to figure 5.2 (see table 5.1).

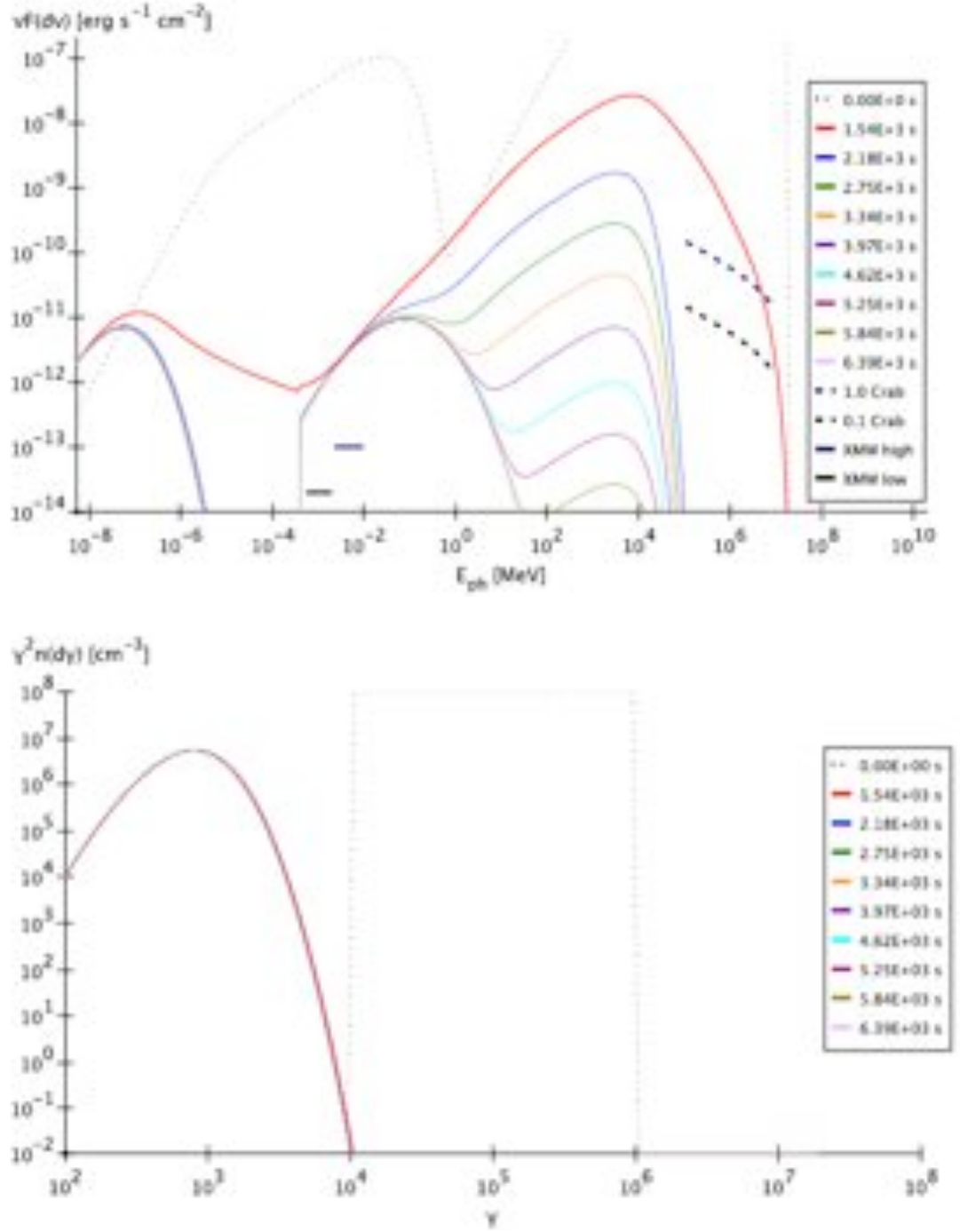


Figure 5.7: Evolving observed photon and electron spectra with a higher minimum cut-off of the electron spectrum ($\gamma_{min} = 10^4$) with respect to figure 5.2 (see table 5.1). Note that an artefact of the numerical lower boundary for the IC spectrum is visible here in the photon spectrum, in keV.

5.2. SIMULATIONS

lower by two orders of magnitude (since they scale as n_e and n_e^2 , respectively), as expected for a predominantly SSC scattering. However, this also means that there are less particles available in the volume and so the cooling is more moderate and less rapid than before, causing the peak position to evolve much more slowly.

An order of magnitude **higher** γ_{\max} means there are more of the energetic particles (figure 5.6). Initial spectrum is very similar to the original one but with more synchrotron photons and upscattered photons at higher energies in each respective band. Both peaks are higher now (synchrotron by an order of magnitude, IC slightly) and shifted in position towards higher energies (synchrotron by 2 orders of magnitude, SSC barely). Except for the first averaging interval, where synchrotron and IC spectra show harder slopes than in the original plots, subsequent evolution is nearly identical to that one for the original γ_{\max} .

An order of magnitude **higher** γ_{\min} causes much higher initial peaks (figure 5.7). Increasing the minimum cut-off will have the effect of a higher number density of electrons per energy interval¹, which in turn increases the height of the synchrotron peak (which scales linearly with number density) and the SSC peak (which scales quadratically with number density). Having a high synchrotron peak will cause very fast particle energy losses. The IC peak subsides from an initial very high value to about the same height as in the original plots by the first averaging interval but the synchrotron spectra have by then shifted downwards in both peak position and height with respect to the original plot. The spectral shape is much different in this scenario due to the extremely quick disappearance of high energy electrons.

The next scenario adds **the BLR**. The BLR provides the targets for IC scattering, but it also moderates the TeV spectrum through pair production (as evident from figure 2.4). As the blob passes through the BLR, it suffers less and less absorption but at the same time electrons are continuing to cool down (in the absence of an accelerator). The parameters for the BLR are given in table 5.2. With the starting point close to the centre, the IC component in the first observing interval shows a strong absorption feature in 1 – 11 TeV range due to the BLR photons. From the starting distances of a few mpc (figure 5.8, lower panel) onwards, the IC component suffers less and less absorption by pair

¹Normalisation for the power law electron spectrum is proportional to $\frac{1-p}{\gamma_{\max}^{1-p} - \gamma_{\min}^{1-p}}$, which is in practice proportional to γ_{\min} for $p = 2$, as γ_{\min} is usually much larger than γ_{\max} (equation 4.21).

5.2. SIMULATIONS

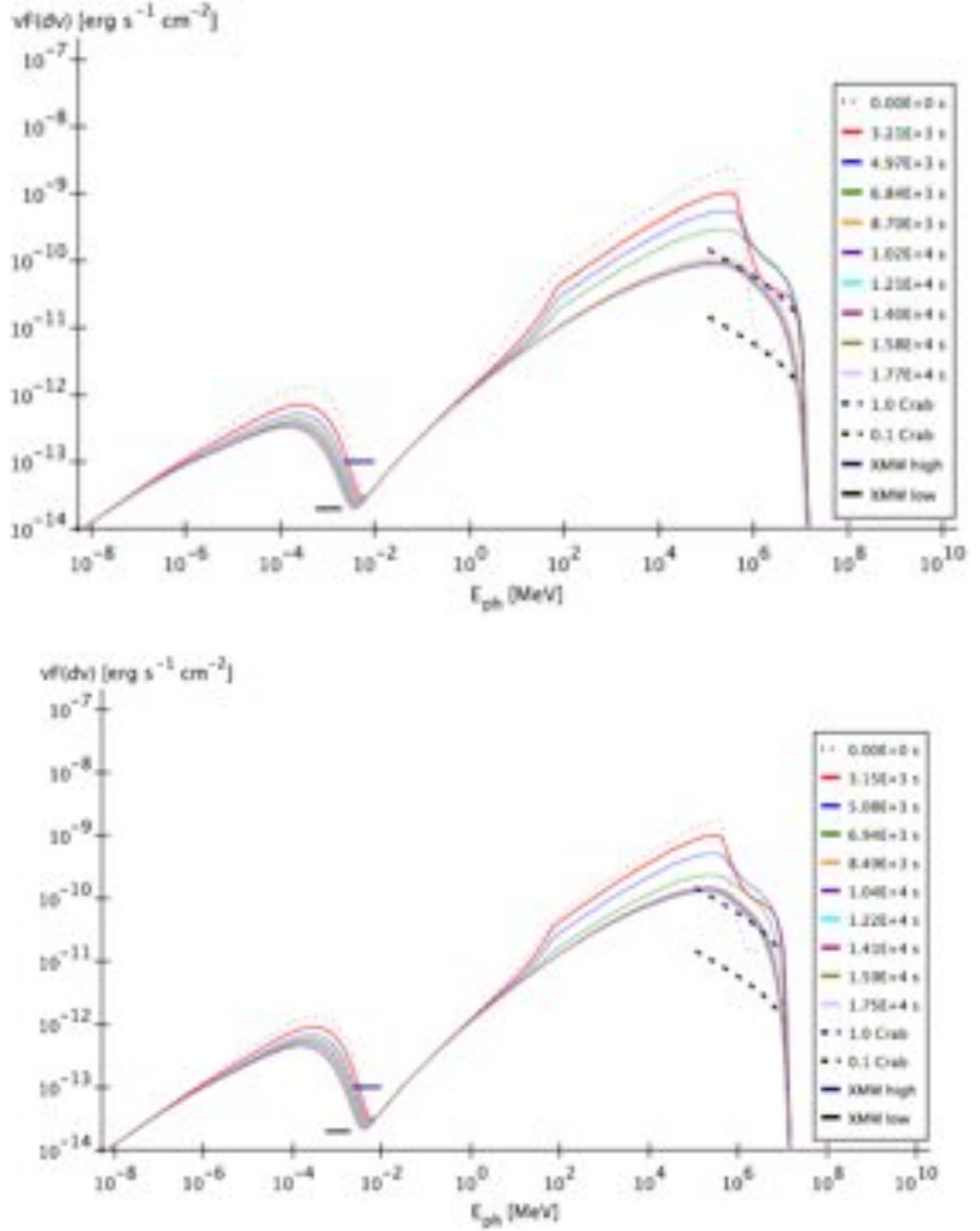


Figure 5.8: Evolving photon spectrum for the simulation starting distances of 2 mpc and 5 mpc, for the parameters $\gamma_{min} = 10^3$, $\gamma_{max} = 5 \cdot 10^7$, $p = 2$, $n_e = 10^4 \text{ cm}^{-3}$, $R_b = 5 \cdot 10^{14} \text{ cm}$, $B = 0.01 \text{ G}$, $t_{obs} = 30 \text{ min}$, $\theta_{obs} = 0.3^\circ$, $z = 0.031$, observing intervals for are 30 min each. Rise and fall of the TeV flux are more visible for a starting point closer to the centre.

5.2. SIMULATIONS

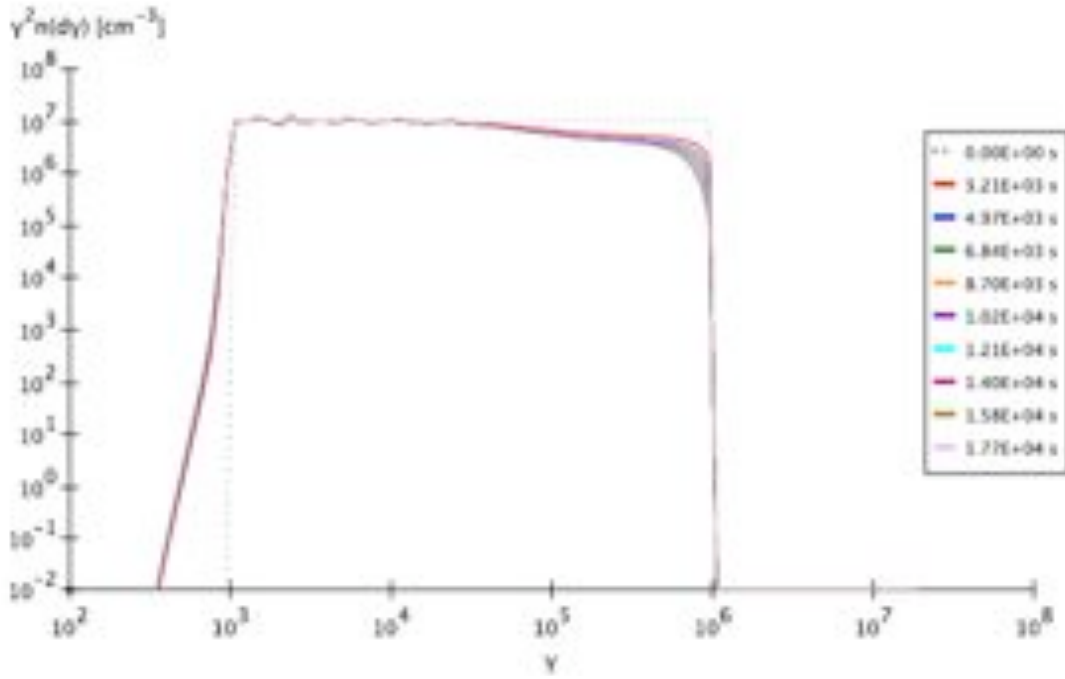


Figure 5.9: Evolving electron spectra for the simulation starting points at 2 mpc, with the inclusion of the BLR (for the photon spectrum, see upper pannel of figure 5.8). Weak cooling is seen due to a very low magnetic field.

Table 5.2: BLR input parameters, given in the galaxy rest frame: λ_{BLR} is the wavelength at which the BLR radiates (H α line), $R_{BLR,in}$ and $R_{BLR,out}$ are the inner and outer radii of the BLR, τ_{BLR} is the optical depth the BLR and α_{BLR} and β_{BLR} are the exponents that govern the power law for the scaling of the number and the radius of the BLR clouds with distance (see Chapter 3.2). BLR optical depth is difficult to put an estimate to and this particular choice is at the lower end, with values higher than 0.1 being often used in literature.

λ_{BLR}	656 nm
$R_{BLR,in}$	10 mpc
$R_{BLR,out}$	40 mpc
τ_{BLR}	0.01
α_{BLR}	-1.5
β_{BLR}	0.6

production, and the hardening of the spectrum is visible at TeV energies.

TeV flux rise without particle acceleration. The rise of the flux is simply due to the decrease in the BLR attenuation of TeV photons, naturally causing the rise and the cessation of the flare. The rising fluxes are usually assumed to mark the particle acceleration phase. At some point (after a few hours) the TeV flux reaches its peak, determined by the balance between the decrease in emission and the decrease in the BLR absorption. After that the peak is reached, the flux can only subside, as the electrons are continuously cooling down, and after a few hours falls below its starting flux. This scenario is represented in figures 5.8 and 5.9 for different starting distances, 5 mpc and 10 mpc. If the starting point is shifted much further this behaviour does not occur for this particular set of parameters. Further than 40 mpc (outer BLR radius), BLR radiation gets redshifted and does not have a great impact on the TeV spectrum. The cooling of the particle spectrum is weak, due to the weak magnetic field, and it changes little during the flare, displaying only a very slight change in the slope (figure 5.9). The TeV range shows rise of the flux along with the hardening of the spectra with time, which was observed in the past (see Krennrich et al. 2002). The simulated observed

5.2. SIMULATIONS

photon spectra and the predicted lightcurves (figure 5.10) follow a similar trend to that observed during the orphan flare in 1ES 1959 (Krawczynski et al. 2004; see figure 1.9), when a TeV flare was observed to rise as the X-ray flux was steadily dying out, although one of the X-ray curves (1 – 10 keV) here displays a lag due to an averaging effect over the spectral dip between the synchrotron and the IC peaks which in this scenario happens to be at quite low energies. There are also energy-dependent lags at higher energies in the TeV band, due to the absorption feature.

Acceleration. The following scenario, presented in figure 5.11, introduces a linear acceleration term, with the acceleration timescale $t_{acc} = 2 \cdot 10^5$ s (see Chapter 4.1). For much higher values of t_{acc} , cooling is too fast for the acceleration to establish a balance between energy gains and losses, even at farther distances from the disc. In this scenario, high-energy electrons are steadily cooling down, although low-energy electrons are getting accelerated, resulting in a peculiar shape of the electron spectrum. The acceleration scenario cannot reproduce the rise and fall of the TeV and synchrotron flux, due to the short acceleration timescale, but the effect of absorption is also still present in the TeV spectrum and contributes to the flattening of the spectrum. However, this acceleration treatment is overly simplistic. In reality the Fermi shock acceleration mechanism generates the power law electron spectra by allowing for the particle escape from the acceleration region during each shock crossing. Also, in the shock acceleration region magnetic field strength is amplified and the value used here is inconsistent with that requirement, so this particular scenario would be difficult to physically justify, but it provides a useful illustration of the effect of the acceleration. The correct treatment of simultaneous acceleration and radiation is one of the most difficult problems in this field and beyond the scope of this thesis.

Comparable heights of the synchrotron and the IC (figure 5.12) peaks are usually observed during the flares in HBLs. This can be achieved by increasing the magnetic field, to get more synchrotron photons, while decreasing the number density of electrons in the volume, to keep the SSC component the same. This results in the IC and synchrotron peak heights being within about an order of magnitude from each other and around $10^{-10} - 10^{-9} \text{ erg s}^{-1} \text{ cm}^{-2}$, which was observed in several flares (e.g. Albert et al. 2007; Aharonian et al. 2007).

5.2. SIMULATIONS

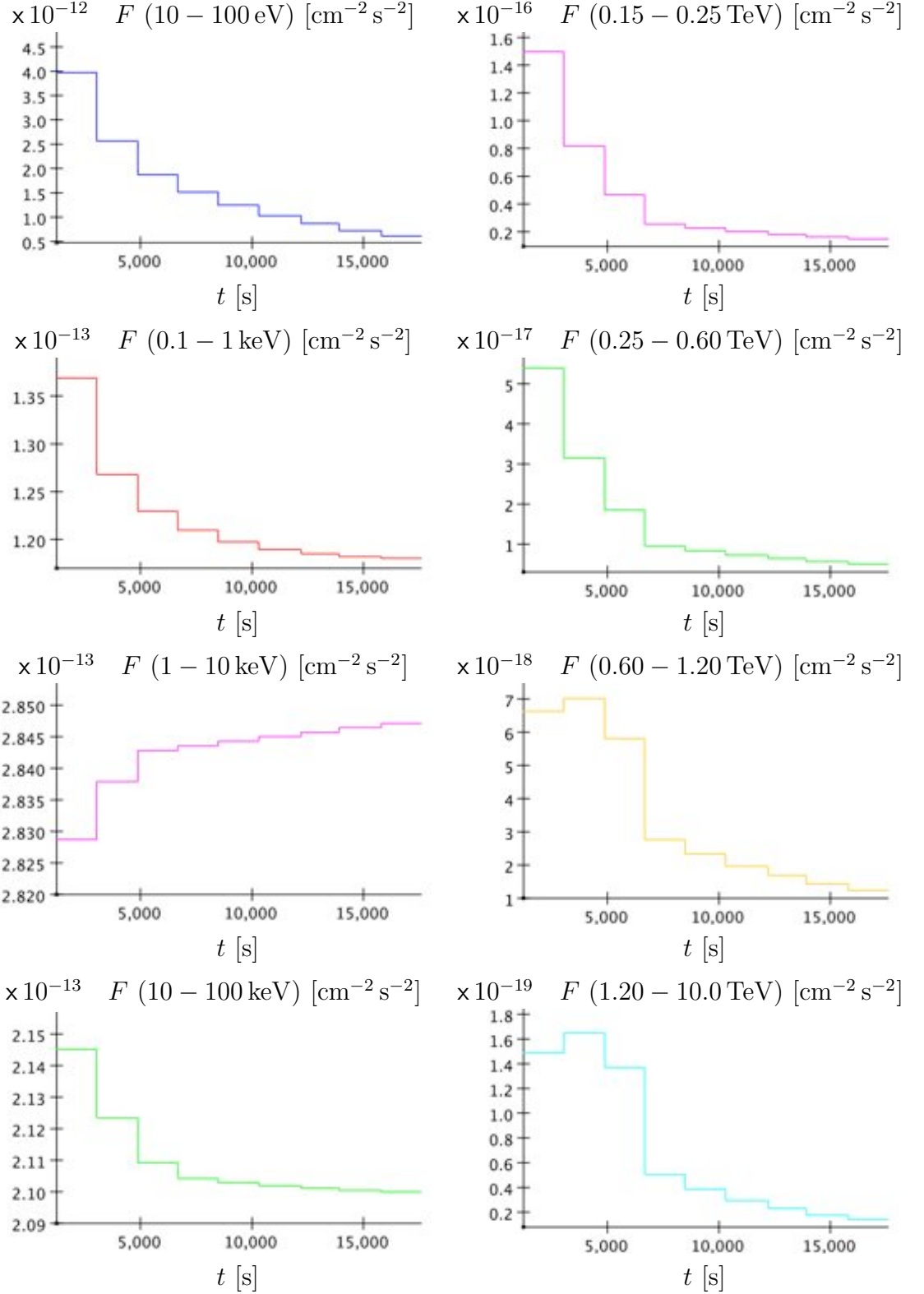


Figure 5.10: Lightcurves at four intervals in the X-ray and TeV parts of the spectrum. The histogram widths represent the time over which the TeV flux is observed. The TeV lags at higher energies reflect the shape of the absorption feature which gets shallower in time. The X-ray peak at 1 – 10 keV is also lagging other energy bands due to the averaging effect over the dip between the two spectral peaks.

5.2. SIMULATIONS

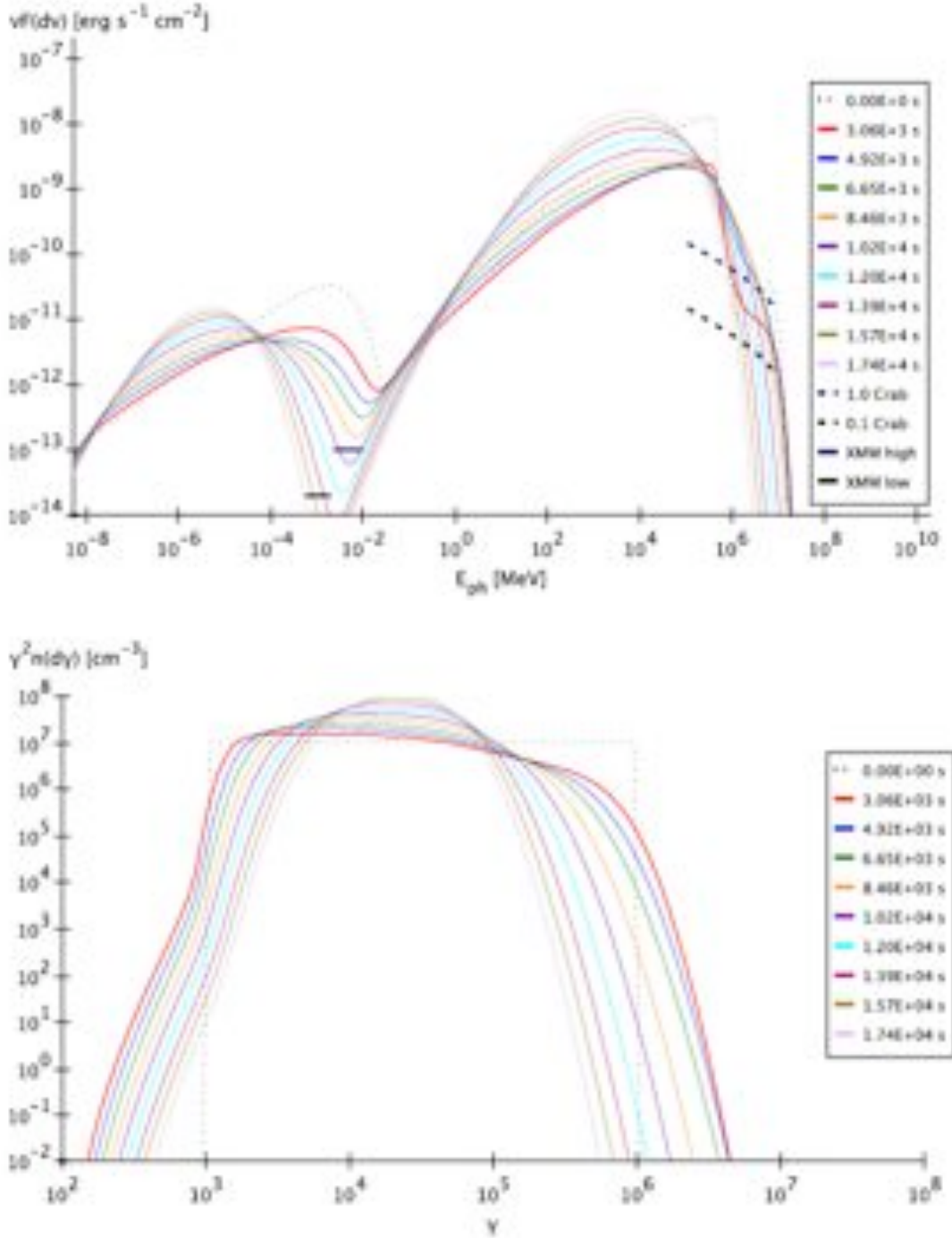


Figure 5.11: Evolving photon and electron spectra for the simulation starting distance of 2 mpc, for the parameters $\gamma_{min} = 10^3$, $\gamma_{max} = 10^6$, $p = 2$, $n_e = 10^4 \text{ cm}^{-3}$, $R_b = 5 \cdot 10^{14} \text{ cm}$, $B = 0.01 \text{ G}$, $t_{obs} = 30 \text{ min}$, $\theta_{obs} = 2^\circ$, $z = 0.031$, observing intervals for are 30 min each. The spectrum is produced by an accelerating population of electrons with a characteristic timescale $t_{acc} = 2 \cdot 10^5 \text{ s}$.

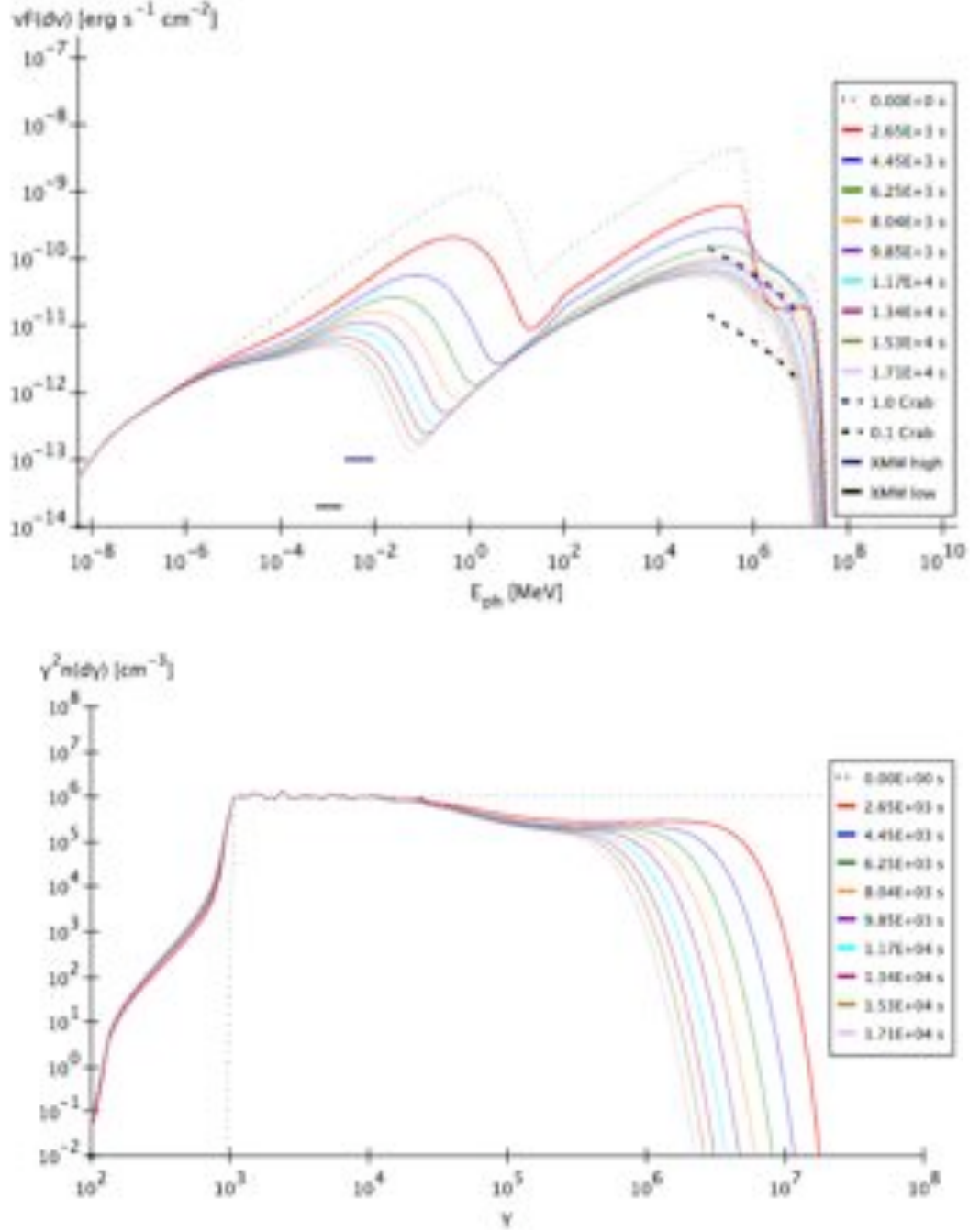


Figure 5.12: Evolving photon and electron spectra for the simulation starting distances of 2 mpc, for the parameters $\gamma_{\min} = 10^3$, $\gamma_{\max} = 3 \cdot 10^7$, $p = 2$, $n_e = 10^3 \text{ cm}^{-3}$, $R_b = 5 \cdot 10^{14} \text{ cm}$, $B = 0.02 \text{ G}$, $t_{\text{obs}} = 30 \text{ min}$, $\theta_{\text{obs}} = 0.3^\circ$, $z = 0.031$. Rise and fall of the TeV flux are visible.

5.3 Discussion of Scenarios and Limitations

The model presented here uses a simplified, spherical geometry of the emitting region. In reality, a conical emission region might be more appropriate (as in Katarzynski et al. 2003). The assumption of homogeneity and isotropic distribution of the electron population in the emitting region also has its limitations, as it means that the synchrotron propagation times within the blob are not taken into account. This makes it impossible to test for the synchrotron – SSC time-lags. The adiabatic expansion of the region has also not been treated here, under the assumption that the sub-parsec jet is well collimated. The model also operates under the assumption of a single scattering, which is usually a very good approximation, but may fail in the case of the very low-energy IC generated photons, which could potentially make a significant contribution as the scattering targets. Also, pairs produced through photon-photon annihilation are not fed back into the system.

Clearly, in the simulations presented in this thesis a limited parameter space is investigated, and many more scenarios can be envisioned and predictions tested with a model such as this. The following is a list of parameters that ought to be investigated further and their potential imprints on the observed SEDs.

1. Increasing the Doppler factor by decreasing the observing angle will simply increase the observed fluxes in both synchrotron and IC and shift the peaks to higher energies by a constant amount. On the other hand, increasing the Doppler factor by increasing the jet gamma factor means additionally affecting the IC peak by boosting the external target photons. Even so, this would only help the disc be significant at the blob distances very close to the centre, but it would have a large impact on the interactions with the BLR targets. A larger ratio between the IC and synchrotron luminosity is favourable when modelling the TeV “orphan” flares.
2. It should be noted that the fraction of disc luminosity reprocessed by the BLR is taken to be relatively low here, 0.01, while it is often quoted as being as high as 0.1. In this thesis only one BLR and disc configuration is investigated, so it would be of interest to study how the predictions may change with different geometries of AGN photon fields. A narrower BLR would give a shorter-lived absorption feature in TeV and so it may help

5.3. DISCUSSION OF SCENARIOS AND LIMITATIONS

model very rapid variability observed in HBLs. An alternative scenario for the very rapid flares caused by the BLR would be due to the vicinity of an individual cloud that could be considered a point or an extended source.

3. The synchrotron and IC fluxes scale in a complicated manner when external fields are introduced, depending on the blob's starting position along the jet. For instance, at small distances from the centre, the incoming disc radiation is boosted strongly, but the effect quickly diminishes as the blob progresses outwards. The situation is even more complicated when the BLR is introduced. The observed time behaviour might therefore point to a place of the origin, which varies (in the scope of the internal shocks scenario) from one flare to another, given the same source.
4. The ratio of the SSC to synchrotron flux is sensitive to the number density of electrons as well as to the radius of the emitting region, and scales linearly with each quantity. To model the behaviour of most flares observed in HBLs, this ratio should be kept as low as possible (as there is also a contribution from the EC component), since the synchrotron and the IC peaks are typically of similar heights in these objects.
5. Different initial high- and low-energy cut-offs also leave imprints on the slopes of the observed SED, as does the slope of the particle spectrum.
6. Particle injection instantaneous here, but by extending it over a period of time one could model the synchrotron rise times.

It is sometimes argued from the data that TeV and X-ray peaks in $\nu F(d\nu)$ representation should be comparable in BL Lac flares (Fossati et al. 1998). In previous scenarios, on shorter timescales, this is only seen when the blob starts far from high external fields, and the observed spectrum this consists only of synchrotron and SSC contributions. Care should be taken in interpreting the data collected so far, since the conclusions derived in the past have mostly relied on the data collected over very long periods of time, often days – months, due to the lack of resolution in older instruments.

As evident from the simulations presented in this chapter, the real picture may be much more complicated than a simple one-zone, homogeneous SSC emission process. External radiation fields cannot be neglected at the distances where

5.3. DISCUSSION OF SCENARIOS AND LIMITATIONS

the observed variable emission is believed to be taking place, which, due to the variability constraints, are believed to be at the scale less than 100 mpc.

Chapter 6

Summary and Conclusions

A model is presented that explores the External Compton target fields' role, along with the flaring features that are seen in the TeV observations of high-peaked BL Lacs, as an alternative to the pure SSC models usually considered.

Ambient photon fields are commonly discredited as unimportant contribution to the seeds for Inverse Compton scattering in TeV blazars, on the basis of very simplified arguments. The simulations in this thesis demonstrate that the real picture can be much more complex, and the behaviour of the observed spectra during the flares to be very sensitive to the position at which the radiation occurs, even for low-luminosity BLRs, such as the one found in Mrk 421.

A detailed, numerical code has been developed to study self-consistently the temporal evolution of the particle distributions in pair plasmas that populate a relativistically moving emission region, with the randomly oriented magnetic field of uniform strength. This region is modelled as a sphere homogeneously filled with isotropic electrons and positrons, but to assume that what we observe is a uniform emission from the whole of the blob is incorrect, since the cooling of the particles should occur on timescales much smaller than the light crossing time of the emission region (Chiaberge & Ghisellini 1999). This means that, unless the particle spectrum is time constant, at any instance in time the observer sees a convolution of spectra produced at different times, owing to the fact that the spectra from the back of the blob take longer to reach us, w.r.t. to the spectra from the top layers. This effect is fully modelled here, by dividing a spherical emission region into slices that are narrow enough to be well approximated as uniform emitters.

The steepening effect of the Inverse Compton cross-section at higher energies is

accounted for by using the full Klein-Nishina cross-section integrated analytically over the isotropic electrons (derived by Reimer et al. 2006). Approximations, such as the outgoing photon moving in the same direction as electron or the monoenergetic treatment of the accretion disc, have been avoided. Importantly, particle energy losses are uniquely treated in an exact manner – particles lost from each energy bin are redistributed over different (in practice only lower) particle energy bins, rather than all being shifted in energy by the amount of the average energy loss.

All of the processes relevant for the ultra-relativistic plasmas have been taken into account. These include synchrotron emission of electrons in the magnetic field with the accompanying synchrotron self-absorption, Inverse Compton Scattering for various seed photons (accretion disc, BLR, synchrotron photons), pair absorption by the local AGN photon fields, namely the accretion disc and the BLR. Intergalactic absorption of gamma-rays has been claimed to be non-negligible even for the low-redshift objects such as Mrk 421 and Mrk 501 from 1 TeV (Primack et al. 1999). This model includes the function describing EBL attenuation with a model and the tabular values calculated by Kneiske et al. (2004). Acceleration is treated here as a continuous function, characterised with an acceleration timescale.

The numerical model presented here allows for the observed spectra to be calculated quickly, with some limitations: so long as the AGN ambient parameters are kept constant, it is very fast to experiment with the blob's and observer's parameters, once the rate coefficients per electron are calculated as matrices for different points along the jet. Since the ambient fields change relatively slowly as the blob progresses outwards, these matrices need only be calculated for a limited number of distances. The code developed is shown to be in good agreement with previous work on the subject for the stationary spectra (except for the disc component in comparison to Böttcher et al. 1997 model). The time evolution is different to that in previous models due to a more different and realistic treatment of radiative losses and time travel effects within the blob. The code was also cross-checked for the correctness of integration algorithms by using two independent integration packages. Being able to perform fast calculations is essential since eventually one wants to be able to perform fits to the actual observed spectra. The code also predicts X-ray and TeV lightcurves for different energy intervals.

The effects of the emission region's passage through the BLR were studied,

for different starting point distances. The pure SSC models are not only not sensitive to the flare's place of origin, but they also suffer the degeneracy between the observing angle and the gamma factor of the emitting region (as the only dependence is on the Doppler factor), as opposed to the EC models, where gamma factor affects the IC peak.

The BLR induced flare scenario, with and without the continuous acceleration, showed a trend similar to the one seen in the orphan flare of 1ES 1959 (Krawczynski et al. 2004), where the synchrotron flux fades while the TeV flux starts to rise quickly. Another interesting thing about this scenario is the hardening of the initially absorbed TeV spectrum, due to the decreasing opacity of the BLR. As the blob starts to emerge, TeV flux goes up and the slope becomes flatter. A similar scenario was able to reproduce the comparable heights of the synchrotron and the IC peaks that are typically seen from HBLs during the outbursts (see e.g. Albert et al. 2007; Aharonian et al. 2007).

The goal of the study was to reproduce the general spectral behaviour and features in the observed SED of TeV emitting BL Lacs. It should be noted though that the previously commonly quoted correlation between the X-ray and TeV peak (in the sense that they should rise simultaneously) should be taken with a pinch of salt – these correlations were mostly derived from the data averaging over very long timescales, due to the limited sensitivity of the TeV detectors. So far there were very few clear examples of flares like those from Mrk 421 from 1996 (Gaidos et al. 1996), 1ES 1959 from 2002 (Krawczynski et al. 2004), Mrk 501 from 2005 (Albert et al. 2007) and PKS 2155 from 2006 (Aharonian et al. 2007), which were exceptionally fortunate events in which the fluxes rose to very high levels. For most of the available variability data, one needs many hours, nights, or weeks often just to get a detection. That means averaging over the spectra produced by the blob from the starting point where its emission becomes visible, say, somewhere in the BLR, to its passage to as far as the NLR, i.e. past the parsec scale. Clearly, the flaring that we see over such long periods (in our frame this corresponds to the timescales of maybe several weeks) cannot be due to one compact, relativistically moving emission region. Equally, even on observing timescales of days, the blob would have to live for at least a few weeks, during which the blob could transverse the whole of the BLR.

The radiative transfer inside the emitting blob has not been modelled and so the models here do not predict the time lags between the synchrotron and IC

peaks due to the the synchrotron radiation propagation times within the blob, although time variability of the synchrotron photons is modelled. However, the models do predict energy-dependent lags at TeV due to the BLR absorbing effect, whereby at the edges of the absorption feature (the lowest and the highest band in the TeV range) flux reach its peak first, having the most absorbed part of the spectrum reach the peak last. Another predicted observable feature is that the TeV first rises in flux and flattens its slope only to fall back down again and steepen after the peak has been reached (after the absorption had decreased). Hence these models can predict the rise and fall-off times of the IC spectrum while they only predict the fall-off of the synchrotron spectrum, since it is assumed that prior to the start of the simulation accelerated electrons have been injected into the emitting region. Therefore the rise time for the synchrotron peak coincides with the acceleration phase (here assumed to precede the emission phase) which is taken to be instantaneous in this model, i.e. freshly accelerated electrons are injected impulsively into the emitting region. This would allow for the low values of the magnetic field that are commonly inferred from the observed spectral data and that are used in the simulation, since in the acceleration phase one expects equipartition, and hence much higher magnetic fields. Magnetic field strength drops quickly as the shock dissipates. The shock acceleration itself is not modelled here.

The scenarios used in this thesis do not seem to be able to reproduce the very rapid variability of the order of minutes, but a somewhat longer variability on the timescales of a couple of hours. It might be possible to reproduce the more rapid variability if a much narrower BLR shell was used. Another way to obtain very rapid variability patterns from the EC scenarios would be to consider a passage of the blob near an emitting BLR cloud (i.e. to consider a local peak in BLR emission) that could be modelled as either a point source or an extended spherical region. Such a scenario could also extend the model in this thesis to the case of microquasars, where the external photon targets are provided by a companion star.

The code also allows for a pure synchrotron – SSC flare, which is expected when the acceleration occurs outside the BLR. Therefore the model presented allows for the both scenarios (pure SSC as well as the SSC+EC), and hence allows for the same object to display various flare profiles, depending on where the shocks catch up with one another along the jet. The EC+SSC model also

allows for the unusual observations, namely the orphan flares, to be naturally accounted for, by considering that flares originate at different distances along the jet.

To test the predictions, clearly the time-resolved multiwavelength spectra are necessary to get a realistic picture of the observed spectral shape. Spectra averaged over many hours/days/weeks are likely to measure a superposition of many individual flares, for which fitting spectra is less meaningful. In the simulations presented here averaging of observed spectra is done over shorter time intervals (10 min, 30 min), in anticipation of the better resolved spectra from the current generation of Cherenkov detectors (HESS, MAGIC, VERITAS).

Appendix A

Coefficients

This section gives the coefficients that were used for numerical rate calculations that were outlined in Chapter 4.

The coefficient that defines the fraction of electrons at energy i that have moved down to energy j per given timestep is

$$\lambda_{ij} = \Delta\gamma_j \int_{\Omega_s} \int_{\epsilon} \int_{\Omega} n_{ph}(d\epsilon, d\Omega_{ph}) \frac{dC(\epsilon, \gamma)}{d\epsilon_s d\Omega_s} d\epsilon d\Omega d\Omega_s \quad (\text{A.1})$$

and has units of $[\text{s}^{-1}]$. Here one is already representing the particle spectrum as a collection of energy bins. In the equation above it is assumed that the energy bin width $\Delta\gamma_j$ is small enough so that the IC cross section does not vary across it. This is not always true, and very small losses (less than the energy bin width) could cause an overestimate in the loss term at a particular energy. One way to correct for it would be to perform a full integral over both the i and j bin. One can still assume that the spectrum is fairly constant over the range of one bin, and so can be left as a histogram. Only the coefficients λ_{ij} are calculated in more detail. Since two more dimensions of integration (over the ‘initial’ and ‘final’ energy bin) are added, the expression has to be divided by their respective binwidths $\Delta\gamma_i$ and $\Delta\gamma_j$

$$\lambda_{ij} = \frac{1}{\Delta\gamma_i} \int_{\gamma_{i,bin}} \int_{\gamma_{j,bin}} \int_{\Omega_s} \int_{\epsilon} \int_{\Omega} n_{ph}(d\epsilon, d\Omega_{ph}) \frac{dC(\epsilon, \gamma)}{d\epsilon_s d\Omega_s} d\epsilon d\Omega d\Omega_s d\gamma_{j,bin} d\gamma_{i,bin} \quad (\text{A.2})$$

Similar is done for the photon spectrum, which is also discretised, and represented with energy bins ϵ equidistant in log. The photon coefficients $\zeta_{i,s}$, which are here

defined as

$$\zeta_{i,s} = \Delta\gamma_i \int_{\Omega_{ph}} \int_{\epsilon} n_{ph}(d\epsilon, d\Omega_{ph}) \frac{dC(\epsilon, \mu_{ph}, \gamma)}{d\epsilon_s d\Omega_s} d\epsilon d\Omega_{ph} \quad (\text{A.3})$$

can be wrapped in the integrations over the initial electron's bin i and final photon's bin s , while dividing through with $\Delta\gamma_i$ and $\Delta\epsilon_s$

$$\zeta_{i,s} = \frac{1}{\Delta\epsilon_s} \int_{\epsilon_{s,bin}} \int_{\gamma_{i,bin}} \int_{\Omega_{ph}} \int_{\epsilon} n_{ph}(d\epsilon, d\Omega_{ph}) \frac{dC(\epsilon, \Omega_{ph}, \gamma)}{d\epsilon_s d\Omega_s} d\epsilon d\Omega_{ph} d\gamma_{i,bin} d\epsilon_{s,bin} \quad (\text{A.4})$$

Appendix B

Approximation for small $\frac{\mu_+ - \mu_-}{\mu_+}$

The fact that $\frac{\mu_+ - \mu_-}{\mu_+}$ can be very small can present practical problems in numerical calculations. Here an approximation to the scattering rate is calculated for such a case, which gives values for the rate in very good agreement with the correct treatment.

Photon spectrum calculated from the full Klein-Nishina cross-section (Reimer et al. (2006)) is

$$\begin{aligned} \dot{n}_{ph}(d\epsilon_s, d\Omega_s) = & \frac{3}{16\pi} \sigma_T c \epsilon_s \int_{\epsilon} \int_{\mu_{ph,e}} \int_{\gamma} n_e(\gamma) n_{ph}(d\epsilon, d\mu_{ph,e}) \Theta(\epsilon_s - \epsilon_{s1}) \\ & \times \frac{1}{\beta \gamma^2 \epsilon \sqrt{\epsilon_s^2 - 2\mu_{ph,e} \epsilon \epsilon_s + \epsilon^2}} \\ & \times \left[1 - \frac{1}{(2\epsilon_s \gamma \beta)^2} \left(\frac{\mu_+ + \mu_- + 2b}{((\mu_+ + b)(\mu_- + b))^{\frac{3}{2}}} + \frac{\mu_+ + \mu_- + 2a}{((\mu_+ + a)(\mu_- + a))^{\frac{3}{2}}} \right) \right. \\ & - \left(\frac{\epsilon(1 - \mu_{ph,e})}{2\gamma\beta} - \frac{\epsilon\epsilon_s(1 - \mu_{ph,e}) + 1}{\gamma\beta\epsilon_s^2(1 - \mu_{ph,e})} \right) \\ & \left. \times \left(\frac{1}{((\mu_+ + b)(\mu_- + b))^{\frac{1}{2}}} + \frac{1}{((\mu_+ + a)(\mu_- + a))^{\frac{1}{2}}} \right) \right] d\gamma d\mu_{ph,e} d\epsilon \end{aligned} \quad (B.1)$$

The term in square brackets is a solution of the following integral (see equation C.46 in Reimer et al. 2006)

$$I = \frac{1}{2\pi} \int_{\mu_-}^{\mu_+} \frac{d\mu}{\sqrt{(\mu - \mu_-)(\mu_+ - \mu)}} (2 + F_2 + F_3) \quad (B.2)$$

with

$$F_2 = \frac{D_2}{(\mu + a)(\mu + b)} \quad (\text{B.3})$$

$$F_3 = \frac{D_3}{(\mu + a)^2 (\mu + b)^2} \quad (\text{B.4})$$

where

$$D_2 = \frac{\epsilon}{\epsilon_s} \frac{(1 - \mu_{ph,e})}{(\beta\gamma)^2} (\epsilon\epsilon_s (1 - \mu_{ph,e}) - 2) \quad (\text{B.5})$$

$$D_3 = \left(\frac{\epsilon}{\epsilon_s} \frac{(1 - \mu_{ph,e})}{(\beta\gamma)^2} \right)^2 \quad (\text{B.6})$$

The following integral can be solved analytically

$$\int_{\mu_-}^{\mu_+} \frac{1}{\pi \sqrt{(\mu - \mu_-)(\mu_+ - \mu)}} d\mu = 1 \quad (\text{B.7})$$

The integrand of this equation has a property of a δ -function, if μ_- and μ_+ are close to each other (i.e. $\Delta\mu = \mu_+ - \mu_- \rightarrow 0$). If one defines such a δ -function as

$$\Theta(\mu) = \frac{1}{\pi \sqrt{(\mu - \mu_-)(\mu_+ - \mu)}} \quad (\text{B.8})$$

Then

$$\lim_{\Delta\mu \rightarrow 0} \int_{\mu_-}^{\mu_+} \frac{1}{\pi \sqrt{(\mu - \mu_-)(\mu_+ - \mu)}} d\mu = \int_{-\infty}^{+\infty} \Theta(\mu) d\mu = 1 \quad (\text{B.9})$$

and also the following will hold

$$\lim_{\Delta\mu \rightarrow 0} \int_{\mu_-}^{\mu_+} \frac{1}{\sqrt{(\mu - \mu_-)(\mu_+ - \mu)}} f(\mu) d\mu = \pi \int \Theta(\mu) f(\mu) d\mu = \pi f(\mu) \quad (\text{B.10})$$

Applying this result to equation B.2, I can now be rewritten as

$$I \simeq \frac{1}{2\pi} \pi (2 + I_2 + I_3) \quad (\text{B.11})$$

APPENDIX B

If a variable K is defined as

$$K = \frac{\epsilon}{\epsilon_s} \frac{(1 - \mu_{ph,e})}{(\beta\gamma)^2} \frac{1}{(\mu + a)(\mu + b)} \quad (\text{B.12})$$

and substituted into equation B.2, one arrives at

$$I \simeq \frac{1}{2} (2 + K (\epsilon\epsilon_s (1 - \mu_{ph,e}) - 2 + K)) \quad (\text{B.13})$$

or

$$I \simeq 1 + \frac{K}{2} (\epsilon\epsilon_s (1 - \mu_{ph,e}) - 2 + K) \quad (\text{B.14})$$

Bibliography

- Aharonian, F. et al. 2006, A&A, 457, 899
- Aharonian, F. et al. 2007, 664, L71
- Aharonian, F. A. 2000, New Astronomy, 5, 377
- Aharonian, F. A. 2002, MNRAS, 332, 215
- Albert, J. et al. 2007, ApJ, 669, 862
- Balbus, S. A. 2006, Nature, 444, 281
- Begelman, M. C. & Rees, M. 1996, Gravity's Fatal Attraction (Scientific American Library)
- Blandford, R. D. 1976, MNRAS, 176, 465
- Blandford, R. D. & Begelman, M. C. 1999, MNRAS, 303, L1
- Blandford, R. D. & Königl, A. 1979, ApJ, 232, 34
- Blandford, R. D. & Levinson, A. 1995, ApJ, 441, 79
- Blandford, R. D. & Payne, D. G. 1982, MNRAS, 199, 883
- Blandford, R. D. & Znajek, R. 1977, MNRAS, 179, 433
- Blazejowski, M. et al. 2005, ApJ, 630, 130
- Bloom, S. D. & Marscher, A. P. 1996, ApJ, 461, 657
- Blumenthal, G. R. & Gould, R. J. 1970, Reviews of Modern Physics, 42, 237
- Böttcher, M. 2005, ApJ, 621, 176

BIBLIOGRAPHY

- Böttcher, M. & Chiang, J. 2002, *ApJ*, 581, 127
- Böttcher, M., Mause, H., & Schlickeiser, R. 1997, *A&A*, 324, 395
- Buckley, J. H. 1998, *Science*, 279, 676
- Chiaberge, M. & Ghisellini, G. 1999, *MNRAS*, 306, 551
- Cools, R. & Haegemans, A. 2003, *ACM Trans. Math. Software*, 29, 287
- Coppi, P. S. 1992, *MNRAS*, 258, 657
- Coppi, P. S. 2002, in *The Universe Viewed in Gamma-rays*, University of Tokyo Symposium, ed. R. Enomoto, M. Mori, & S. Yanagita (Universal Academy Press: Tokyo), 77
- Coppi, P. S. & Aharonian, F. A. 1999, *APh*, 11, 35
- Coppi, P. S. & Blandford, R. D. 1990, *MNRAS*, 245, 453
- Corbett, E. A., Robinson, A., Axon, D. J., & Hough, J. H. 2000, *MNRAS*, 311, 485
- Costamante, L. 2001, PhD thesis, University of Milano
- Crusius, A. & Schlickeiser, R. 1988, *A&A*, 196, 327
- Dai, H., Xie, G. Z., Zhou, S. B., et al. 2007, *AJ*, 133, 2187
- Daum, A. et al. 1997, *APP*, 8, 1
- Dermer, C. D. & Schlickeiser, R. 1993, *ApJ*, 416, 458
- Donea, A.-C. & Protheroe, R. J. 2003, *APh*, 18, 377
- Drury, L. 1983, *SSRv*, 36, 57
- Fabian, A. C., Guilbert, P. W., Blandford, R. D., Phinney, E. S., & Cuellar, L. 1986, *MNRAS*, 221, 931
- Falcke, H., Gopal-Krishna, & Biermann, P. L. 1995, *A&A*, 298, 395

- Fossati, G., Buckley, J., Edelson, R. A., Horns, D., & Jordan, M. 2004, in *New Astronomy Reviews*, Vol. 48, 2nd VERITAS Symposium on the Astrophysics of Extragalactic Sources, ed. S. Swordy & L. Fortson, 419–422
- Fossati, G., Maraschi, L., Celotti, A., Comastri, A., & Ghisellini, G. 1998, *MNRAS*, 299, 433
- Frank, J., King, A. R., & Raine, D. J. 1992, *Accretion Power in Astrophysics*, 2nd edn. (Cambridge University Press)
- Gaidos, J. A. et al. 1996, *Nature*, 383, 319
- Genz, A. C. & Malik, A. A. 1980, *J. Comput. Appl. Math.*, 295
- Ghisellini, G. 1999, *APh*, 11, 11
- Ghisellini, G. 2001, in *ASP Conference Series*, ed. P. Padovani & M. Urry, Vol. 227, 85
- Ghisellini, G., Celotti, A., Fossati, G., Maraschi, L., & Comastri, A. 1998, *MNRAS*, 301, 451
- Ghisellini, G. & Madau, P. 1996, *MNRAS*, 280, 67
- Hartman, R. C. et al. 1999, *ApJS*, 123, 79
- Hinton, J. 2004, in 2nd VERITAS Symposium on the Astrophysics of Extragalactic Sources, ed. S. Swordy & L. Fortson, *New Astronomy Reviews*, 331–337
- Hubbard, A. & Blackman, E. G. 2008, *MNRAS*, 390, 331
- Jauch, J. M. & Rohrlich, F. 1980, *The Theory of Photons and Electrons*, 2nd edn. (Springer-Verlag)
- Jones, F. C. 1968, *PhRv*, 167, 1159
- Kaspi, S., Maoz, D., Netzer, H., et al. 2005, *ApJ*, 629, 61
- Kaspi, S. & Netzer, H. 1999, in *ASP Conf. Series*, Vol. 162, 223
- Kataoka, J. et al. 1999, *ApJ*, 512, 138

BIBLIOGRAPHY

- Katarzynski, K., Ghisellini, G., Tavecchio, F., & Gracia, J. 2006, MNRAS Letters, 368, 52
- Katarzynski, K., Sol, H., & Kus, A. 2001, A&A, 367, 809
- Katarzynski, K., Sol, H., & Kus, A. 2003, A&A, 410, 101
- Kemhavi, A. K. & Narlikar, J. V. 1999, Quasars and active galactic nuclei: an introduction (Cambridge University Press)
- Kildea, J. et al. 2007, APh, 28, 182
- Kirk, J. G. & Schneider, P. 1987, ApJ, 315, 425
- Kneiske, T. M., Bretz, T., Mannheim, K., & Hartmann, D. H. 2004, A&A, 413, 807
- Krawczynski, H. 2004, New Astronomy Reviews, 48, 367
- Krawczynski, H., Coppi, P. S., & Aharonian, F. A. 2002, MNRAS, 336, 721
- Krawczynski, H. et al. 2004, ApJ, 601, 151
- Krennrich, F. et al. 2002, ApJ, 575, L9
- Lang, K. R. 1999, Astrophysical Formulae, Vol. II: Space, Time, Matter and Cosmology., 3rd edn. (Springer-Verlag, New York)
- Lorenz, E. & Martinez, M. 2005, Astronomy & Geophysics, 46, 6.21
- Mannheim, K. 1993, A&A, 269, 67
- Mastichiadis, A. & Kirk, J. G. 1997, A&A, 320, 19
- Morganti, R., Ulrich, M.-H., & Tadhunter, C. N. 1992, MNRAS, 254, 546
- Mücke, A., Protheroe, R. J., Engel, R., Rachen, J. P., & Stanev, T. 2003, APh, 18, 593
- Narayan, R. & Insu, Y. 1994, ApJ, 428, L13
- Nieppola, E., Valtaoja, E., Tornikoski, M., Hovatta, T., & Kotiranta, M. 2008, A&A, 488, 867

- Padovani, P. 1998, in Vulcano Workshop "Frontier Objects in Astrophysics and Particle Physics
- Padovani, P. 2007, *Ap&SS*, 309, 63
- Petry, D., Böttcher, M., Connaughton, V., et al. 2000, *ApJ*, 536, 742
- Primack, J. R., Bullock, J. S., Somerville, R. S., & MacMinn, D. 1999, *APh*, 11, 93
- Rees, M. J., Netzer, H., & Ferland, G. J. 1989, *ApJ*, 347, 640
- Reimer, A., Pohl, M., & Reimer, O. 2006, *ApJ*, 644, 1118
- Robson, I. 1996, *Active Galactic Nuclei* (John Wiley & Sons Ltd.)
- Rybicki, G. B. & Lightman, A. P. 1979, *Radiative Processes in Astrophysics*
- Sauty, C., Tsinganos, K., & Trussoni, E. 2002, in *Lecture Notes in Physics*, Vol. 589, *Relativistic flows in Astrophysics*, ed. A. Guthmann, M. Georganopoulos, A. Marcowith, & K. Manolakou (Springer-Verlag), 41
- Shakura, N. I. & Sunyaev, R. A. 1973, *A&A*, 24, 337
- Sikora, M., Begelman, M. C., & Rees, M. 1994, *ApJ*, 421, 153
- Sikora, M. & Madejski, G. 2001, *X-RAY ASTRONOMY: Stellar Endpoints, AGN, and the Diffuse X-ray Background*. AIP Conference Proceedings, 599, 935
- Sikora, M., Madejski, G., & Begelman, M. C. 1997, in *Proceedings of the International Conference: Relativistic Jets in AGNs*, 287–293
- Simon, M. 1969, *ApJ*, 156, 341
- Skelton, P. 1999, PhD thesis, University of Leeds
- Skelton, P. 2001, in *High Energy Gamma-Ray Astronomy*, AIP Conf. Proceedings, Vol. 558, 692
- Tavecchio, F. 2005, in *10th Marcel Grossmann Meeting*, 512

BIBLIOGRAPHY

- Ulrich, M., Maraschi, L., & Urry, C. M. 1997, *Annu. Rev. Astron. Astrophys.*, 35, 445
- Urry, C. M. & Padovani, P. 1995, *Publications of the ASP*, 107, 803
- Verheest, F. 2006, *Physics of Plasmas*, 13
- Wagner, S. J. & Witzel, A. 1995, *Annual Review of Astronomy and Astrophysics*, 33, 163
- Wandel, A. 1997, *ApJ Letters*, 490, L131
- Watson, M. G. et al. 2001, *A&A*, 365, L51
- Weaver, T. A. 1976, *Physical Review A*, 13, 1563
- Weekes, T. C. 2008, in *AIP Conference Proceedings*, Vol. 1085, *HIGH ENERGY GAMMA-RAY ASTRONOMY: Proceedings of the 4th International Meeting on High Energy Gamma-Ray Astronomy*, 3–17
- Weekes, T. C. et al. 1989, *ApJ*, 342, 379
- Weekes, T. C. et al. 2002, *APh*, 17, 221
- Wehrle, A. E. 1997, *Bulletin of the AAS*, 29, 1304
- Zdziarski, A. A. 1988, *ApJ*, 335, 786